UiO : University of Oslo

Stig Asle Vaksvik Synnes

Advanced Processing for Synthetic Aperture Sonar

Thesis submitted for the degree of Philosophiae Doctor

Department of Informatics

The Faculty of Mathematics and Natural Sciences

Norwegian Defence Research Establishment (FFI)

2021

Series of dissertations submitted to the
Faculty of Mathematics and Natural Sciences, University of Oslo
No. 2415

ISSN 1501-7710

Cover: Hanne Baadsgaard Utigard.
Print production: Reprosentralen, University of Oslo.

Preface

This thesis is submitted in partial fulfillment of the requirements for the degree of *Philosophiae Doctor* at the University of Oslo. The research presented here was conducted at the University of Oslo (UiO) and at the Norwegian Defence Research Establishment (FFI) under the supervision of adjunct professor Roy Edgar Hansen and professor Andreas Austeng. Roy Edgar Hansen is a principal scientist at FFI, while Andreas Austeng is a professor at UiO.

I am employed at FFI, where I started in 1998 after receiving my degree of Cand. Scient. in Physics from the University of Bergen. The work on the thesis was conducted as a part of my job over the years 2011 – 2021, and was funded by FFI's projects on synthetic aperture sonar (SAS). These SAS projects have been run and financed through a collaboration between FFI, Kongsberg Maritime and the Royal Norwegian Navy.

This thesis includes a collection of five papers, placed and presented in a larger common perspective. I first place the title topic of *"Advanced SAS"* in a greater context. Then I present each of the individual papers, and give an updated review on their topics. I follow up with a discussion on my contributions in a greater perspective, before I summarize my findings and conclude.

Acknowledgements

I would like to thank my research colleagues of the SAS signal processing group at FFI: Roy Edgar Hansen, Torstein Olsmo Sæbø, Ole Jacob Lorentzen and Marc Geilhufe. It is fun to work in a team where challenging established truths is encouraged, and potentially rewarded with a beer after months of research. You have a non-failing and inspiring enthusiasm for SAS research, embracing any challenge from a multitude of angles, flavored with your individual expertise and preferences. Also many thanks to the rest of the Underwater Robotics group at FFI, both for providing a broader insight into the operations of autonomous underwater vehicles (AUVs), and for their contribution to the social work environment.

Thanks to my supervisors adjunct professor Roy Edgar Hansen and professor Andreas Austeng with the University of Oslo for their support on both research topics and administrative tasks. I have appreciated your company, both at campus and abroad on conferences. I also enjoyed the time together with fellow students and researchers at the Digital Signal Processing group.

In Norway, we have a fruitful long-term collaboration on the development of AUV and SAS. This collaboration has brought together long term research by FFI, applications and operations by the Royal Norwegian Navy, and industrialization by Kongsberg Maritime. I have had a huge benefit from working within this collaboration, and I appreciate the contacts I have made there. I also value the contact with my former FFI-colleagues Hayden John Callow and Per Espen Hagen, who are now at Kongsberg Maritime.

My SAS experience has been widened and flavoured by the annual meetings of the Mine Counter Measures (MCM) related Joint Research Projects (JRP) at the NATO Center for Maritime Research and Experimentation (CMRE). These meetings have brought the national MCM communities together, and have worked as catalysts for interesting off-spring collaborations.

My greatest thanks go to my wife Marit who makes every day bright, and to our three boys, Marius, Joakim and Emil for all the fun they bring along.

Stig Asle Vaksvik Synnes
Oslo, June 2021

List of Included Publications

Paper I*

Sæbø, T. O., Synnes, S. A. V., and Hansen, R. E. (2013). "Wideband interferometry in synthetic aperture sonar". In: *IEEE Transactions on Geoscience and Remote Sensing* vol. 51, no. 8, pp. 4450–4459

Paper II

Synnes, S. A. V., Hunter, A. J., Hansen, R. E., Sæbø, T. O., Callow, H. J., Vossen, R. van, and Austeng, A. (2017). "Wideband synthetic aperture sonar backprojection with maximization of wave number domain support". In: *IEEE Journal of Oceanic Engineering* vol. 42, no. 4, pp. 880–891

Paper III

Synnes, S. A. V. and Hansen, R. E. (2015). "Aspect-dependent scattering in widebeam synthetic aperture sonar". In: *Proceedings of the 3rd Underwater Acoustics Conference and Exhibition (UACE)*. Chania, Crete, Greece, pp. 129–136

Paper IV

Synnes, S. A. V. and Lorentzen, O. J. (2019). "Calibration target for estimation of frequency dependence in synthetic aperture sonar". In: *Proceedings of the 5th Underwater Acoustics Conference and Exhibition (UACE)*. Hersonissos, Crete, Greece, pp. 147–154

Paper V

Synnes, S. A. V., Hansen, R. E., and Sæbø, T. O. (2021). "Spatial coherence of speckle for repeat-pass synthetic aperture sonar micronavigation". In: *IEEE Journal of Oceanic Engineering (Eary Access)*, pp. 1–16

*Torstein O. Sæbø and I had equal contributions on this paper. We were not aware that this could be indicated in the author list, and Torstein ended up first.

Additional Publications

During the preparation of the thesis, I have also authored or contributed to the following papers that are not part of the thesis.

Journal Papers

1. Hansen, R. E., Callow, H. J., Sæbø, T. O., and Synnes, S. A. V. (2011). "Challenges in seafloor imaging and mapping with synthetic aperture sonar". In: *IEEE Transactions on Geoscience and Remote Sensing* vol. 49, no. 10, pp. 3677–3687

2. Blomberg, A. E. A., Austeng, A., Hansen, R. E., and Synnes, S. A. V. (2013). "Improving sonar performance in shallow water using adaptive beamforming". In: *IEEE Journal of Oceanic Engineering* vol. 38, no. 2, pp. 297–307

Conference Papers

1. Sæbø, T. O., Hansen, R. E., Callow, H. J., and Synnes, S. A. V. (2011). "Coregistration of synthetic aperture sonar images from repeated passes". In: *Proceedings of the 4th Underwater Acousitc Measurements (UAM)*. Kos, Greece, pp. 529–536

2. Blomberg, A. E. A., Hansen, R. E., Synnes, S. A. V., and Austeng, A. (2011). "Improved interferometric sonar performance in shallow water using adaptive beamforming". In: *Proceedings of the 4th Underwater Acoustic Measurements (UAM)*. Kos, Greece, pp. 287–292

3. Callow, H. J., Sæbø, T. O., Synnes, S. A. V., and Hansen, R. E. (2011). "SAS beamforming through a vertical sound speed profile". In: *Proceedings of the 4th Underwater Acousitc Measurements (UAM)*. Kos, Greece, pp. 561–568

4. Sæbø, T. O., Synnes, S. A. V., and Hansen, R. E. (2012). "Wideband interferometry in synthetic aperture sonars". In: *Proceedings of the 9th European Conference on Synthetic Aperture Radar (EUSAR)*. Nürnberg, Germany, pp. 1–4

5. Synnes, S. A. V. and Hansen, R. E. (2013). "Ultra wideband SAS imaging". In: *Proceedings of the 1st Underwater Acoustics Conference and Exhibition (UACE)*. Corfu, Crete, Greece, pp. 111–118

6. Lorentzen, O. J., Synnes, S. A. V., Wiig, M. S., and Glette, K. (2013). "Environmentally adaptive sonar". In: *Proceedings of the 1st Underwater Acoustics Conference (UAC)*. Corfu, Crete, Greece, pp. 583–590

7. Geilhufe, M., Dugelay, S., Synnes, S. A. V., Sæbø, T. O., Midtgaard, Ø., and Hansen, R. E. (2014). "Comparative study of frequency dependency in high resolution sonar imagery from the MANEX'13 sea trials". In: *Proceedings of the Institute of Acoustics International Conference on Synthetic Aperture Sonar and Synthetic Aperture Radar (SAS/SAR)*. Lerici, Italy, pp. 191–200

8. Geilhufe, M., Connors, W. A., Synnes, S. A. V., Midtgaard, Ø., Sæbø, T. O., Hansen, R. E., and Dugelay, S. (2015). "Assessment of mine hunting performance evaluation parameters across multiple side-looking sonar systems and frequencies". In: *Proceedings of MTS/IEEE Oceans*. Washington DC, USA, pp. 1–9

9. Vestgården, J. I., Karlsen, M., Synnes, A. S. V., and Lorentzen, O. J. (2016). "Ship wake signatures measured by AUV with upward looking high-frequency sonar". In: *Proceedings of the Underwater Defence Technology (UDT)*. Lillestrøm, Norway, pp. 1–4

10. Synnes, S. A. V., Sæbø, T. O., and Hansen, R. E. (2016). "Interferometry using phase slope estimation". In: *Proceedings of the 11th European Conference on Synthetic Aperture Radar (EUSAR)*. Hamburg, Germany, pp. 1–4

11. Hansen, R. E., Geilhufe, M., Synnes, S., Midtgaard, Ø., and Sæbø, T. O. (2016). "In-situ performance assessment for high frequency seabed imaging sidescan sonar". In: *Proceedings of the Institute of Acoustics Conference on Acoustic and Environmental Variability, Fluctuations and Coherence*. Cambridge, UK, pp. 1–12

12. Hansen, R. E., Sæbø, T. O., Lorentzen, O. J., and Synnes, S. A. V. (2017a). "Mapping unexploded ordnance (UXO) using interferometric synthetic aperture sonar". In: *Proceedings of the 4th Underwater Acoustics Conference and Exhibition (UACE)*. Skiathos, Greece, pp. 687–694

13. Geilhufe, M., Voss, H., Hansen, R. E., Synnes, S. A. V., Midtgaard, Ø., Synnes, S. A. V., and Sæbø, T. O. (2017). "Towards automated HF sidescan sonar performance estimation". In: *Proceedings of the 4th Underwater Acoustics Conference and Exhibition (UACE)*. Skiathos, Greece, pp. 545–552

14. Lorentzen, O. J., Synnes, S. A. V., Hansen, R. E., Sæbø, T. O., and Geilhufe, M. (2017). "Local probability-based phase unwrapping for synthetic

aperture sonar interferometry". In: *Proceedings of the 4th Underwater Acoustics Conference and Exhibition (UACE)*. Skiathos, Greece, pp. 1005–1011

15. Lorentzen, O. J., Synnes, S. A. V., Hansen, R. E., and Sæbø, T. O. (2018). "Investigating layover effects in cross-correlation based interferometry for synthetic aperture sonar". In: *Proceedings of the 12th European Conference on Synthetic Aperture Radar (EUSAR)*. Aachen, Germany, pp. 338–343

16. Hansen, R. E., Sæbø, T. O., Synnes, S. A. V., and Lorentzen, O. J. (2018). "Challenges in coregistration of repeated passes in synthetic aperture sonar". In: *Proceedings of the 12th European Conference on Synthetic Aperture Radar (EUSAR)*. Aachen, Germany, pp. 344–349

17. Geilhufe, M., Hansen, R. E., Midtgaard, Ø., and Synnes, S. A. V. (2019). "Through-the-sensor sharpness estimation for synthetic aperture sonar images". In: *Proceedings of MTS/IEEE Oceans*. Seattle, WA, USA, pp. 1–6

Conference Contributions Without Paper

1. Hansen, R. E., Sæbø, T. O., Synnes, S. A. V., and Lorentzen, O. J. (2017b). "Synthetic aperture sonar interferometry for detailed seabed mapping: Performance considerations". In: *Proceedings of the Acoustics joint meeting, 173rd meeting of the Acoustical Society of America (ASA) and 8th Forum Acusticum of the European Acoustics Association (EAA)*. Boston, USA

2. Sæbø, T. O., Hansen, R. E., Synnes, S. A. V., and Lorentzen, O. J. (2017). "Depth estimation of water column objects using interferometric synthetic aperture sonar". In: *Proceedings of the Acoustics joint meeting, 173rd meeting of the Acoustical Society of America (ASA) and 8th Forum Acusticum of the European Acoustics Association (EAA)*. Boston, USA

Contents

Chapter 1

Introduction

Sonar is the technique of using underwater sound for navigation and ranging. A range profile of the acoustic backscatter can be gathered by transmitting a known signal of sound energy in a burst, called a ping, and examining the received echo for ping replicas (Lurton, 2002).

Synthetic aperture sonar (SAS) is the technique of coherently combining sonar recordings from consecutive pings, acquired from a moving platform, in order to synthesize a longer aperture than the physical aperture operated (Hansen, 2011). The SAS systems usually operate with a side-looking collection geometry. The primary advantage of SAS is that it can support high and range-independent along-track resolution. In contrast, physical aperture sonar has an along-track resolution that degrades proportionally with range. The main challenge of SAS is that the technique requires extremely precise navigation over the full length of the synthetic aperture (Cutrona, 1975; Hansen et al., 2011).

SAS may provide photo-realistic images of the acoustic backscatter over a scene. By operating two vertically displaced sensors, also high resolution depth estimates, called bathymetry, can be obtained. These two data products can be presented and used individually, or fused together to produce astonishing illustrations (Hansen et al., 2017). I give one example image with fused SAS intensity, bathymetry and data quality in Figure 1.1. Another image from Paper I was chosen to decorate the front page of its issue of IEEE Transactions on Geoscience and Remote Sensing.

SAS systems may also collect information that is not presented in SAS intensity images. Wideband and widebeam systems may gather information on how the backscattering changes with frequency and aspect angle. In addition, I consider the interferometric information (applicable to bathymetry) and ping-to-ping signal information (applicable to navigation) such contributions. The extraction and exploitation of such non-imaging information is the main topic of this thesis and constitutes what I herein denote *Advanced SAS* processing.

In the following sections, I first state my research question and present my research community. Then I put my work in a larger perspective by reviewing the development of SAS imaging leading up to high resolution images with photographic resemblance, and into the regime of advanced SAS processing. I examine what constitutes non-imaging information, and how this information is currently being addressed. Then I present my paper contributions, where I explore different approaches for further exploitation of the non-imaging

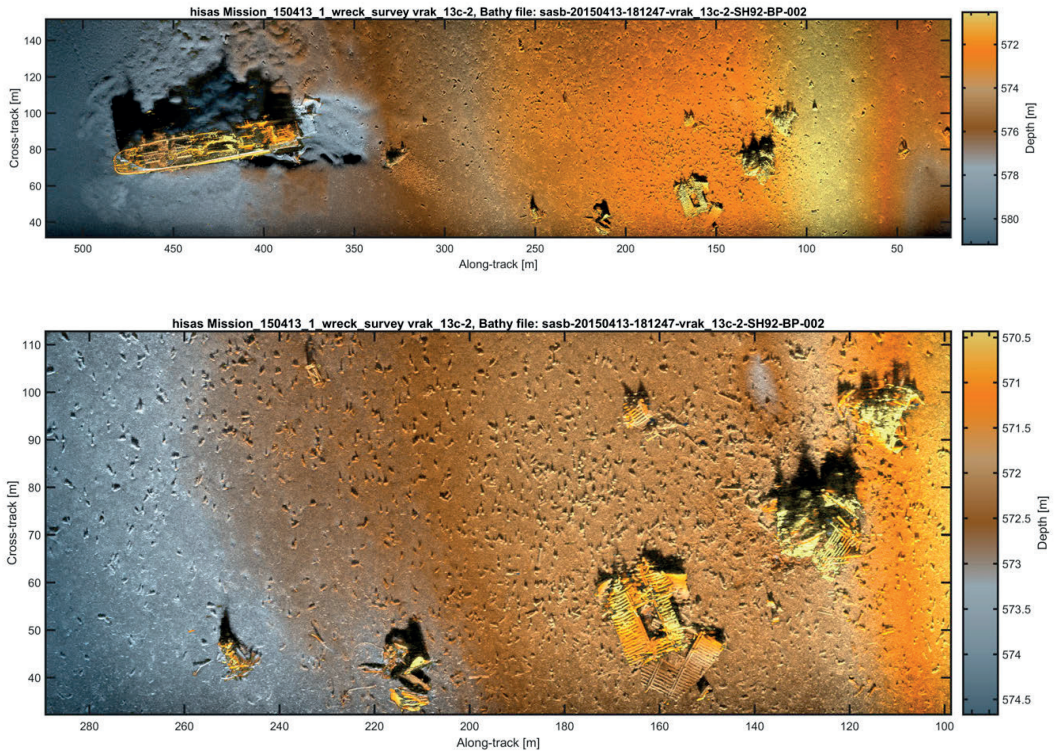

Figure 1.1: A scene from the Skagerrak World War II chemical munitions dump site, illustrating the fusion of SAS image, SAS bathymetry and data quality. The upper panel spans a 500 m × 200 m area covering the wreck of a ship that was filled with bomb shells and sunken after the war. The bow section of the ship has disintegrated and a huge number of bomb shells are spread over a wide area. The lower panel shows a zoom-in on an area with bomb shells and debris. In the images, the bathymetry is represented as color and the backscattering is represented as brightness, while the interferometric coherence is used to emphasize valid data points. *Image: FFI. Data courtesy of the Norwegian Coastal Administration (Kystverket).*

information. I follow up by an overall discussion of my findings in relation to the main research question, before I give a brief summary and conclude.

1.1 Research Question

The research question of this thesis is how to gather, process and exploit the non-imaging information collected by SAS systems.

I will first establish what constitutes this non-imaging information. Then I examine how this information is currently being addressed, before I explore different approaches for further exploitation of the information through the included papers.

1.2 The Norwegian SAS Community

The SAS research in Norway started around 2000 in a collaboration between FFI, Kongsberg Maritime (KM) and the Royal Norwegian Navy (RNoN), as part of a wider collaboration on the development of autonomous underwater vehicles (AUV) (Skogen (ed.), 2005). Through this collaboration, the HUGIN AUV and its primary sensor, the HISAS synthetic aperture sonar, have been developed with important contributions from all three parties. I present a photo of a HUGIN AUV with HISAS in Figure 1.2.

Figure 1.2: A selfie in front of one of the Royal Norwegian Navy's new HUGIN AUVs on board KNM Olav Tryggvason in June 2019. The HISAS synthetic aperture sonar is the dark red inset near the center of the vehicle. *Photo: Stig A. V. Synnes.*

At FFI, the SAS research is performed in the SAS signal processing group, and my colleagues there are all listed in my Acknowledgements. Our work involves a good blend of basic research, development, and experimentation, with both military and civilian applications. In addition to many technical studies documented in FFI reports, we have a significant academic profile with a total volume of more than 10 journal papers and 100 conference papers. Our research has also engaged a number of PhD and master projects.

We have a strong international collaboration, much of which has evolved from the NATO joint research projects (JRP) on mine countermeasures (MCM), organized by what is now the NATO Center for Maritime Research and Experimentation (CMRE).

Through the Norwegian collaboration on SAS, we have participated in the development of KM's HISAS series of SAS systems (Fossum et al., 2008; Hagen et al., 2018; Hansen et al., 2007), and we continue to contribute on new developments. Our SAS research is gathered in FFI's FOCUS SAS processing toolbox (Hansen et al., 2005), which is continuously maintained and extended with new capabilities.

The RNoN is the initial and driving end-user for the Norwegian development of SAS technology. The RNoN has been prototype users of HUGIN AUVs with SAS for mine counter measures (MCM) operations since 2004, and they received their first commercial delivery in 2008 (Hagen et al., 2008; Hagen et al., 2005). The RNoN have also participated in the Standing NATO Mine Countermeasures Group One (SNMCMG1) with MCM vessels equipped with HUGIN AUVs (Waage, 2014). A series of new vehicles was ordered by the RNoN in 2017 (Kongsberg, 2017) and delivered in 2018 – 2020.

FFI acquired one of the commercial HUGIN AUVs in 2008. Our AUV was named HUGIN HUS and has mainly been operated from FFI's research vessel H. U. Sverdrup II. The HISAS 1030 constitutes the primary sensor on the AUV. This HISAS system was extended with a prototype LF transmitter for a period from 2012 (and named HISAS 1031) (Synnes et al., 2013), before the full system was upgraded to the current HISAS 1032 in 2014.

1.3 Larger Perspective

The technique of synthetic aperture sonar has its origin from synthetic aperture radar (SAR), invented in 1951 and first openly published in 1965 (Love, 1985; Wiley, 1965). The first open publication on SAS followed shortly thereafter, and includes a patent from 1969 (Walsh, 1969). The SAS technique became the focus of a wide research community over the following decades (Hayes et al., 2009; Rolt, 1991), and has recently resulted in a wide range of commercial and military SAS systems (Sternlicht et al., 2018).

The initial driving force for the development of SAS was military applications, including naval mine counter measures (MCM) and rapid environmental assessment (REA), as exemplified in (Hagen et al., 2008; Hagen et al., 2005). The SAS technology has later been embraced by the oil industry for pipeline inspection (Hagen et al., 2010; Hansen et al., 2010), and for oil rig decommissioning (Neto et al., 2017). Furthermore, SAS can be used to provide bathymetric maps at high resolution (Griffiths et al., 1997). Though interferometric SAS processing has been presented from several communities (Larsen et al., 2010; Shea et al., 2014; Sæbø et al., 2007), there has lacked a good integration of the bathymetric SAS measurements with the commercial geographic information systems (GIS) that are needed to produce commercial maps (Callow et al., 2012). SAS has been extensively used for wide area search for both historical wrecks and sunken boats, ships, submarines, planes and helicopters. Other applications include monitoring of dumped munitions (Hansen et al., 2019), marine geology (Denny et al., 2015), biotope mapping (Sture et al., 2018) and underwater archeology (Ødegård et al., 2018).

Refining the process of SAS image formation continues to be one of the top SAS research activities. It is expected that we will see an even wider range of SAS applications in the coming years (Sternlicht et al., 2018). The focus on robust processing will continue, and there is an unharvested potential from running more adaptive data collection and processing. Recent trends indicate that we will be seing more sophisticated processing that can support better characterization of both seabed and targets (Hansen, 2013).

1.4 Image Formation

Synthetic aperture sonar imaging is based on exploiting a presumed frequency- and aspect-independence of the backscattering off the scene in order to construct high-resolution images (Jakowatz et al., 1996, Ch. 2), (Hansen, 2011). Synthetic aperture sonar processing coherently combines measurements from the pings that cover (insonify) each portion of the seafloor. In result, range-independent along-track resolution can be approached with SAS, in contrast to the along-track resolution of physical aperture sonar that degrades proportionally with range (Walsh, 1969).

In order to coherently combine SAS measurements, the phase error over the full synthetic aperture must be small compared to the wavelength (Cutrona, 1975). This poses very strict requirements both on the navigation accuracy and on the knowledge of the environmental information. For non-linear tracks, accurate bathymetric information is also essential (Jakowatz et al., 1996, Ch. 3.8), (Hansen et al., 2007), (Sæbø, 2010). Typical SAS imaging systems focus on imaging the seabed and target surface and operates in the high frequency regime of 100 – 400 kHz (Bellettini et al., 2009; Callow et al., 2014).

1.4.1 Challenges and Milestones

The commercial SAS systems of today are based upon a series of historical developments. A good overview and a few key references are provided in the section "Technological milestones and lineage" of (Sternlicht et al., 2018). They summarize that after the invention of SAR in 1951 and the suggestion of adopting the technique for sonar in the late 1960s, SAS had a tremendous potential, but also promised daunting challenges. The idea of using multi-element receiver arrays was proposed in the 1970s, and opened for SAS with practical combinations of speed and range. There was a concern that media turbulence could prevent the formation of SAS images, but during the 1970s and 1980s, experiments instilled confidence that the ocean medium would be sufficiently stable. The burdensome computations needed for SAS image formation was addressed by fast imaging algorithms, pushing forward the SAS technology, until it became less burdensome with newer generations of computers. The 1980s and 1990s saw the evolution of smaller inertial navigation systems (INS) aided by speed measurements from Doppler velocity logs (DVL). In combination with techniques using the phase difference between successive pings (micronavigation), this led to the development of motion estimation techniques that finally could support the sub-wavelength navigation requirements of high frequency SAS. This was combined with auto-focus techniques (adopted from SAR) that could correct residual phase errors from unaccounted platform motion and medium sound speed fluctuations.

The 2000s saw the introduction of interferometric SAS systems (Wang et al., 2001). These systems can provide both physical aperture bathymetric estimates for robust SAS imaging and SAS bathymetry based on the interferometric SAS image pairs (Sæbø, 2010). Sea-surface multipath interference in shallow waters continues to be a nuisance, though some tools have been provided for its mitigation, as noted in (Sternlicht et al., 2018). An in-depth investigation on the challenges of SAS image formation is conducted in (Hansen et al., 2011), examining the impact from navigation errors, sound velocity errors, bathymetric errors for the case of non-linear tracks, and multipath. For the application of SAS for seafloor imaging and mapping, the study concludes that "Although the research on micronavigation has made a major step forward the last decade, navigation is still the most important challenge to overcome." A comprehensive review of the SAS literature up to 2007 is found in (Hayes et al., 2009).

1.4.2 Assumption of Frequency- and Aspect-Invariance

High resolution SAS image formation relies on frequency- and aspect-invariant scattering. The image amplitudes are obtained from the acoustic backscatter, averaged over the processed beamwidth and bandwidth. The SAS images are typically presented as acoustic intensity in a logarithmic scale, and often show details down to a few centimeters throughout a wide swath that can span several hundred meters.

SAS image formation relies on accurate navigation, often achieved by INS navigation, refined by SAS micronavigation. For non-straight trajectories, good image quality also relies on accurate information on the bathymetry.

1.5 Advanced Processing

SAS imaging exploits a presumed frequency- and aspect-invariance of the backscattering from the scene. With narrowband and narrowbeam systems, all the gathered data may contribute coherently to improve the image resolution. With large bandwidth and beamwidth, the data also represent information on the frequency- and aspect-dependence of the scattering, and the full spectrum does not necessarily combine coherently to improve the image resolution.

The backscattering off targets can have a strong dependence on both frequency and aspect angle. If the target response changes significantly over the processed angles, this will reduce the signal-to-noise ratio (SNR) and can lead to erroneous estimations of the target strength if the assumption of aspect invariance is used. However, the scattering strength as function of frequency and aspect angle may provide additional information on targets and the scene, which in many cases can be extracted through dedicated advanced SAS processing.

The backscattering off the seafloor will often incorporate multiplicative speckle statistics, resulting from a random distribution of scatterers within each theoretical resolution cell (Oliver et al., 1998, Ch. 4.3). This speckle pattern changes both with the angles from which the scene is observed and with frequency (Jakowatz et al., 1996, Ch. 3.3).

In the remainder of this section, I list some of the potential fields of advanced signal processing on data from SAS systems that might take advantage of the above two features, many of which are believed to be important parts of future SAS processing (Hansen, 2013; Sternlicht et al., 2018). I group the techniques depending on whether they address the frequency- and aspect-dependence (typically of targets), or whether they address the spatial coherence of speckle (typically on the background).

1.5.1 Frequency- and Aspect-Dependence

SAS processing relating to frequency- and aspect-dependence include these areas of advanced SAS processing:

- Low frequency SAS: Low frequencies can provide bottom and target penetration, and potential target resonances at low frequencies (Piper et al., 2002; Williams et al., 2010).
- Multiband: SAS systems that covers a wide frequency span might allow for easier discrimination between seafloor surface and sub-surface scattering (Geilhufe et al., 2014; Sternlicht et al., 2011). Multiband systems operated from small to medium size AUVs often include a LF band around 10 – 40 kHz and a HF band around 100 – 400 kHz (Groen et al., 2015; Piper et al., 2002; Synnes et al., 2013).
- Frequency-dependence: The frequency-dependence of the backscattering is related to e.g. acoustic properties and surface roughness (Jackson et al., 2007), but also thickness (Fiorito et al., 1979) and geometric shape (Brooker, 2009, chapter 9.3). Knowledge on the frequency dependence might provide information on these metrics.
- Frequency- and aspect-dependence: Wideband data at low frequencies and a wide range of aspects can be collected and investigated. One such application is the examination for characteristic target resonances and returns in the averaged response over a target area (Williams et al., 2010).
- Circular SAS: Full aspect circular SAS (CSAS) is provided in (Marston et al., 2016). Data from wideband CSAS could be the ideal starting point for analyzing frequency- and aspect-dependence.
- Aspect-dependence: The aspect-dependence of the backscattering can be used to estimate the orientation and size of scatterers (Allen et al., 1994). It can also be used to improve both imaging and target recognition for partially occluded targets (Allen et al., 1995).
- Multi-aspect SAS: Dividing a widebeam or CSAS recording into multiple narrow beams centered around different aspects can give images with different highlights and shadows, that can provide complementary information to the total coverage image (Cook et al., 2001). Visualization of aspect by color on CSAS data is presented in (Plotnick et al., 2018), and enhancement of the shadow from a target through fixed focusing is developed in (Groen et al., 2009).

1.5.2 Spatial Coherence of Speckle Background

SAS processing that takes advantage of the spatial correlation/decorrelation of speckle include a number of areas of advanced SAS processing:

- Interferometry: Interferometric estimation of the terrain is well established both in SAR and SAS (Bamler et al., 1998; Sæbø, 2010). Current research includes higher resolution mapping for use with rough terrain and on small targets (Lorentzen et al., 2020). Interferometry has an inherent 2π ambiguity, which usually is addressed by phase unwrapping techniques (Ghiglia et al., 1998; Yu et al., 2019), which enforce assumptions on e.g. continuity. Alternatively, the signal bandwidth can be used to resolve the ambiguity, following (Madsen et al., 1992).
- Multipath assessment and mitigation: Assessment, analysis and experimental validation of multipath contamination is addressed in e.g. (Bellettini et al., 2003; Synnes et al., 2009). Different techniques for mitigating the impact of multipath have been suggested, and the technique of using adaptive vertical beamforming on two, three or multiple arrays appears promising (Blomberg et al., 2013; Pan et al., 2016).
- SAS micronavigation for image formation: SAS micronavigation for image formation by estimating the sway motion was introduced with (Raven, 1981). The technique was later refined by adopting heading estimates from INS (Bellettini et al., 2002; Bellettini et al., 2009; Wang et al., 2001). Even so, techniques for adaptive image enhancement adopted from SAR, such as phase gradient autofocus (PGA), could in many cases reveal an unexploited potential and provided benchmarks and motivation for further research on both SAS micronavigation (Callow, 2003) and image quality assessment (Callow et al., 2005).
- SAS micronavigation as input to an INS: SAS micronavigation by estimating both the sway and the surge motion was first described in 1978 (Dickey, 1981) and was demonstrated in 2001 (Wang et al., 2001). After development by FFI and industrialization by KM, the collaboration achieved SAS micronavigation aiding with an accuracy that surpassed that of the state of the art DVLs (Kongsberg, 2019), with the first system delivered late in 2020 with the HUGIN Superior AUV. SAS micronavigation can also provide micronavigation updates between passes (Hunter et al., 2015; Synnes et al., 2010). One operational concept that takes advantage on these measurements is suggested in (Hunter et al., 2017).
- Speckle reduction: Speckle is observed as multiplicative intensity variations on the backscattering off a scene. These variations can make it difficult to interpret synthetic aperture images, but they can be reduced at some cost. A tutorial on speckle reduction in SAR is given in (Argenti et al., 2013). The effect of different techniques for speckle reduction (or despeckling) has been demonstrated on SAS (Austeng et al., 2013; Chaillan et al., 2007).

Chapter 2

Publications

In this chapter I first present and summarize each of the included papers. Then I follow up with an up-to-date literature review on the topics of each paper.

2.1 Summary of the Included Papers

This section summarizes the research topic, motivation, claim, method and result of the included publications.

2.1.1 Paper I

Sæbø, T. O., Synnes, S. A. V., and Hansen, R. E. (2013). "Wideband interferometry in synthetic aperture sonar". In: *IEEE Transactions on Geoscience and Remote Sensing* vol. 51, no. 8, pp. 4450–4459

Paper I investigates the refinement of SAS bathymetry on complicated scenes from using wideband information. High precision bathymetric measurements can be obtained from the interferometric phase difference between two observations with a vertical baseline, but these interferometric estimates possess a depth ambiguity that originates from the unknown 2π wrap of the phase difference. The ambiguities can be attempted resolved by using a 2D phase unwrapper to produce a continuous surface, though this will incorporate an assumption on continuity that might be erroneous, in particular on complex scenes. We address an alternative approach of using wideband information to estimate the absolute phase, thereby approaching ambiguity-free bathymetric estimates.

Initially, we estimate the potential performance of (non-adaptive) wideband estimators by evaluating the probability of correct wrap of a maximum likelihood time delay estimator as a function of relative bandwidth and SNR. In the remainder of the paper, we evaluate three existing and one new method of estimating the absolute phase difference. Complex cross-correlation based bathymetry evaluates the interferogram for many sub-wavelength registration offsets, estimates the correct wrap from the lag of maximum coherence, and uses the related interferometric phase for precision. Both the split spectrum algorithm and the multi-chromatic approach splits the interferogram into subbands and estimate the frequency-dependent rate of change between bands. We extend the split-spectrum algorithm to multiple bands, inspired by the multi-chromatic approach, and introduce adaptive weighting between the different combinations of bands. The weights are chosen based on the estimated variance of the time

delays and the separation of the bands such that the combined result minimizes the variance of the absolute phase estimate.

While interferometry can be used with a priori co-registration to within a fraction of the resolution cell, a co-registration to within a fraction of the half-wavelength is needed to assert the correct wrap. The method of complex cross-correlation searches over multiple lags, while the multiband methods rely on an a priori co-registration to within roughly the systems range resolution. We observe that the complex cross-correlation is thus more robust, but as it constitutes a higher order method, it has a higher number of erroneous measurements than the other methods for areas where the initial co-registration is within the requirements of the multiband methods. For these areas, the coarse co-registration constitutes a priori knowledge which complex cross-correlation does not have.

Our suggested weighted multiband extension of the split-spectrum approach supports fast and effective absolute phase estimation where the initial co-registration is within the requirements of the method, and the method performs better on real data with our suggested adaptive weights.

2.1.2 Paper II

Synnes, S. A. V., Hunter, A. J., Hansen, R. E., Sæbø, T. O., Callow, H. J., Vossen, R. van, and Austeng, A. (2017). "Wideband synthetic aperture sonar backprojection with maximization of wave number domain support". In: *IEEE Journal of Oceanic Engineering* vol. 42, no. 4, pp. 880–891

Paper II examines the support and quality of frequency- and aspect-dependent information available from SAS systems with three different SAS backprojection (BP) imaging algorithms. With narrowband and narrowbeam systems, all the gathered data may contribute coherently to improve the image resolution. With large bandwidth and beamwidth, the data also represent information on the frequency- and aspect-dependence of the scattering, and the full spectrum does not necessarily combine coherently to improve the image resolution. Therefore, the data quality cannot be estimated from one fullband spatial domain image. Also, any image formation relies on using a windowing function for compromising between resolution and suppression of sidelobes and grating lobes, thereby incorporating application-dependent design choices.

We suggest an approach for isolating the operation of the imaging algorithm from the impact of sensor and scene to obtain the means for examining both the data support and the data quality supported by sensor and algorithm. We apply a 2D Fourier Transform on the image and obtain a wavenumber domain representation, where the frequency- and aspect-dependence can be isolated by using polar coordinates. We develop wavenumber domain counterparts of some common spatial domain quality metrics, and use these to evaluate how

the different imaging algorithms use the information on the scene provided by wideband widebeam SAS systems. We address the signal-to-ambient-noise ratio and the signal-to-grating-lobe ratio. Because SAS arrays often are under-sampled along-track, we pay particular attention to data degradation from aliasing. We map the data quality for a typical SAS system design used in combination with different SAS BP imaging algorithms. This allows us to evaluate how different imaging algorithms use the information on the scene that is provided by a wideband widebeam SAS system. We find that the widebeam back projection (WBP) provides the maximum support of information on the frequency and aspect dependence, though at an additional computational cost.

2.1.3 Paper III

Synnes, S. A. V. and Hansen, R. E. (2015). "Aspect-dependent scattering in widebeam synthetic aperture sonar". In: *Proceedings of the 3rd Underwater Acoustics Conference and Exhibition (UACE)*. Chania, Crete, Greece, pp. 129–136

Paper III investigates aspect-dependent scattering in widebeam synthetic aperture sonar. The backscattering of physical structures can show a strong angular dependence over the beamwidth covered by widebeam systems. During SAS imaging, the contributions from all aspect angles are focused into each image pixel, though for well sampled complex images, this information is preserved and can be retrieved. Extracting this aspect-dependence of the scattering can provide information on the orientation and size of facets, which may be used for target detection and classification.

We investigate the aspect-dependence of the backscattering going into each pixel, using an approach based on adaptive matched filter feature extraction developed in synthetic aperture radar (SAR). We demonstrate the method on SAS data recorded from a HUGIN autonomous underwater vehicle using a HISAS system with a prototype low frequency transmitter covering the band 12-38 kHz with a -3 dB beamwidth exceeding 100 degrees at the center frequency. Assuming uniform linear scatterers with size larger than the wavelength, we apply match filtering for scatterers of different length in a polar coordinate wavenumber domain representation. We get a good match for scatterers for which the facet broadside falls within the sensors beamwidth, and generate maps that present the estimated facet lengths and facet orientations.

2.1.4 Paper IV

Synnes, S. A. V. and Lorentzen, O. J. (2019). "Calibration target for estimation of frequency dependence in synthetic aperture sonar". In: *Proceedings of the 5th Underwater Acoustics Conference and Exhibition (UACE)*. Hersonissos, Crete, Greece, pp. 147–154

Paper IV develops a SAS calibration target that can provide ground truth on both strength and frequency dependence of the backscatter, while minimizing variations with aspect angle. Better discrimination of different materials and other physical properties might be supported by wider bandwidth and lower frequency SAS images. The suggested calibration target can constitute a benchmark for validation of algorithms exploring this potential.

We suggest an extended calibration target consisting of reflectors with different combinations of scattering strength and frequency dependence. Deterministic frequency dependencies are assured by using solid objects of various geometrical shapes and different targets strengths are obtained by using replicas of different size. Any aspect-dependence is minimized by choosing targets with an acoustic point target response where possible. We gather theory for acoustic interaction with a submersed metal plate and for a set of acoustic scatterers that can be mounted onto it. We validate the theory using measurements at different frequencies and geometries on a prototype target, and suggest a refined design of a calibration target that should be well suited to validate algorithms intended to extract the frequency dependence of the scattering over a scene.

2.1.5 Paper V

Synnes, S. A. V., Hansen, R. E., and Sæbø, T. O. (2021). "Spatial coherence of speckle for repeat-pass synthetic aperture sonar micronavigation". In: *IEEE Journal of Oceanic Engineering (Eary Access)*, pp. 1–16

Paper V examines the spatial coherence of speckle seafloor as encountered by SAS systems. The acquired information can be used for accurate positioning of AUVs, both ping-to-ping and between passes. Important applications include mitigation of drift, coherent change detection and repeat-pass SAS interferometry.

We divide the different contributions to spatial decorrelation into the three groups of speckle decorrelation, footprint mismatch and stretching. We examine each contribution separately and develop simplified formulas for their decorrelation baselines. We demonstrate good agreement of spatial decorrelation estimates from the numerical evaluations, our simplified formulas and experimental results.

While spatial decorrelation from stretching is most prominent for synthetic aperture images, we show that for the correlation of single element data, speckle decorrelation dominates with the low grazing angles common to SAS. We demonstrate increasing the across-track baseline of successful repeat-pass SAS micronavigation updates from the less than 1 meter reported in previous studies to more than 10 meters. We show that this can only be achieved by combining elements into larger effective elements, and that it is more easily obtained for patches at long range. In addition, we evaluate the relation between stretching and decorrelation, and we derive a lower limit on the expectation value for

estimating coherence values through cross-correlation.

2.2 Updated Literature Review

In this section, I give an up-to-date review on the topics of each paper. The work on the papers has spanned over one decade, and I find it interesting both to examine how the papers have been addressed, and how the progress has been in the covered topics. I also include a wider literature review on the topic of Paper IV, as the literature review included in this conference paper was rather brief.

2.2.1 Paper I

This journal paper investigates the refinement of SAS bathymetry on complicated scenes from using wideband information. The paper was awarded with the front page of the journals special issue on SAR, as illustrated in Figure 2.1.

Our study expands on established wideband methods developed for processing interferometric SAR. One of the primary methods is that of *split-bandwidth interferometry* (Madsen et al., 1992) of the NASA/JPL, adopted by the German Aerospace Center (DLR) and re-branded the *split-spectrum algorithm (SSA)* (Bamler et al., 2004) for processing of TerraSAR-X interferometry data. Another is the *multi-frequency interferometry* (Pascazio et al., 2002; Xu et al., 1994), adopted and re-branded the *multi-chromatic approach (MCA)* (Veneziani et al., 2003) and advocated in Italy and used in their SAR interferometry programme.

My updated literature review indicates that these methods were developed and established between 1992 and 2010, confirming the impression of our original literature review. For SSA we appear to have missed the papers using the terminology of *spectral diversity (SD)* (introduced with (Amin, 1993)) and used for SAR interferometry e.g. in (Scheiber et al., 2000). The terminology of spectral diversity appears to be preferred for the application of measuring surface displacement of land slides, a review of which is given in (Mastro et al., 2020). SSA is also reviewed in (Jiang et al., 2017) under its original name of split-bandwidth interferometry, though this review only covers references from the years 2000 - 2009. The same paper also addresses the use of cross-correlation for interferometry. Both cross-correlation and spectral diversity are also addressed in (Wang et al., 2017).

An updated review on phase unwrapping in interferometric SAR addressing narrowband phase-unwrapping and absolute phase estimation based on multi-baseline recordings is provided in (Yu et al., 2019). They show that the research on multi-baseline interferometry is an active field for the application of satellite based SAR measurements from multiple passes. While the review paper does not cover the use of bandwidth for absolute phase unwrapping, they show that the application of MCA (which can be applied both for multiband and multi-

Figure 2.1: An image from our paper was chosen to decorate the front page of the SAR special issue of IEEE Transactions on Geoscience and Remote Sensing. *© 2013 IEEE. Reprinted, with permission.*

baseline interferometry) is an active method area of research with applications to multibaseline SAR. One late example is (Libert et al., 2017), where the method is briefly reviewed before it is used on persistent scatterers and attempted re-branded *split-band interferometric SAR (SBInSAR)*.

Within the field of sonar, our paper is cited in a review article on methods for interferometric echo sounding (Grall et al., 2020). The only work that attempts to expand on our method appears to be my own (Synnes et al., 2016). As of January 2021, the other 15 citations on Web of Science are only referring to general SAS interferometry, as are the additional 12 citations on Google Scholar (which includes references to our preceding conference paper (Sæbø et al., 2012)).

Except for the applications of wideband methods on SAS and SAR interferometry, SSA has also been used for image co-registration and for the estimation and mitigation of ionospheric dispersion at microwave frequencies (Mastro et al., 2020). While adaptive weighting of multiple bands is common for applications of MCA in SAR, I have not been able to verify that the same is the case for applications of SSA in SAR. This indicates that our adaptively weighted multiband SSA (WSSA) could still have an impact on SAR if adopted.

2.2.2 Paper II

This journal paper is four years old, and the literature review is not obsolete. I therefore only examine the citing papers.

The journal paper has one citation for wavenumber domain filtering for (the application of classification supported by) sub-view and sub-band feature extraction (Xenaki et al., 2019). The other six citations as of January 2021 on Web of Science (8 citations on Google Scholar) is only referring to time domain SAS image formation, or even referring to SAS in general.

Our preceding conference paper (Synnes et al., 2013) is not included by Web of Science, but has five citations on Google Scholar, and I know of one additional citation. One of these citing papers is the enclosed Paper III, where I apply the wideband processing scheme in order to maximize the wavenumber domain support of valid data. Another is (Groen et al., 2015), that goes one step further and examines the wideband processing scheme with respect to resolution, sidelobe level and SNR, before applying the wideband processing scheme on dual band SAS processing. Two other papers refer to the reported HISAS HF/LF prototype (Callow et al., 2014; Geilhufe et al., 2015), one refers to the relation of processed beamwidth and frequency for achieving a fixed resolution (Hansen, 2013), while the final is our follow-up journal paper.

2.2.3 Paper III

In this paper, we apply adaptive matched filtering in order to estimate size and orientation of the dominating scatterers (assumed planar) for each pixel. The technique was adopted from SAR, though our literature review showed that the technique was not widely applied.

As of January 2021, the three primary references of our conference paper have gained six new citations on Web of Science and an additional six on Google Scholar. There appears to be some interest on the technique for circular SAR and for SAR systems operating at terahertz frequencies (which appears to favor sub-aperture imaging). I note that (Hu et al., 2017) attempts at an effective implementation of matched filtering that is based on 2D FFT. I also noticed that (Kapoor et al., 1996) has a suggestion on filter selection based on SNR.

Our paper is not covered by Web of Science, but on Google Scholar it has three citations. Two of the citations refer to potential applications of the method, while (Synnes et al., 2016) investigates an adaptation of the method for interferometry. The closest I have come matched filtering in the SAS literature is (Plotnick et al., 2018), where they divide a circular SAS image into a stack of low-resolution images at different aspect angles, though they only color-code the contributions as they combine them in one composite image.

Lately, I have also become aware that a similar technique is applied in medical ultrasound under the name of *specular beamforming* (Rodriguez-Molares et al., 2017).

2.2.4 Paper IV

One of the main purposes of the conference paper was that it should work as a design document for the production of a calibration target. Following the publication of the paper, we had a target produced by FFI's Prototype Workshop, of which a photo is shown in Figure 2.2. It was designed for frequencies around 100 kHz, is made of aluminium, measures 80 cm x 120 cm and weighs 79 kg.

Figure 2.2: My realization of the suggested calibration target, produced by FFI's Prototype Workshop. *Photo: Stig A. V. Synnes.*

The paper is rather recent, though it did not comprise an in-depth literature review, so I add some information on the use of calibration targets.

In radar, calibration targets are extensively used both for absolute calibration and for estimation of the point spread function (from which both the geometrical resolution and other performance metrics can be derived) (Curlander et al., 1991,

Ch. 7). The trihedral corner reflector is often chosen, but a number of reflector shapes are used based on their different advantages regarding e.g. directivity and target strength as function of size (Curlander et al., 1991, Ch. 7), (Brooker, 2009, chapter 9.3).

In sonar, absolute calibration of the systems is well established for oceanography and fishery, where a potential accuracy of 0.1 dB at single frequencies is achieved using copper or tungsten carbide spheres. In tank experiments, an average precision of 0.2 dB has also been reported over the frequency interval from 50 kHz to 150 kHz (Islas-Cital et al., 2010). The use of different types of spherical objects as calibrated mine hunting sonar targets has been examined in (Anstee, 2002). To my knowledge, none of the current SAS systems are absolutely calibrated, except from the rail-based system of (Williams et al., 2010), though calibration is believed to be beneficial for seabed and target characterization (Hansen, 2013).

In SAS, different compound targets have been applied to demonstrate the spatial resolution of the systems. These typically including multiple reflectors with different spacings, as for the targets in (Austeng et al., 2012; Groen et al., 2015; Hansen, 2019).

The frequency dependency of a targets scattering strength is known to be a function of target shape (or curvature). The usual approach is to evaluate the scattering strength at one frequency, and not to address the frequency-dependency directly as we suggest. Only just before printing the thesis, I was able to locate (Gerry et al., 1999) that relates the frequency dependency of the scattering to the geometrical shape of targets. I recommend that any follow-up studies also examine their work.

2.2.5 Paper V

This journal paper was published by IEEE Journal of Oceanic Engineering on 31 May 2021 online as Early Access, and will be included in an upcoming issue of the journal. The literature review of the manuscript is fully up to date.

Chapter 3

Discussion

Throughout this thesis I have addressed information from SAS that is complementary to that presented in the common high resolution SAS intensity images. In the introduction I established what constitutes this information and how it is currently exploited. Ideally, I would follow up with the optimal processing for extracting and exploiting this information in my papers. However, what is optimal depends on the optimization criterium, which again depends on the application. And also, the quality of the data available is a function both of the data collection and of the data processing. In my papers, I have therefore investigated how the data quality depends on both SAS system and collection geometry, how to maximize the information collected, and how to exploit the information available in selected applications.

3.1 Non-Imaging Information

What constitutes the non-imaging information available?

I have established that the non-imaging information gathered by SAS systems can include both the frequency- and aspect-dependence of the backscattering (usually from targets), and the spatial coherence of speckle (usually on the background).

How is this information currently addressed?

In the introduction I identified a number of established fields of SAS processing that relies on this information: The frequency- and aspect-dependence is addressed in low frequency, multiband and wideband SAS, and widebeam and circular SAS. The spatial coherence of speckle is exploited in interferometry, multipath assessment and mitigation, speckle reduction, and SAS micronavigation.

3.2 Collection and Representation

How can the information be gathered and preserved?

Through Paper II, I examined the support and quality of frequency- and aspect dependent information available from SAS systems. The same SAS receiver arrays are usually employed over the entire frequency band. Because the acoustic beamwidth increases with frequency, special care must be taken to avoid aliasing at the highest frequencies when acquiring the full beamwidth at the lowest

frequencies. We showed that after representing all the data in a high resolution grid, most of the high quality data can be filtered out in the wavenumber domain and stored in a lower resolution (still Nyquist-sampled) complex SAS image. The proposed wideband backprojection algorithm constitutes one realization of the above. The resulting complex SAS image preserves the collected high quality data, and can be used both for analysing any frequency- and aspect dependence, and for generating SAS intensity images by applying a window function covering a desired selection of frequencies and aspect angles.

Through Paper V, I addressed both challenges and fundamental limitations related to using the spatial correlation of speckle for micronavigation. When operating SAS micronavigation on single element data, the strong speckle decorrelation with across-track baseline imposes practical limitations both on sway motion and on yaw crabbing angle. We showed that the best data for accurate navigation is gathered when both the sway motion and the crabbing angle are kept small, but also that longer across-track baselines can be handled by combining neighbour elements into larger effective ones, at the cost of increasing the along-track navigation error. Exploring the latter trade-off should open for practical operations of repeat-pass SAS micronavigation, and the relation may also be used to optimize SAS micronavigation when running on widebeam (low frequency) systems.

In Paper V, we showed that decorrelation from stretching becomes increasingly important with larger across-track baselines and grazing angles. The findings apply to single elements and long synthetic apertures alike, and thus also to SAS interferometry on slant-range SAS images. Wavenumber stretching can be reduced by de-stretching the time series, e.g. by making ground range SAS images, or by using shorter time series at the cost of an increased coherence floor. The more fundamental decorrelation from wavenumber mismatch might prevent use of the largest baselines and grazing angles.

3.3 Wideband and Widebeam Systems

How to get the most out of frequency- and aspect coverage?

During the work on Paper III, I came to realize that the analysis of aspect-dependence is most powerful if the system beamwidth covers 90 degrees or more. The specular reflection off targets can be orders of magnitude stronger than that of the corresponding diffuse scattering. A two-sided SAS system with beamwidth $\beta > \pi/2$ operated in a line pattern will acquire the specular reflection at least from one side of most extended targets. By running two orthogonal line patterns, the full 360 degrees coverage is collected throughout the scene, and the specular reflection can be acquired for any orientation. An alternative way of acquiring the full aspect coverage is to run circular SAS on dedicated smaller areas.

The performance of SAS micronavigation is also a function of the system

beamwidth, as detailed in Paper V. SAS micronavigation relies on ping data from overlapping acoustic footprints, observed from the same azimuth direction. A larger beamwidth will support processing on consecutive pings with larger turn rates, and processing on pings from different passes with larger relative headings. However, a larger beamwidth will also increase the decorrelation with across-track baseline. This might call for combining neighbour elements, which in turn affect the along-track navigation error.

For the analysis of frequency-dependence, I do not hold the same in-depth experience as for the analysis of aspect-dependence. I recognize that the interaction between the acoustic signal and a target may change rapidly at low frequencies in particular. These variations might be picked up by multiband SAS systems, though I argue that it must be better to use a wide continuous band. A system with large ratio of bandwidth to maximum frequency (B/f_{max}) would more likely collect non-imaging information. I would therefore like to further explore low frequency wideband systems bandwidth $B > f_{\max}/2$.

The robustness of SAS bathymetry estimates can benefit strongly from large ratios B/f_{max}. In Paper I, we showed that the probability of estimating the correct wrap by absolute phase estimation is significantly increased for systems approaching and passing $B > f_{\max}/2$.

Repeat-pass micronavigation and repeat-pass interferometry can also benefit from larger values of B/f_{max}, as the decorrelation with change of grazing angle is lower than for more narrowband systems, c.f. Paper V.

3.4 Exploitation and Applications

How have I exploited more of the information in selected applications?

In Paper I, we have resolved bathymetric ambiguities from the rate at which the interferometric phase changes with frequency. We expanded on the existing multi-band methods through using the full bandwidth and through using adaptive weights on the data quality. Still, our estimates were made at reduced resolution. More details could be available with higher resolution estimates, but potentially at the cost of reducing the tolerance to initial miss-registration. A full resolution estimate was initiated in my follow-up study of (Synnes et al., 2016), mentioned in Section 2.2.1.

In Paper III, we estimated the aspect dependence of the scattering, evaluated at each pixel from the contributions from all aspects within the beamwidth. We successfully adopted the technique from SAR and demonstrated estimating both orientation and size of planar scatterers. I recognize that such high resolution estimation of the aspect-dependence can provide important information on targets in particular. Though we made some speed improvements, our implementation is still rather slow, and a fast FFT-based approach should be sought to open for

wider use.

It would be very interesting to follow up Paper III by estimating the frequency-dependence of the scattering for each pixel. I intended to do such a follow-up study, as mentioned in Paper IV. However, extracting information per pixel on the frequency-dependence proved more difficult than it was for the aspect-dependence. In addition, I found that we were in need of a calibration target with ground-truth for validation of such an algorithm. This was followed up through Paper IV, where we developed a SAS calibration target that can provide ground truth on both frequency dependence and absolute target strength, while minimizing the aspect dependence.

In Paper V, we investigated the spatial correlation of speckle for the application of repeat-pass SAS micronavigation. We identified the different contributions to spatial decorrelation, and quantified their impact. By adjusting the processing, we were able to increase the feasible across-track baseline between passes from less than 1 meter to 10 meters.

Chapter 4

Summary and Conclusion

In this thesis I have addressed how to gather, process and exploit the information that is collected by SAS systems but not reflected in SAS intensity images. This includes information both on the frequency- and aspect dependence of the backscattering and on the spatial coherence of speckle. I have chosen to denote techniques addressing and exploiting this information for *Advanced SAS* processing.

In the introduction, I have established how this non-imaging information is currently being addressed. In the included papers, I have investigated how the quality of this data depends on the SAS system and the collection geometry, how to maximize the information collected, and how to exploit the information available in selected applications.

I have performed an in-depth analysis on the support and quality of frequency- and aspect-dependent information available from SAS systems in Paper II. I have also conducted a detailed analysis on the spatial correlation of speckle, its impact to SAS micronavigation and some implications to SAS interferometry in Paper V.

The study on frequency- and aspect dependent information was addressed through improved bathymetric estimates in Paper I, extraction of aspect dependence in Paper III, and a validation target for extraction of frequency dependence in Paper IV. In the discussion I have argued that wideband and widebeam systems with beamwidth $\beta > \pi/2$ and bandwidth $B > f_{\max}/2$ should be well suited for taking benefit of the aspect- and frequency-dependence of target scattering.

The investigations on spatial correlation in Paper V had a direct impact on the feasibility of SAS micronavigation between repeated passes, where we were able to increase the practical across-track baseline between the passes from less than 1 meter to 10 meters. This should open for a wider range of operations for repeat-pass SAS micronavigation.

References

Allen, M. R., Jauregui, J. M., and Hoff, L. E. (1995). "FOPEN-SAR detection by direct use of simple scattering physics". In: *Proceedings of the IEEE International Radar Conference*. Alexandria, VA, USA, pp. 152–157.

Allen, M. R., Phillips, S. A., and Sofianos, D. J. (1994). "Wide-angle SAR matched filter image formation for enhanced detection performance". In: *SPIE 2093, Substance Identification Analytics*. Innsbruck, Austria, pp. 381–387.

Amin, M. G. (1993). "Introducing the spectral diversity". In: *IEEE Transactions on Signal Processing* vol. 41, no. 1, pp. 185–193.

Anstee, S. (2002). *Use of spherical objects as calibrated mine hunting sonar targets*. Tech. rep. DSTO-TN-0425. DSTO, Australia.

Argenti, F., Lapini, A., Alparone, L., and Bianchi, T. (2013). "A tutorial on speckle reduction in synthetic aperture radar images". In: *IEEE Geoscience and Remote Sensing Magazine* vol. 1, no. 3, pp. 6–35.

Austeng, A., Callow, H. J., Larsen, Y., and Hansen, R. E. (2013). "Speckle reduction in synthetic aperture sonar images using Thomson's multitaper approach". In: *Proceedings of the 1st Underwater Acoustics Conference (UAC)*. Corfu, Crete, Greece, pp. 1–8.

Austeng, A., Jensen, A. C., Nilsen, C.-I. C., Callow, H. J., and Hansen, R. E. (2012). "Use of the minimum variance beamformer in synthetic aperture sonar imaging". In: *Proceedings of the 11th European Conference on Underwater Acoustics (ECUA)*. Edinburgh, Scotland.

Bamler, R. and Eineder, M. (2004). "Split band interferometry versus absolute ranging with wideband SAR systems". In: *Proceedings of the IEEE International Geoscience and Remote Sensing Symposium (IGARSS)*. Anchorage, Alaska, pp. 980–984.

Bamler, R. and Hartl, P. (1998). "Synthetic aperture radar interferometry". In: *Inverse Problems* vol. 14, R1–R54.

Bellettini, A., Pinto, M., and Wang, L. (2003). "Effect of multipath on synthetic aperture sonar". In: *Proceedings of the World Congress on Ultrasonics (WCU)*. Paris, France, pp. 531–534.

Bellettini, A. and Pinto, M. A. (2002). "Theoretical accuracy of synthetic aperture sonar micronavigation using a displaced phase-center antenna". In: *IEEE Journal of Oceanic Engineering* vol. 27, no. 4, pp. 780–789.

Bellettini, A. and Pinto, M. (2009). "Design and experimental results of a 300-kHz synthetic aperture sonar optimized for shallow-water operations". In: *IEEE Journal of Oceanic Engineering* vol. 34, no. 3, pp. 285–293.

Blomberg, A. E. A., Austeng, A., Hansen, R. E., and Synnes, S. A. V. (2013). "Improving sonar performance in shallow water using adaptive beamforming". In: *IEEE Journal of Oceanic Engineering* vol. 38, no. 2, pp. 297–307.

Brooker, G. (2009). *Introduction to Sensors for Ranging and Imaging*. 1st ed. Scitech Publishing. Chap. 8, p. 740.

Callow, H. J., Sæbø, T. O., and Hansen, R. E. (2005). "Towards robust quality assessment of SAS imagery using the DPCA algorithm". In: *Proceedings of Oceans Europe*. Brest, France, pp. 1–6.

Callow, H. J. (2003). "Signal Processing for Synthetic Aperture Sonar Image Enhancement". PhD thesis. University of Canterbury, Christchurch, New Zealand, pp. 1–273.

Callow, H. J., Espen, P., and Hansen, R. E. (2014). "Operating frequency trade-offs in the design of high resolution synthetic aperture sonars for small platforms". In: *Proceedings of the Underwater Defence Technology (UDT)*. Liverpool, United Kingdom, pp. 1–9.

Callow, H. J., Hagen, P. E., Hansen, R. E., Sæbø, T. O., and Pedersen, R. B. (2012). "A new approach to high-resolution seafloor mapping". In: *Journal of Ocean Technology* vol. 7, no. 2, pp. 13–22.

Chaillan, F., Fraschini, C., and Courmontagne, P. (2007). "Speckle noise reduction in SAS imagery". In: *Signal Processing* vol. 87, pp. 762–781.

Cook, D. A., Christoff, J. T., and Fernandez, J. E. (2001). "Broadbeam multi-aspect synthetic aperture sonar". In: *Proceedings of MTS/IEEE Oceans*. Honolulu, HI, USA, pp. 188–192.

Curlander, J. C. and McDonough, R. N. (1991). *Synthetic Aperture Radar System and Signal Processing*. John Wiley & Sons, Inc, p. 647.

Cutrona, L. J. (1975). "Comparison of sonar system performance achievable using synthetic-aperture techniques with the performance achievable by more conventional means". In: *The Journal of the Acoustical Society of America* vol. 58, no. 2, pp. 336–348.

Denny, A. R., Sæbø, T. O., Hansen, R. E., and Pedersen, R. B. (2015). "The use of synthetic aperture sonar to survey seafloor massive sulfide deposits". In: *Journal of Ocean Technology* vol. 19, no. 1, pp. 36–53.

Dickey, F. R. J. (1981). *Velocity measuring correlation sonar*. United States Patent 4,244,026.

Fiorito, R., Madigosky, W., and Überall, H. (1979). "Resonance theory of acoustic waves interacting with an elastic plate". In: *The Journal of the Acoustical Society of America* vol. 66, no. 6, pp. 1857–1866.

Fossum, T. G., Sæbø, T. O., Langli, B., Callow, H. J., and Hansen, R. E. (2008). "HISAS 1030 - High resolution interferometric synthetic aperture sonar". In: *Proceedings of the Canadian Hydrographic Conference and National Surveyors Conference*. Victoria, BC, Canada, pp. 1–11.

Geilhufe, M., Connors, W. A., Synnes, S. A. V., Midtgaard, Ø., Sæbø, T. O., Hansen, R. E., and Dugelay, S. (2015). "Assessment of mine hunting performance evaluation parameters across multiple side-looking sonar systems and frequencies". In: *Proceedings of MTS/IEEE Oceans*. Washington DC, USA, pp. 1–9.

Geilhufe, M., Dugelay, S., Synnes, S. A. V., Sæbø, T. O., Midtgaard, Ø., and Hansen, R. E. (2014). "Comparative study of frequency dependency in high resolution sonar imagery from the MANEX'13 sea trials". In: *Proceedings of the Institute of Acoustics International Conference on Synthetic Aperture Sonar and Synthetic Aperture Radar (SAS/SAR)*. Lerici, Italy, pp. 191–200.

Gerry, M. J., Potter, L. C., Gupta, I. J., and Merwe, A. van der (1999). "A parametric model for synthetic aperture radar measurements". In: *IEEE Transactions on Antennas and Propagation* vol. 47, no. 7, pp. 1179–1188.

Ghiglia, D. C. and Pritt, M. D. (1998). *Two-Dimensional Phase Unwrapping: Theory, Algorithms, and Software*. John Wiley & Sons, INC, p. 512.

Grall, P., Kochanska, I., and Marszal, J. (2020). "Direction-of-arrival estimation methods in interferometric echo sounding". In: *Sensors* vol. 20, no. 12, pp. 1–17.

Griffiths, H. D., Rafik, T. A., Meng, Z., Cowan, C. F. N., Shafeeu, H., and Anthony, D. K. (1997). "Interferometric synthetic aperture sonar for high resolution 3-D mapping of the seabed". In: *IEE Proceedings - Radar, Sonar and Navigation* vol. 144, no. 2, pp. 96–103.

Groen, J., Hansen, R. E., Callow, H. J., Sabel, J. C., and Sæbø, T. O. (2009). "Shadow enhancement in synthetic aperture sonar using fixed focusing". In: *IEEE Journal of Oceanic Engineering* vol. 34, no. 3, pp. 269–284.

Groen, J., Schmaljohann, H., Leier, S., and Jans, W. (2015). "Synthetic aperture sonar fusion for images with dissimilar physical content due to differences in acoustic frequency". In: *Proceedings of the 3rd Underwater Acoustics Conference and Exhibition (UACE)*. Chania, Crete, Greece, pp. 121–128.

Hagen, P. E., Børhaug, E., and Midtgaard, Ø. (2010). "Pipeline inspection with interferometric SAS". In: *Sea Technology* vol. 51, no. 6, pp. 37–40.

Hagen, P. E., Callow, H., Reinertsen, E., and Sabo, T. O. (2018). "Cassandra: An integrated, scalable, SAS based system for acoustic imaging and bathymetry". In: *Proceedings of MTS/IEEE Oceans*. Charleston, SC, USA, pp. 1–6.

Hagen, P. E., Fossum, T. G., and Hansen, R. E. (2008). "HISAS 1030: The next generation mine hunting sonar for AUVs". In: *Proceedings of the Underwater Defence Technology (UDT) Pacific*. Sydney, Australia, pp. 1–8.

Hagen, P. E., Størkersen, N., Sten, G., Marthinsen, B., and Vestgård, K. (2005). "Military operations with HUGIN AUVs: Lessons learned and the way ahead". In: *Proceedings of Oceans Europe*. Brest, France, pp. 1–4.

Hansen, R. E., Sæbø, T. O., Callow, H. J., Hagen, P. E., and Hammerstad, E. (2005). "Synthetic aperture sonar processing for the HUGIN AUV". In: *Proceedings of Oceans Europe*. Brest, France, pp. 1–5.

Hansen, R. E. (2019). "Mapping the ocean floor in extreme resolution using interferometric synthetic aperture sonar". In: *Proceedings of the International Congress on Ultrasonics*. Bruges, Belgium, pp. 1–10.

Hansen, R. E. (2011). "Introduction to synthetic aperture sonar". In: *Proceedings of the Sonar Systems*. Ed. by Kolev, N. Z. IntechOpen, pp. 3–28.

Hansen, R. E. (2013). "Synthetic Aperture Sonar Technology Review". In: *Marine Technology Society Journal* vol. 47, no. 5, pp. 117–127.

Hansen, R. E., Callow, H. J., Sæbø, T. O., and Synnes, S. A. V. (2011). "Challenges in seafloor imaging and mapping with synthetic aperture sonar". In: *IEEE Transactions on Geoscience and Remote Sensing* vol. 49, no. 10, pp. 3677–3687.

Hansen, R. E., Lågstad, P., and Sæbø, T. O. (2019). *Search and monitoring of shipwreck and munitions dumpsites using HUGIN AUV with synthetic aperture sonar - technology study*. Tech. rep. FFI-rapport 19/00245. Norwegian DefenceResearch Establishment, pp. 1–33.

Hansen, R. E., Sæbø, T. O., Callow, H. J., and Hagen, P. E. (2007). *The SENSOTEK interferometric synthetic aperture sonar: Results from HUGIN AUV trials*. Tech. rep. FFI-rapport 2007/01597. Kjeller, Norway: Norwegian Defence Research Establishment (FFI), pp. 1–49.

Hansen, R. E., Sæbø, T. O., Callow, H. J., and Hagen, P. E. (2010). "Interferometric synthetic aperture sonar in pipeline inspection". In: *Proceedings of IEEE Oceans*. Sydney, Australia, pp. 1–10.

Hansen, R. E., Sæbø, T. O., Lorentzen, O. J., and Synnes, S. A. V. (2017). "Mapping unexploded ordnance (UXO) using interferometric synthetic aperture sonar". In: *Proceedings of the 4th Underwater Acoustics Conference and Exhibition (UACE)*. Skiathos, Greece, pp. 687–694.

Hayes, M. P. and Gough, P. T. (2009). "Synthetic Aperture Sonar: A Review of Current Status". In: *IEEE Journal of Oceanic Engineering* vol. 34, no. 3, pp. 207–224.

Hu, R., Min, R., and Pi, Y. (2017). "A Video-SAR imaging technique for aspect-dependent scattering in wide angle". In: *IEEE Sensors Journal* vol. 17, no. 12, pp. 3677–3688.

Hunter, A. J., Connors, W. A., and Dugelay, S. (2017). "An operational concept for correcting navigation drift during sonar surveys of the seafloor". In: *IEEE Journal of Oceanic Engineering* vol. 43, no. 4, pp. 913–926.

Hunter, A. J. and Dugelay, S. (2015). "Exploiting the coherence of seabed scattering for repeat-pass SAS micro-navigation". In: *Proceedings of the Institute of Acoustics Conference on Seabed and Sediment Acoustics*. Bath, UK, pp. 175–182.

Islas-Cital, A., Atkins, P. R., and Foo, K. Y. (2010). "Standard target calibration of broad-band active sonar systems in a laboratory tank". In: *Proceedings of IEEE Oceans*. Sydney, Australia, pp. 1–10.

Jackson, D. R. and Richardson, M. D. (2007). *High-Frequency Seafloor Acoustics*. New York, NY, USA: Springer Science+Business Media, LLC, p. 616.

Jakowatz, J. C. V., Wahl, D. E., Eichel, P. H., Ghiglia, D. C., and Thompson, P. A. (1996). *Spotlight-Mode Synthetic Aperture Radar: A Signal Processing Approach*. 1st ed. Springer, Boston, MA, USA, p. 429.

Jiang, H., Feng, G., Wang, T., and Bürgmann, R. (2017). "Toward full exploitation of coherent and incoherent information in Sentinel-1 TOPS data for retrieving surface displacement: Application to the 2016 Kumamoto (Japan) earthquake". In: *Geophysical Research Letters* vol. 44, no. 4, pp. 1758–1767.

Kapoor, R. and Nandhakumar, N. (1996). “Features for detecting obscured objects in ultra-wideband (UWB) SAR imagery using a phenomenological approach”. In: *Pattern Recognition* vol. 29, no. 11, pp. 1761–1774.

Kongsberg (2017). “The norwegian armed forces procures hugin autonomous underwater vehicles for nok 155 million”. In: *Kongsberg Maritime Press release*. URL: https://www.kongsberg.com/newsandmedia/news-archive/2017/the-norwegian-armed-forces-procures-hugin-autonomous-underwater-vehicles-for-nok/.

Kongsberg (2019). “Hugin Superior”. In: *Kongsberg Maritime Datasheet*. URL: https://www.kongsberg.com/globalassets/maritime/km-products/product-documents/hugin-superior.pdf.

Larsen, L. J., Wilby, A., and Stewart, C. (2010). “Deep ocean survey and search using synthetic aperture sonar”. In: *Proceedings of IEEE Oceans*. Sydney, Australia, pp. 8–11.

Libert, L., Derauw, D., D’Oreye, N., Barbier, C., and Orban, A. (2017). “Split-band interferometry-assisted phase unwrapping for the phase ambiguities correction”. In: *Remote Sensing* vol. 9, no. 9, pp. 1–17.

Lorentzen, O. J., Sæbø, T. O., Geilhufe, M., and Hansen, R. E. (2020). “Backscatter features for estimating synthetic aperture sonar bathymetry”. In: *Proceedings of IEEE/MTS Oceans*. virutal, pp. 1–2.

Love, A. W. (1985). “In memory of Carl A. Wiley”. In: *IEEE Antennas and Propagation Magazine*, no. June, pp. 17–18.

Lurton, X. (2002). *An Introduction to Underwater Acoustics: Principles and Applications*. 2nd ed. Chichester, UK: Springer Praxis Publishing, p. 716.

Madsen, S. N. and Zebker, H. A. (1992). “Automated absolute phase retrieval in across-track interferometry”. In: *Proceedings of the International Geoscience and Remote Sensing Symposium (IGARSS)*. Houston, Texas, USA, pp. 1–3.

Marston, T. M. and Kennedy, J. L. (2016). “Volumetric acoustic imaging via circular multipass aperture synthesis”. In: *IEEE Journal of Oceanic Engineering* vol. 41, no. 4, pp. 852–867.

Mastro, P., Serio, C., Masiello, G., and Pepe, A. (2020). “The multiple aperture SAR interferometry (MAI) technique for the detection of large ground displacement dynamics: An overview”. In: *Remote Sensing* vol. 12, pp. 1–48.

Neto, A. A., Rodrigues, G. P., and Alvarenga, I. D. (2017). “Seabed mapping with HISAS sonar for decommissioning projects”. In: *Sea Technology*, pp. 15–18.

Oliver, C. and Quegan, S. (1998). *Understanding Synthetic Aperture Radar Images*. 1st ed. Artech house, Inc., p. 512.

Pan, X., Chen, Q., Xu, W., Li, J., and Sun, F. (2016). “Shallow-water wideband low-frequency synthetic aperture sonar for an autonomous underwater vehicle”. In: *Ocean Engineering* vol. 118, pp. 117–129.

Pascazio, V. and Schirinzi, G. (2002). “Multifrequency InSAR height reconstruction through maximum likelihood estimation of local planes parameters”. In: *IEEE Transactions on Image Processing* vol. 11, no. 12, pp. 1478–1489.

Piper, J. E., Commander, K. W., Thorsos, E. I., and Williams, K. L. (2002). “Detection of buried targets using a synthetic aperture sonar”. In: *IEEE Journal of Oceanic Engineering* vol. 27, no. 3, pp. 495–504.

Plotnick, D. S. and Marston, T. M. (2018). "Utilization of Aspect Angle Information in Synthetic Aperture Images". In: *IEEE Transactions on Geoscience and Remote Sensing* vol. 56, no. 9, pp. 5424–5432.

Raven, R. S. (1981). *Electronic stabilization for displaced phase center systems*. United States Patent 4,244,036.

Rodriguez-Molares, A., Fatemi, A., Lovstakken, L., and Torp, H. (2017). "Specular Beamforming". In: *IEEE Transactions on Ultrasonics, Ferroelectrics, and Frequency Control* vol. 64, no. 9, pp. 1285–1297.

Rolt, K. D. (1991). "Ocean, Platform, and Signal Processing Effects on Synthetic Aperture Sonar Performance". Cand Scient. Massachusetts Institute of Technology, p. 233.

Scheiber, R. and Moreira, A. (2000). "Coregistration of interferometric SAR images using spectral diversity". In: *IEEE Transactions on Geoscience and Remote Sensing* vol. 38, no. 5 I, pp. 2179–2191.

Shea, D., Dawe, D., Dillon, J., and Chapman, S. (2014). "Real-time SAS processing for high-arctic AUV surveys". In: *Proceedings of the IEEE/OES Autonomous Underwater Vehicles (AUV)*. Oxford, MS, USA, pp. 1–5.

Skogen (ed.), E. (2005). "HUGIN – Utvikling av autonome undervannsfarkoster ved FFI". In: *Fra Forsvarets forskningsinstitutts historie*, pp. 1–24.

Sternlicht, D. D., Fernandez, J. E., Holtzapple, R., Kucik, D. P., Montgomery, T. C., and Loeffler, C. M. (2011). "Advanced sonar technologies for autonomous mine countermeasures". In: *Proceedings of MTS/IEEE Oceans*. Waikoloa, HI, USA, pp. 1–5.

Sternlicht, D. D., Hayes, M. P., and Hansen, R. E. (2018). "Historical development of seabed mapping synthetic aperture sonar". In: *Proceedings of the Institute of Acoustics 4th International Conference on Synthetic Aperture Sonar and Synthetic Aperture Radar (SAS/SAR)*. Lerici, Italy, pp. 1–10.

Sture, Ø., Ludvigsen, M., Scheide, M. S., and Thorsnes, T. (2018). "Recognition of cold-water corals in synthetic aperture sonar imagery". In: *Proceedings of the IEEE/OES Autonomous Underwater Vehicle Workshop (AUV)*. Porto, Portugal, pp. 1–6.

Synnes, S. A. V., Callow, H. J., Sæbø, T. O., and Hansen, R. E. (2010). "Multipass coherent processing on synthetic aperture sonar data". In: *Proceedings of the 10th European Conference on Underwater Acoustics (ECUA)*. Istanbul, Turkey, pp. 1–7.

Synnes, S. A. V. and Lorentzen, O. J. (2019). "Calibration target for estimation of frequency dependence in synthetic aperture sonar". In: *Proceedings of the 5th Underwater Acoustics Conference and Exhibition (UACE)*. Hersonissos, Crete, Greece, pp. 147–154.

Synnes, S. A. V., Sæbø, T. O., and Hansen, R. E. (2016). "Interferometry using phase slope estimation". In: *Proceedings of the 11th European Conference on Synthetic Aperture Radar (EUSAR)*. Hamburg, Germany, pp. 1–4.

Synnes, S. A., Hansen, R. E., and Sæbø, T. O. (2009). "Assessment of shallow water performance using interferometric sonar coherence". In: *Proceedings of the 3rd Underwater Acoustic Measurements (UAM)*. Nafplion, Greece, pp. 1391–1396.

Synnes, S. A. V. and Hansen, R. E. (2013). "Ultra wideband SAS imaging". In: *Proceedings of the 1st Underwater Acoustics Conference and Exhibition (UACE)*. Corfu, Crete, Greece, pp. 111–118.

Synnes, S. A. V. and Hansen, R. E. (2015). "Aspect-dependent scattering in widebeam synthetic aperture sonar". In: *Proceedings of the 3rd Underwater Acoustics Conference and Exhibition (UACE)*. Chania, Crete, Greece, pp. 129–136.

Synnes, S. A. V., Hansen, R. E., and Sæbø, T. O. (2021). "Spatial coherence of speckle for repeat-pass synthetic aperture sonar micronavigation". In: *IEEE Journal of Oceanic Engineering (Eary Access)*, pp. 1–16.

Synnes, S. A. V., Hunter, A. J., Hansen, R. E., Sæbø, T. O., Callow, H. J., Vossen, R. van, and Austeng, A. (2017). "Wideband synthetic aperture sonar backprojection with maximization of wave number domain support". In: *IEEE Journal of Oceanic Engineering* vol. 42, no. 4, pp. 880–891.

Sæbø, T. O., Hansen, R. E., and Hanssen, A. (2007). "Relative height estimation by cross-correlating ground-range synthetic aperture sonar images". In: *IEEE Journal of Oceanic Engineering* vol. 32, no. 4, pp. 971–982.

Sæbø, T. O., Synnes, S. A. V., and Hansen, R. E. (2012). "Wideband interferometry in synthetic aperture sonars". In: *Proceedings of the 9th European Conference on Synthetic Aperture Radar (EUSAR)*. Nürnberg, Germany, pp. 1–4.

Sæbø, T. O. (2010). "Seafloor Depth Estimation by means of Interferometric Synthetic Aperture Sonar". PhD thesis. University of Tromsø, Norway, p. 202.

Sæbø, T. O., Synnes, S. A. V., and Hansen, R. E. (2013). "Wideband interferometry in synthetic aperture sonar". In: *IEEE Transactions on Geoscience and Remote Sensing* vol. 51, no. 8, pp. 4450–4459.

Veneziani, N., Bovenga, F., and Refice, A. (2003). "A wide-band approach to the absolute phase retrieval in SAR interferometry". In: *Multidimensional Systems and Signal Processing* vol. 14, pp. 183–205.

Walsh, G. M. (1969). *Acoustic mapping apparatus*. United States Patent 3,484,737.

Wang, L., Bellettini, A., Hollett, R., Tesei, A., Pinto, M., Chapman, S., and Gade, K. (2001). "InSAS'00: Interferometric SAS and INS aided SAS imaging". In: *Proceedings of MTS/IEEE Oceans*. Honolulu, HI, USA, pp. 179–187.

Wang, Z., Yang, Y., Ding, Z., Lin, S., Zhang, T., and Lv, Z. (2017). "A high-accuracy interferometric SAR images registration strategy combined with cross correlation and spectral diversity". In: *Proceedings of the International Conference on Radar Systems (Radar)*. Belfast, UK, pp. 1–6.

Wiley, C. A. (1965). *Pulsed Doppler radar methods and apparatus methods*. United States Patent 3,196,436.

Williams, K. L., Kargl, S. G., Thorsos, E. I., Burnett, D. S., Lopes, J. L., Zampolli, M., and Marston, P. L. (2010). "Acoustic scattering from a solid aluminum cylinder in contact with a sand sediment: Measurements, modeling, and interpretation". In: *The Journal of the Acoustical Society of America* vol. 127, no. 6, pp. 3356–3371.

Waage, T. E. (2014). *Syv krigsskip til Vågen: Nato-flåte på besøk*.

Xenaki, A. and Pailhas, Y. (2019). “Compressive synthetic aperture sonar imaging with distributed optimization”. In: *The Journal of the Acoustical Society of America* vol. 146, no. 3, pp. 1839–1850.

Xu, W., Chang, E. C., Kwoh, L. K., Lim, H., and Heng, W. C. A. (1994). “Phase-unwrapping of SAR interferogram with multi-frequency or multi-baseline”. In: *Proceedings of the IEEE International Geoscience and Remote Sensing Symposium (IGARSS)*. Pasadena, CA, USA, pp. 730–732.

Yu, H., Lan, Y., Yuan, Z., Xu, J., and Lee, H. (2019). “Phase unwrapping in InSAR: A review”. In: *IEEE Geoscience and Remote Sensing Magazine* vol. 7, no. 1, pp. 40–58.

Ødegård, Ø., Hansen, R. E., Singh, H., and Maarleveld, T. J. (2018). “Archaeological use of synthetic aperture sonar on deepwater wreck sites in Skagerrak”. In: *Journal of Archaeological Science* vol. 89, pp. 1–13.

Papers

Paper I

Wideband Interferometry in Synthetic Aperture Sonar

Torstein Olsmo Sæbø, Stig Asle Vaksvik Synnes, Roy Edgar Hansen

 IEEE Transactions on Geoscience and Remote Sensing, August 2013, volume 51, issue 8, pp. 4450–4459.
DOI: 10.1109/TGRS.2013.2244900.

Abstract

Synthetic aperture sonar (SAS) interferometry can provide very high resolution images and topographic maps of the seafloor over large swaths. Processing of interferometric data to retrieve reliable depth estimates of the seafloor is, however, non-trivial. Traditional narrowband interferometry processing relies on advanced phase unwrapping techniques, constraints, and prior knowledge to resolve phase ambiguities. These methods all have dependence throughout the dataset, e.g. a small error in the assumption may cause a global error in the final phase estimate. For wideband systems there are alternative techniques to estimate the absolute (or ambiguity-free) phase difference directly. We consider four different wideband interferometry techniques for direct phase difference estimation: complex cross correlation, split-spectrum algorithm, and the multi-chromatic approach. In addition, we develop a weighted split-spectrum algorithm, where the weights minimizes the variance in the absolute phase estimate. We benchmark these techniques on simulated data and demonstrate the techniques on real data from the HISAS wideband interferometric SAS on a HUGIN autonomous underwater vehicle. We have found the following: The cross correlation technique always outperforms the other techniques in misregistrated areas caused by severe topographic changes. The split spectrum techniques are substantially faster than the cross correlation technique. The multi-chromatic approach has similar performance as the multiband split spectrum technique for the same choice of bands. We demonstrate that all the wideband interferometry techniques outperform a

All authors are with the Norwegian Defence Research Establishment (FFI), Norway. Synnes is also pursuing a Ph.D. at the University of Oslo, Norway, where Hansen is adjunct associated professor.

standard Goldstein's Branch cut phase unwrapping algorithm on real data from a complicated scene containing an elevated target and severe layover.

I.1 Introduction

Interferometry refers to a family of techniques where interference phenomena between waves are used to measure e.g. the shift between two dataset. In synthetic aperture radar (SAR) interferometry means measuring the shift between SAR images. If the sensor positions are separated with a vertical baseline, the across-track shift can be used to estimate the topography.

Synthetic aperture sonar (SAS) technology (similar to SAR) has matured substantially the last few years (Hansen, 2011; Hayes et al., 2009). As for radar, interferometry has been considered for SAS (Bonifant Jr et al., 2000; Griffiths et al., 1997; Sæbø, 2010), with specific differences between SAS and SAR (Griffiths, 1997; Sæbø et al., 2010a).

The Norwegian Defence Research Establishment (FFI) and Kongsberg Maritime have a long term collaboration to develop SAS technology. Figure I.1 shows a HUGIN autonomous underwater vehicle (AUV) onboard FFI's research vessel H. U. Sverdrup II. The vehicle is equipped with a HISAS 1030 wideband interferometric SAS with two receiver arrays for single-pass interferometry and 30% relative bandwidth (Fossum et al., 2008; Hagen et al., 2008).

Traditional SAR interferometry techniques (Bamler et al., 1998; Hanssen, 2001; Rosen et al., 2000) rely on coregistered images and advanced phase unwrapping techniques to produce Digital Elevation Models (DEM). For wideband systems, the absolute (or ambiguity-free) phase difference between two images can be estimated directly (Bamler et al., 2004; Pascazio et al., 2002; Veneziani et al., 2003). In this paper we consider four different techniques: The *complex cross correlation* (CCC) technique used in standard time delay estimation (Madsen, 1995; Sæbø et al., 2007). The *split-spectrum* algorithm (SSA), based on splitting the signal into two frequency subbands and generating an differential interferogram (similar to Delta-k) (Bamler et al., 2005; Madsen et al., 1992). The *multi-chromatic approach* (MCA), based on generating multiple interferograms in different frequency bands. The interferograms will wrap at different intervals, and the wraps that minimizes the subband differences are chosen (Pascazio et al., 2001; Veneziani et al., 2000). We have also developed a *weighted multiband split-spectrum* algorithm (WSSA), where multiple bands are formed, and interferograms at all difference frequencies are constructed. The weights are chosen based on the signal to noise ratio and the frequency separations. We study the theoretical performance of these techniques, evaluate their performance on a simulated scenario, and finally apply the methods on real data from the HISAS interferometric SAS.

In section I.2 we review the basic principle of depth estimation by interferometry,

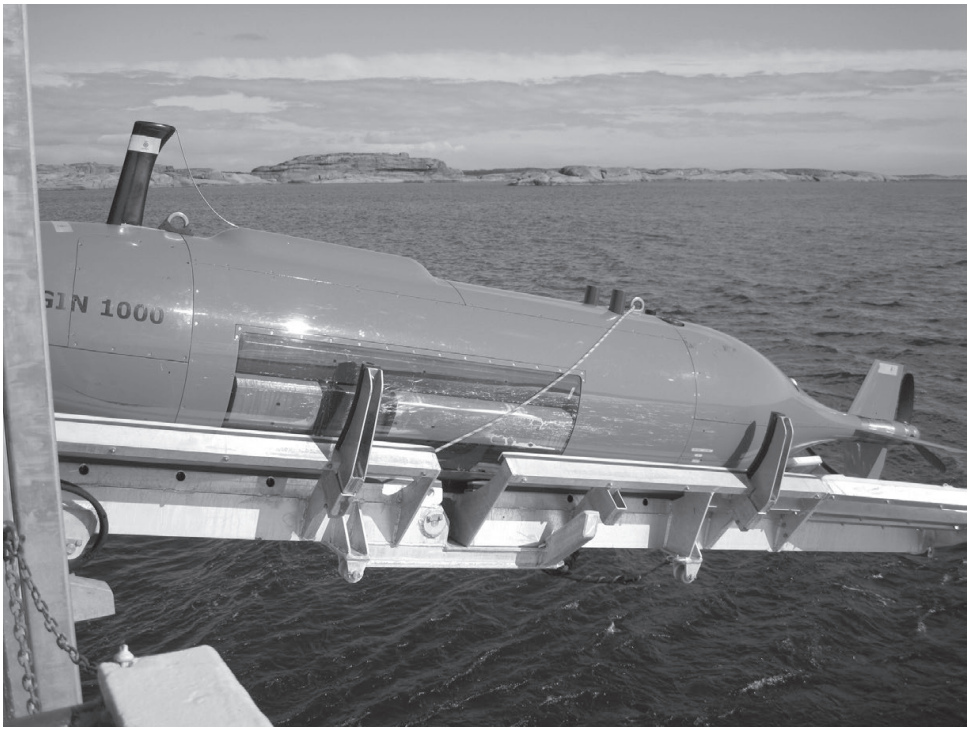

Figure I.1: The HUGIN autonomous underwater vehicle equipped with the HISAS wideband interferometric synthetic aperture sonar.

in section I.3 we describe the different techniques for absolute phase difference estimation. In I.4 we describe the processing flow for wideband interferometry, and in I.5 we assess the performance of the different techniques on simulated data. In I.6 we show wideband interferometry results on real data collected by HUGIN AUV, and in I.7 we conclude our work.

I.2 Depth Estimation

We construct a master SAS image $s_m(t, x)$ and slave SAS image $s_s(t, x)$ from two vertically displaced arrays, where t is the two-way travel time and x is the position along the synthetic aperture. By estimating the time delay, $t_d(t)$, between corresponding image features, we obtain a depth-estimate relative to the sonar coordinate system (Hanssen, 2001), (Jakowatz et al., 1996, chapter 5)

$$z(t) = r\frac{c}{D}t_d(t). \tag{I.1}$$

Here $r = ct/2$ is the one way range, c is the sound speed and D the interferometric baseline (see Figure I.2). The depth estimation is thus reduced to a time delay estimation problem.

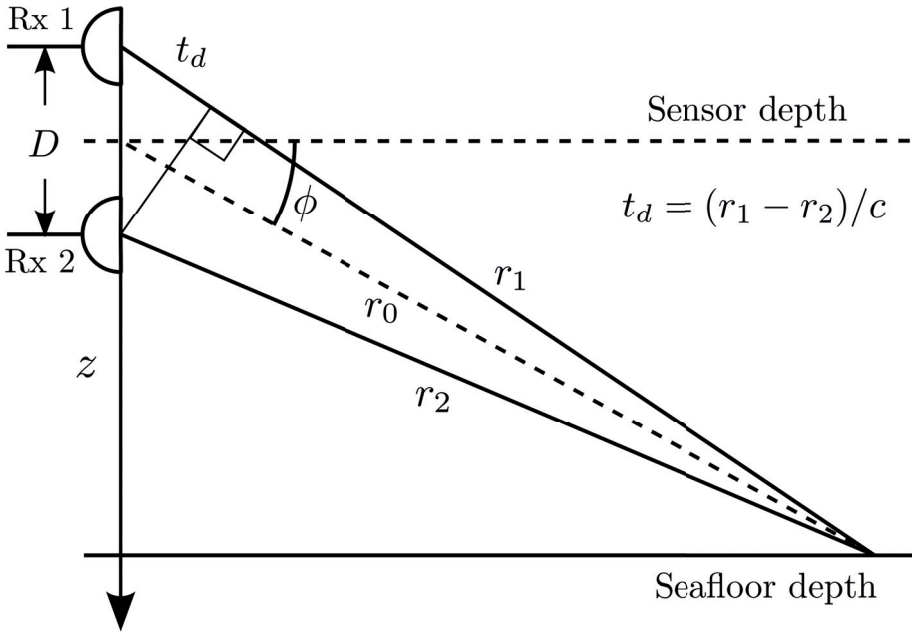

Figure I.2: Geometry of seafloor depth estimation.

I.2.1 Coarse co-registration

In order to extract the phase difference (or the corresponding time delay) between the master and slave SAS images, the images must be co-registered (Fornaro et al., 1995; Jakowatz et al., 1996). The success of the co-registration can be estimated from the coherence between the two images. Coherence is here defined as the amplitude of the complex degree of coherence (Hanssen, 2001, chapter 4.3)

$$\gamma(\tau) = \frac{\langle s_m s_s^*(t_d - \tau)\rangle}{\left[\langle |s_m|^2\rangle \langle |s_s|^2\rangle\right]^{1/2}} \tag{I.2}$$

evaluated at zero-lag, $\tau = 0$. The coherence has the property $0 \leq |\gamma(\tau)| \leq 1$. For simplicity, we have omitted the time- and position arguments.

Registration within a fraction of a resolution cell is required for accurate phase estimation modulo 2π. For absolute (ambiguity free) phase difference estimation, registration to within the wrapping interval is also required. The image resolution along the (two-way) time axis is $1/B$, and the wrapping interval of the phase difference is $1/f_c$, where B is the full bandwidth and f_c the center frequency. This means that, in general, co-registration to within the wrapping interval is only achievable for ultra-wideband systems with high signal-to-noise ratio (SNR). The co-registration is usually performed through a warping function estimated from a set of control points (Hong et al., 2006), or through an *a priori* knowledge of the seafloor depth (Sæbø, 2010). Both the warping function and the *a priori* seafloor depth are typically of too low order to capture rapid depth changes, which occur on complicated objects. This means that in practice, there will

always be some occurrence of wrap ambiguities in the phase differences.

I.2.2 Interferogram estimation

For each resolution cell in the co-registered SAS images, the complex interferogram γ around the center frequency f_c is computed through

$$\gamma(f_c) = s_m(f_c)s_s^*(f_c). \tag{I.3}$$

In practice a sliding maximum likelihood phase estimation filter is used to reduce the phase noise in the complex interferogram at the cost of reduced spatial resolution (Ghiglia et al., 1998, chapter 3.2), (Hanssen, 2001, chapter 4.3). The interferometric phase difference, $\psi_w(f_c) = \arg\{\gamma(f_c)\}$, is a function of the interferometric time delay. However, the phase difference is available only modulo 2π, with the absolute phase difference between the two images, $\psi_a(f_c)$, defined as

$$\psi_a(f_c) = 2\pi f_c t_d. \tag{I.4}$$

The time delay is thus related to the absolute phase difference and the interferometric (wrapped) phase difference through

$$t_d = \frac{\psi_a(f_c)}{2\pi f_c} = \frac{\psi_w(f_c)}{2\pi f_c} + \frac{k(f_c)}{f_c}, \tag{I.5}$$

where $k(f_c)$ is the number of 2π-wraps at center frequency.

I.2.3 Phase unwrapping

A common method used to resolve phase ambiguities in the interferogram is a 2D phase unwrapper (Ghiglia et al., 1998). A phase unwrapper assumes that the phase differences between neighboring pixels are less than π. Phase unwrappers therefore add additional information and may outperform absolute phase difference estimators. However, when using 2D phase unwrappers, any small error in the assumption may cause an global error in the final depth estimate, since all pixels are dependent. In this paper we have chosen to use a standard Goldstein‘s Branch cut algorithm, as described in (Ghiglia et al., 1998, chapter 4.2), as a benchmark method. There do exist more advanced phase unwrappers, but since our effort in this paper is concentrated in estimating the absolute phase differences directly more advanced phase unwrappers are outside the scope of this article.

I.3 Absolute Phase Difference Estimators

The challenge of absolute phase difference estimation is to obtain the correct wrap. Different absolute phase estimators will have different performance, but a non-adaptive method cannot perform better than the maximum likelihood

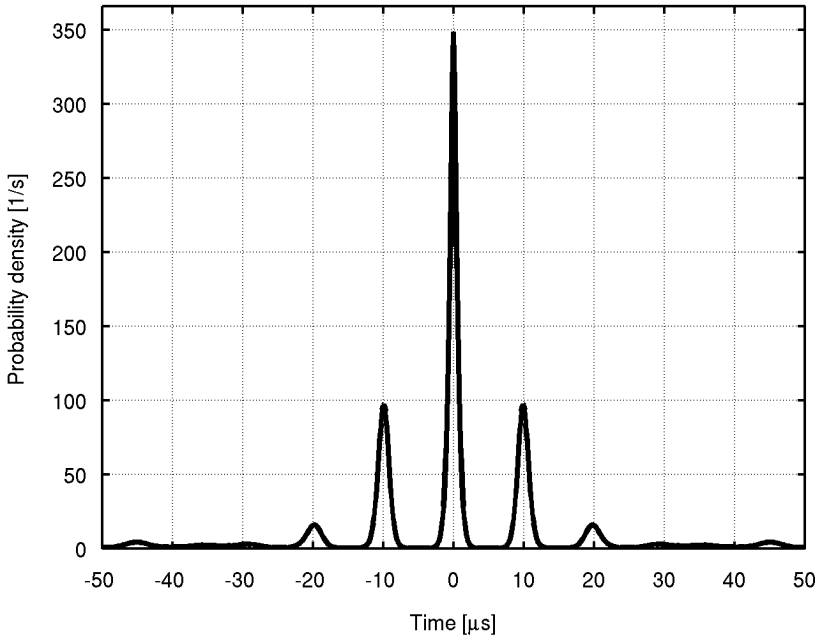

Figure I.3: Approximated probability density function (PDF) for estimation of delay τ with the maximum likelihood estimator. The example is for 0 dB SNR, 100 kHz center frequency, 30% relative bandwidth and 0.5 ms integration time.

estimator (MLE). The performance of such an estimator has been studied in detail (Weinstein et al., 1984; Weiss et al., 1983). The probability of estimating a delay offset τ cannot generally be expressed in a closed analytic form, but a closely approximated expression is given in (Weinstein et al., 1984, eq 4-8), assuming a large number of independent samples. The related probability density function (PDF), $p(\tau)$, is a function of the SNR, frequency interval, the length of the time series (i.e. the number of independent samples) and the sensor separation in wavelengths. In Figure I.3 we show $p(\tau)$ for an example case with 0 dB SNR, 100 kHz center frequency, 30% relative bandwidth and 0.5 ms integration time, limited to an interval of ± 5 wraps. We observe that the function describes the lower bound regarding both the probability for incorrect wrap and the accuracy within each wrap.

The probability of obtaining the correct wrap is found by integrating $p(\tau)$ over the interval $[-1/(2f_c), 1/(2f_c)]$. Examples on the maximum theoretical probability of obtaining the correct wrap as a function of SNR and relative bandwidth is presented in Figure I.4. The signal frequency is 100 kHz, and the length of the time series is 0.5 ms, corresponding to 50 independent samples for 30% relative bandwidth. The absolute phase difference error is limited within ± 5 wraps, hence the lower value is 0.1. We see that a wideband system with e.g. 30% relative bandwidth has substantially better probability to estimate correct wrap than a narrowband system. This is an important finding, and suggests

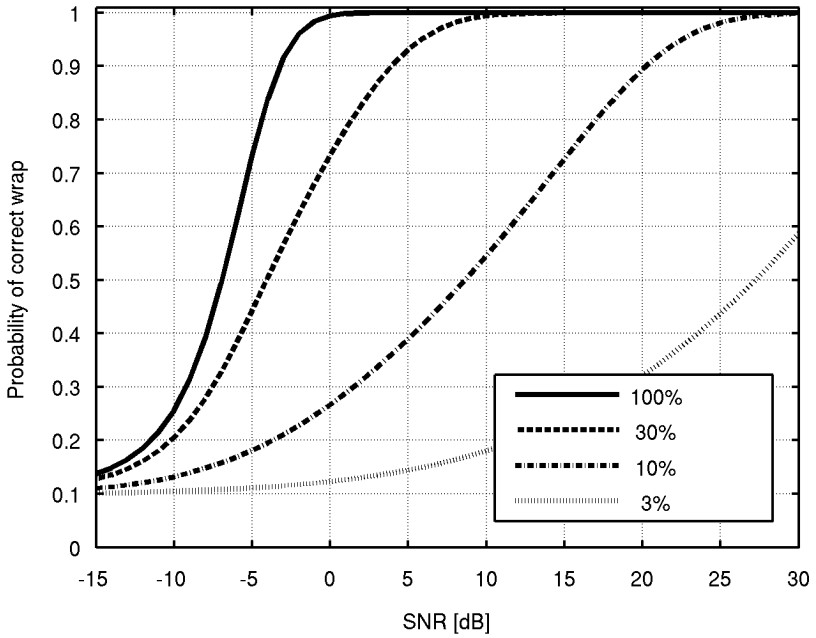

Figure I.4: Theoretical probability of correct wrap as a function of SNR and relative bandwidth. The length of the series is 0.5 ms, corresponding to 50 independent samples for 30% relative bandwidth, and the search is limited within ±5 wraps.

that absolute phase techniques can potentially achieve good performance on wideband systems.

In the rest of this section, we describe four different techniques for absolute phase difference estimation.

I.3.1 Complex Cross Correlation (CCC)

Peak detection in the complex cross correlation (CCC) of the two sequences is the Maximum Likelihood Estimator for differential shift estimation of partially correlated sequences (Jakowatz et al., 1996, chapter 5.4), (Seymour et al., 1994). The MLE has the asymptotic properties of being unbiased and achieving the Cramér-Rao lower bound (CRLB) (Kay, 1993, chapter 7). The master and slave images must be oversampled before the fine-level (sub-resolution) cross correlation to avoid aliasing (Hanssen, 2001, chapter 2.5.3), and the step interval for the CCC evaluation should not exceed the ambiguity interval. Then the peak magnitude is detected, and can be used to determine the absolute phase (and thereby the correct wrap interval)

$$\psi_a(f_c) = 2\pi f_c \arg\max_{\tau} |\gamma(\tau)| \tag{I.6}$$

The ability to estimate correct wrap is dependent on the relative bandwidth and the signal to noise ratio (Weinstein et al., 1984), (Sæbø et al., 2007). For systems with limited bandwidth, CCC is less suited as an absolute phase difference estimator. In the limit of ultra-wideband systems, the phase becomes ambiguity free (Ulander et al., 1998), and only phase noise within the wrap interval affects the accuracy of the depth estimation. CCC is computational heavy compared to the other techniques in this paper. It starts from the coarse co-registrated images and performs fine-level (sub-resolution) co-registration over the entire image. CCC also allows for searching outside the initial pixel correlations, and therefore is a more robust method.

In the case of non-white noise and/or non-white signal, standard CCC may not be optimum, and techniques like the generalized cross correlation (GCC) (Carter, 1987; Knapp et al., 1976) can potentially improve the performance.

I.3.2 Split-Spectrum Algorithm (SSA)

The split-spectrum algorithm (SSA) splits the full bandwidth B into two non-overlapping subbands of bandwidth b. Then the interferogram from each subband is formed, and thereafter combined into a differential interferogram (Bamler et al., 2005). By expressing both bands through equation (I.5), we observe that this corresponds to an interferogram at the differential frequency

$$\psi_a(\Delta f) = 2\pi(f_2 - f_1)t_d = \psi_a(f_2) - \psi_a(f_1) \tag{I.7}$$

where f_1 and f_2 are the frequencies of each subband and $\Delta f = f_2 - f_1$. The advantage is that this interferogram wraps with the larger period $1/\Delta f$. The costs are larger resolution cells by a factor B/b, and increased variance of the time delay. With SSA, the absolute phase at f_c becomes

$$\psi_a(f_c) = \frac{f_c}{\Delta f}\psi_a(\Delta f). \tag{I.8}$$

By inserting the variance for the time delay estimate of each subband $\sigma^2_{f_1}$ and $\sigma^2_{f_2}$ we find the corresponding variance on the estimate using the delta frequency $\sigma^2_{\Delta f}$ to be

$$\sigma^2_{\Delta f} = \frac{f_2\sigma^2_{f_2} + f_1\sigma^2_{f_1}}{f_2 - f_1}. \tag{I.9}$$

The Split-Spectrum Algorithm described in the literature uses only two subbands. Within this restriction it has been shown that the smallest variance is achieved by dividing the total bandwidth B into three equal parts and using the upper and lower bands (Bamler et al., 2005). The split spectrum technique uses the same principle as in ΔK, first exploited by (Hagfors, 1961) in radar applications.

I.3.3 Multi-Chromatic Approach (MCA)

An alternative method that can be used on either two or multiple frequency bands is the Multi-Chromatic Approach (MCA) (Veneziani et al., 2003; Veneziani et al., 2006). MCA, as with SSA, takes advantage of that the absolute phase difference is proportional to the frequency. The original master and slave images are divided into two or multiple bands at different center frequencies $f_n, n = 1, 2, 3, \ldots, N$ with reduced bandwidth $b < B$. Each subband can overlap in frequency domain $b > B/N$ (Bovenga et al., 2009; Bovenga et al., 2011). Interferograms at different center frequencies will wrap at different intervals. As a result, the time delay t_d can be estimated by comparing the wrap combinations for the different interferograms.

Functionally, the estimator can be described as follows. We construct a series of vectors

$$\mathbf{k} = [k_1, k_2, \ldots, k_N], \quad k_n = 0, \pm 1, \pm 2, \ldots \tag{I.10}$$

containing candidate solutions within certain limits given by geometry and baseline. We then form a cost function which is the variance of the absolute phase estimate for a given candidate $\mathbf{k}$

$$J(\mathbf{k}) = \frac{1}{N} \sum_{n=1}^{N} \left\{ \frac{f_c}{f_n} \left(\psi_w(f_n) + 2\pi k_n \right) - \psi_{avg}(f_c, \mathbf{k}) \right\}^2 \tag{I.11}$$

where

$$\psi_{avg}(f_c, \mathbf{k}) = \frac{1}{N} \sum_{n=1}^{N} \frac{f_c}{f_n} \left\{ \psi_w(f_n) + 2\pi k_n \right\} \tag{I.12}$$

is the average absolute phase for the given selection of $\mathbf{k}$. We then minimize the cost function

$$\mathbf{k}_{min} = \arg\min_{\mathbf{k}} J(\mathbf{k}) \tag{I.13}$$

to determine the optimal choice of wraps per subband $\mathbf{k}_{min}$. The absolute phase difference is then estimated by averaging over all subbands

$$\psi_a(f_c) = \frac{1}{N} \sum_{n=1}^{N} \frac{f_c}{f_n} \left\{ \psi_w(f_n) + 2\pi k_{n,min} \right\}. \tag{I.14}$$

In the general case of different variance in different bands, the above least squares method should be modified to incorporate weights of $1/\sigma^2$ (Veneziani et al., 2000; Veneziani et al., 2003). The multifrequency interferometry method (Pascazio et al., 2001; Pascazio et al., 2002) give a result similar to MCA, but it approaches the problem thorough the PDF of the absolute phase estimate rather than through the error function of the absolute phase estimate.

I.3.4 Weighted Multiband Split-Spectrum Algorithm (WSSA)

In order to use all the signal information, we suggest an extension of SSA to multiple bands. As with MCA, we divide the signal bandwidth into N bands. We then form all the difference frequencies $\Delta f_{nm} = f_n - f_m$, using the description for SSA, where equation (I.9) is valid for non-overlapping subbands. There are $K = N(N-1)/2$ differences (Johnson et al., 1993, chapter 3.3). We estimate the absolute phase at f_c, $\psi_a(f_c)$, from the absolute phase of each band pair, $\psi_a(\Delta f_{nm})$, and average all to form a final estimate of the absolute phase difference

$$\psi_a(f_c) = \frac{1}{w_{tot}} \sum_{n=1}^{N} \sum_{\substack{m=1 \\ m \neq n}}^{n} w_{nm} \frac{f_c}{\Delta f_{nm}} \psi_a(\Delta f_{nm}). \tag{I.15}$$

w_{nm} is a weight that can be chosen, and w_{tot} is a normalization factor. By choosing $w_{nm} = 1/\sigma^2_{\Delta f_{nm}}$ from (I.9) and

$$w_{tot} = \frac{1}{\sigma^2_{\Delta f_{tot}}}, \quad \sigma^2_{\Delta f_{tot}} = \sum_{n=1}^{N} \sum_{\substack{m=1 \\ m \neq n}}^{n} \sigma^2_{\Delta f_{nm}} \tag{I.16}$$

we get a *weigthed multiband SSA* estimate, where the weights of the individual band-pairs are the inverse of the variance $1/\sigma^2_{\Delta f_{nm}}$. By using the actual estimates for $\sigma^2_{f_i}$, this is an adaptive filter that minimizes the variance of the combined absolute phase difference estimate. Such adaption to the data will potentially improve the performance compared to deterministic filters when the subband variance changes over the bands. A similar type of weighting was suggested for MCA in (Veneziani et al., 2000; Veneziani et al., 2003). By assuming the same variance for each subband, we get a non-adaptive multiband method with the (relative) weights $w_{nm} = (f_2 - f_1)/(f_2 + f_1)$.

I.3.5 Summary of Methods

CCC is maximum likelihood and should theoretically achieve a Fisher efficiency of one (the ratio of the CRLB to the variance of the estimator). According to (Brcic et al., 2009) the Fisher efficiency for SSA is 0.75 for two densely spaced subbands of $b = B/2$, and 0.89 by using two maximally separated subbands of $b = B/3$. An extension of the method to four bands should give Fisher efficiencies of 0.93 and 0.96 respectively. Even so, our WSSA is an adaptive minimum least squares method that could outperform maximum likelihood estimators in the case of non-white noise.

Traditional narrowband SAR/SAS interferometry requires a 2D phase unwrapping stage (see Section I.2.3), where prior knowledge or specific properties of the data is assumed (smooth surfaces or such) (Nico et al., 2000). Thus for narrowband systems, methods like Conditional Mean Estimate and Maximum A Posteriori (MAP) can obtain substantially higher performance than the MLE (Loffeld et al., 2008), when the prior knowledge is correct.

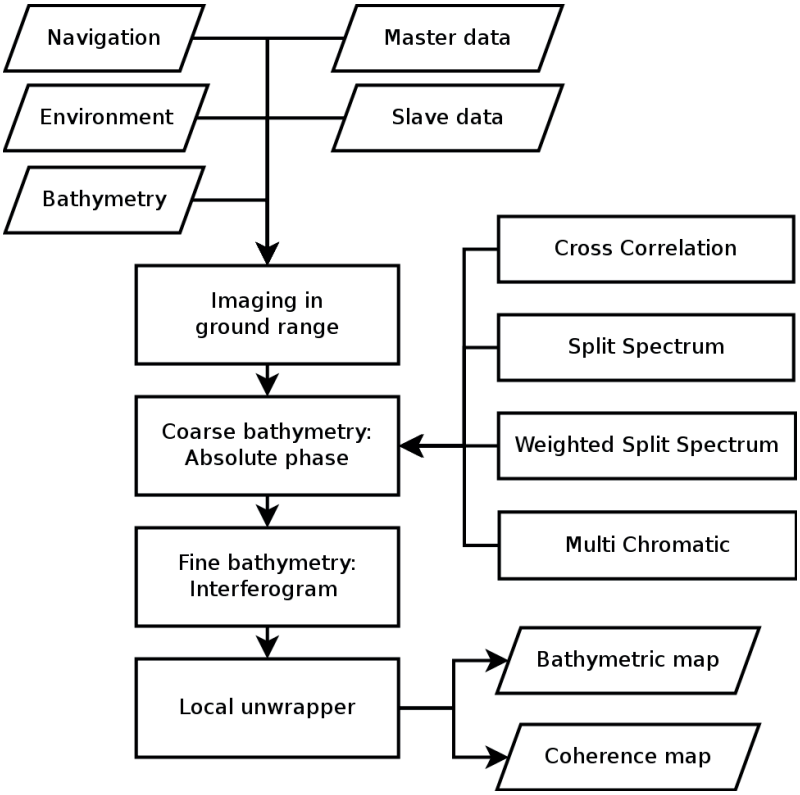

Figure I.5: Full wideband interferometry processing scheme including absolute phase difference estimation.

The key properties of the described methods are:

1. CCC does a local coregistration, and always performs better than subband methods on misregistrated images.

2. CCC is substantially slower than the other methods.

3. MCA and multiband SSA have similar performance for the same choice of bands.

4. Multiband SSA is simpler to implement and is faster than MCA for the same choice of bands.

5. Multiband WSSA is always better than multiband SSA on the same choice of bands.

6. Multiband SSA and MCA approaches the performance of CCC for large number of bands.

I.4 Processing Flow

Figure I.5 shows the basic processing flow for wideband SAS interferometry processing including the absolute phase estimation methods described in the previous section. In this section, we describe each of the components in this processing flow.

We first produce a master and a slave image which are coarsely coregistered by rendering the images on an *a priori* seafloor depth. The coarse registration is based on real aperture (or sidescan) seafloor depth estimation from the same data (Hansen et al., 2011; Sæbø et al., 2010b). The images are constructed using the backprojection algorithm, and are gridded in ground range. We pre-flatten the spectrum of the images as suggested in (Bovenga et al., 2009).

Then one of the absolute phase difference estimators are run to resolve the phase ambiguities of the full bandwidth interferogram. All of the methods use a maximum likelihood estimator to estimate the phase differences. In this article we have chosen to use a 9×9 pixels filter window. Since the images are slightly oversampled in $2 \times 2\,\mathrm{cm}$, the effective number of independent pixels in the phase difference estimators is approximately 50.

All the subband methods have increased variance compared to the variance of the phase difference on the full band interferogram (for CCC, the full bandwidth is incorporated in the estimation). We therefore only use the absolute phase difference estimates to determine the correct wrap

$$k(f_c) = \left\lfloor \frac{1}{2\pi} \left\{ \psi_a(f_c) - \psi_w(f_c) \right\} \right\rceil \tag{I.17}$$

where $\lfloor \rceil$ is the `round`-operator. In order to obtain the correct $k(f_c)$, each subband must be selected wide enough to yield a time delay estimate variance smaller than the wrap interval $1/f_c$.

In a standard interferogram, the phase differences are typically wrapped from smooth, continuous absolute phase differences. This may not be true for very complicated scenes. Thus large regions in the interferogram will have the same phase wraps, and a 2D phase unwrapper simply tries to connect the regions. After we have run one of the absolute phase difference estimators, the interferogram are in general unwrapped. However, there will remain small areas (with a size typical less then the phase difference estimation window) with incorrect wrap randomly distributed throughout the scene. As we saw in Figure I.4, the number of wrap errors is strongly dependent on the SNR. To remove these residual errors we have implemented a *local* unwrapper. The local unwrapper estimates the median value inside a small neighboring region and unwraps the phase difference to this value. This method removes the wrap errors provided that the number of incorrect wraps are significantly less than the number of correct wraps. The advantage with such a local method is that a small error in the method will

not affect large regions in the unwrapped phase difference. Note that since the wrap errors are randomly located after we have run an absolute phase difference estimators, the data do now not fulfill the assumptions of most phase unwrappers. This means that running for example Goldsteins Branch algorithm on top of an absolute phase difference estimators will provide large errors.

I.5 Performance Assessment on Simulated Data

To test the performance we have simulated a scene consisting of a flat seafloor (simple) with a wreck (difficult). We have focused the SAS images onto a ground-plane with a 1 m depth error relative to the true depth of the flat part of the seafloor (which is realistic in real scenarios).

The simulated wreck has a height which is up to 4 m off the *a priori* depth. The simulated sonar is a HISAS 1030 sonar with 30 kHz bandwidth around 100 kHz center frequency, and a 30 cm vertical baseline (20 λ). The wreck is at 10 meters water depth and the ground range in the simulation extends from 41 to 59 meters. The front of the wreck causes significant layover which causes problems for all of the considered methods. Recent work (Reigber et al., 2000; Zhu et al., 2012) show promising results in reducing the effect of layover via the SAR tomography technique, but such methods are outside the scope of this paper.

In our implementation, we have found that MCA and multiband SSA have similar performance for the same choice of bands. We therefore only consider multiband SSA, WSSA and CCC here.

We have evaluated two performance measures:

I.5.1 Robustness

We study the robustness of the techniques by investigating how often the methods successfully manage to estimate the correct wrap. In this case we have considered the flat seafloor region of our simulation. The findings are: WSSA and SSA have similar performance on two subbands; WSSA is better than SSA for three or more subbands; more subbands are better; the number of subbands should be lower than the number of across-track pixels in the phase difference estimation window; when using two subbands these should be sparse; when using five subbands these should be densely spaced; CCC is better than WSSA and SSA up to three subbands, but WSSA and SSA with five subbands are better than CCC (see discussion below). In Figure I.6 we show the performance of the most relevant methods as a function of estimated SNR. Notice that the results in Figure I.6 only applies to this specific scenario and should only be used to compare the relative performance between the methods.

WSSA is an adaptive method that can outperform CCC. However, we found that multiband SSA also outperformed CCC, while we expected CCC to have the

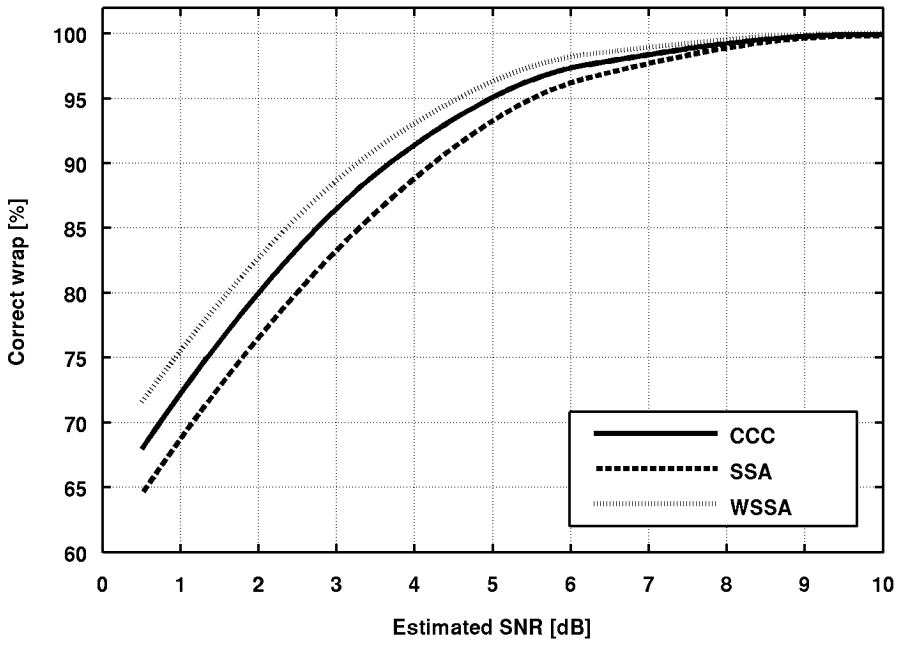

Figure I.6: Probability of correct wrap as a function of SNR for the different methods . For WSSA we have used five dense subbands and for SSA we have used two sparse subbands.

highest score of the none-adaptive methods. This could be a consequence of CCC being a higher order model. CCC estimates shift in addition to phase-difference, in contradiction to WSSA and SSA which assumes zero-lag. In this simulation the shift is only a small fraction of a resolution cell, so zero-lag is the correct answer. This mean that WSSA and SSA have *a priori* knowledge which CCC does not have.

I.5.2 Accuracy

We study the accuracy of the techniques by investigating the actual variance on the final depth estimates. CCC estimates a shift and perform better than the other methods if there is significant misregistration between the images. If we assume that the wrap is correct, both WSSA and SSA have the same accuracy as regular phase-differencing. This is because we only use WSSA and SSA to estimate the wraps and then we apply full bandwidth phase-differencing on top.

In Figure I.7 we show a comparison between the zero-lag methods and CCC. In the upper panel we show the estimated pixel shift from CCC. The steps in the shift are due to the finite sampling inside CCC. In the center panel we compare the estimated coherence between the the zero-lag methods and CCC. Notice the significant coherence loss which occurs when the shift is more than a twentieth of a resolution cell. Since we have simulated a system where the resolution is comparable to the wavelength, we observe significant coherence loss even

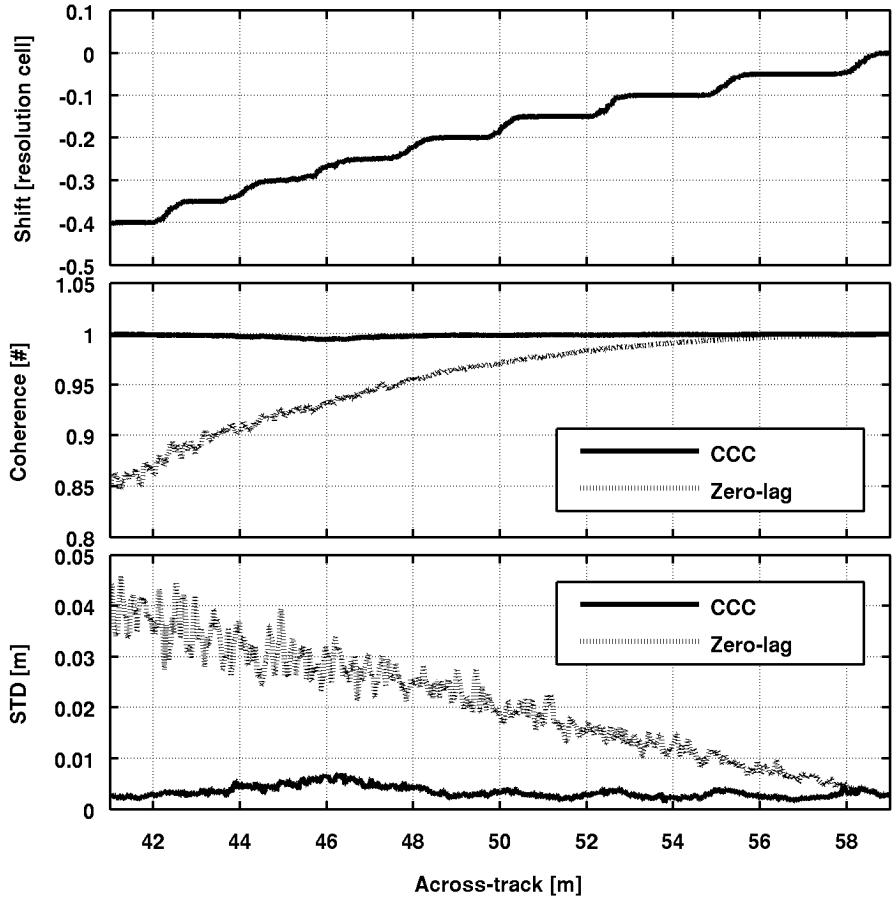

Figure I.7: Estimated across-track pixel shift (top), estimated coherence (center) and estimated standard deviation (bottom) as a function of across-track distance. The results are the average over 400 along-track lines in the flat region of our noise-free simulated data.

below the usual coregistration demand of approximately a tenth of a resolution cell (Hanssen, 2001). In the lower panel we show the corresponding standard deviation of the estimate. Note that all methods are unbiased. For a realistic SNR the curves would have been much closer, but the figure illustrates that for high SNR, any misregistration would cause coherence loss for the zero-lag methods.

In Figure I.8 we show the simulated and estimated bathymetry on the simulated wreck. All the absolute phase difference estimators have very few wrap-errors, but they fail in the layover region (due to the overlap of responses from the wreck and seafloor). On the wreck, however, there is a significant shift in the interferometric images and therefore CCC performs best. For WSSA, we have used 5 dense subbands. We also tested the Goldstein‘s Branch cut algorithm, and it fails severely in reconstructing the depth of the wreck.

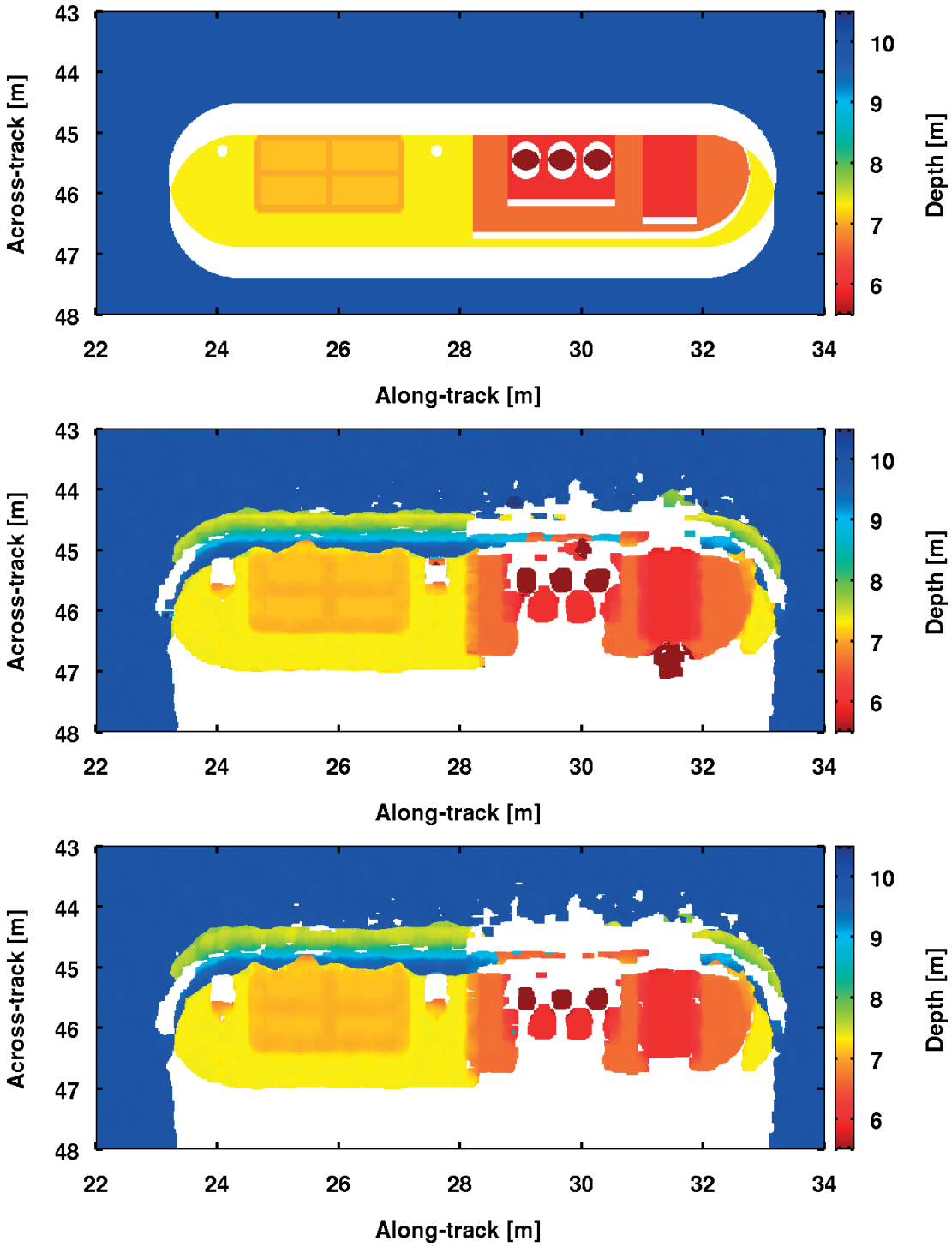

Figure I.8: Model bathymetry (top), CCC based bathymetry (center) and WSSA based bathymetry (bottom). In the model, both the layover region and the shadow region have been removed. In the center and lower panel all estimates with a coherence below 0.55 are removed. The average SNR in the SAS images are around 10 dB.

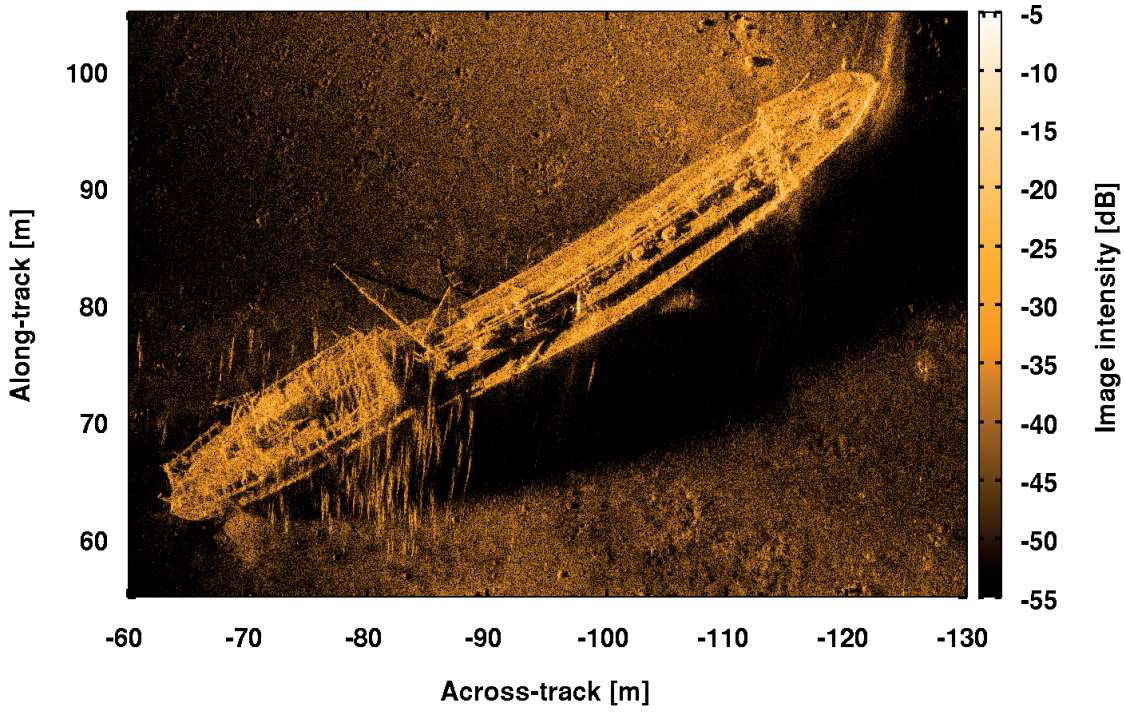

Figure I.9: SAS image of the wreck of the Holmengraa. Data courtesy of Kongsberg Maritime.

I.6 Experimental Results

We have tested the wideband interferometry methods on real data collected with a HISAS 1030 interferometric SAS (see Figure I.1). The data were collected in February 2012, south of Horten, Norway, at approximately 77 m water depth. As for the simulated data, the experimental data are collected using 30 kHz bandwidth around 100 kHz center frequency, and with a 30 cm vertical baseline. The object of interest is the wreck of the 1500 dead weight tons oil tanker Holmengraa, that was sunk during World War II. The length of the wreck is 68 m, and the width is 9 m. Figure I.9 shows the SAS image of the wreck. The range to the center of the image is 95 m, and the image size is 50 x 80 m. The bright lines on top of the bridge in the lower left corner of the image, is a school of fish. The theoretical resolution in the image is around 3 x 3 cm, and the grid resolution is 2 x 2 cm. Figure I.10 shows CCC based coherence and interferogram. We see that the coherence is very high (red color) in the flat areas around the wreck, and on some parts of the wreck. In the shadow region, and over complex areas of the wreck, the coherence is low (blue color). The interferometric phase difference (lower panel) varies slowly over the seafloor surrounding the wreck. On the wreck, especially in the aft part, there are rapid variations and disconnected regions, which will cause difficulties for 2D phase unwrappers.

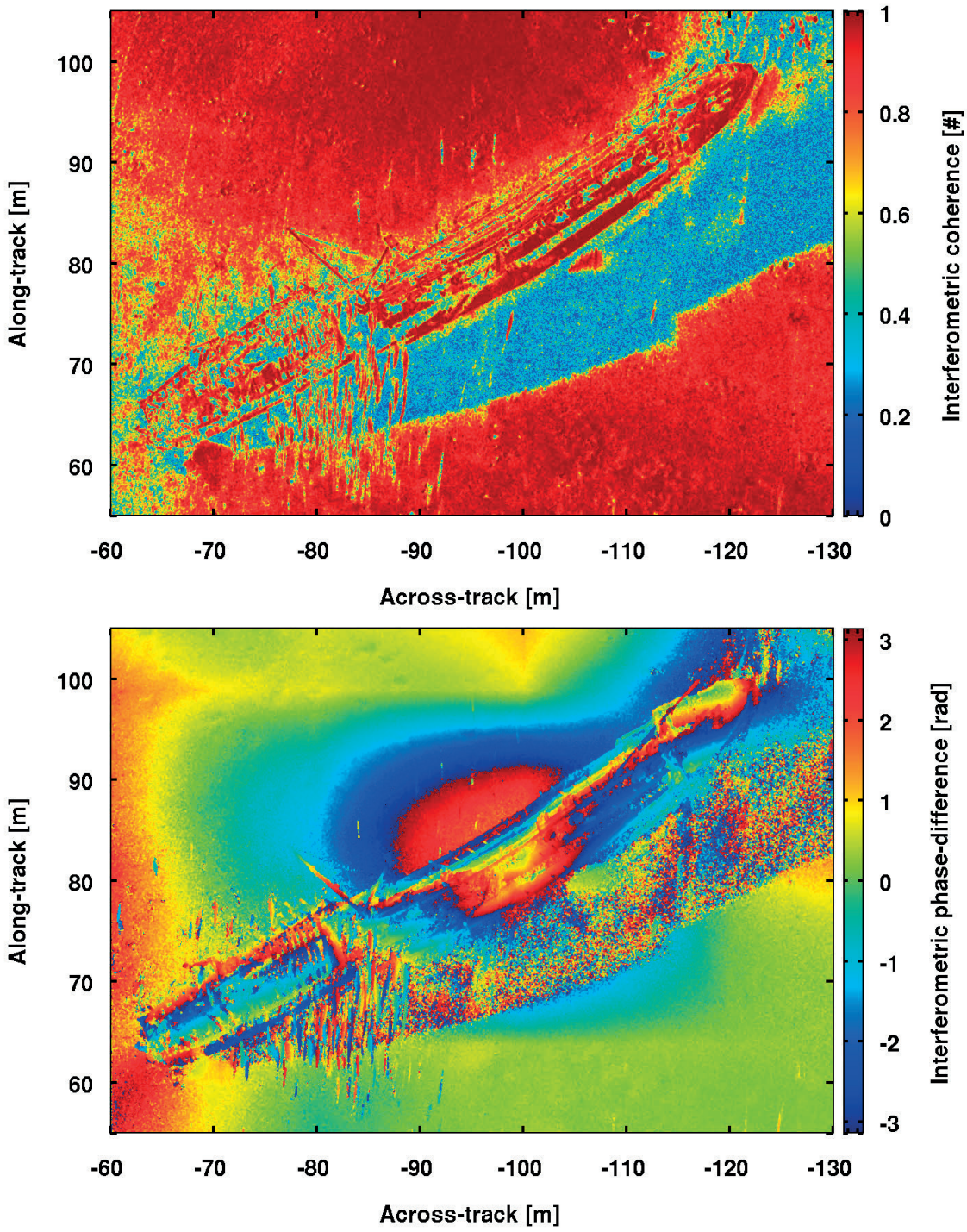

Figure I.10: Cross correlation based coherence (upper panel) and interferogram (lower panel) of the scene shown in Figure I.9.

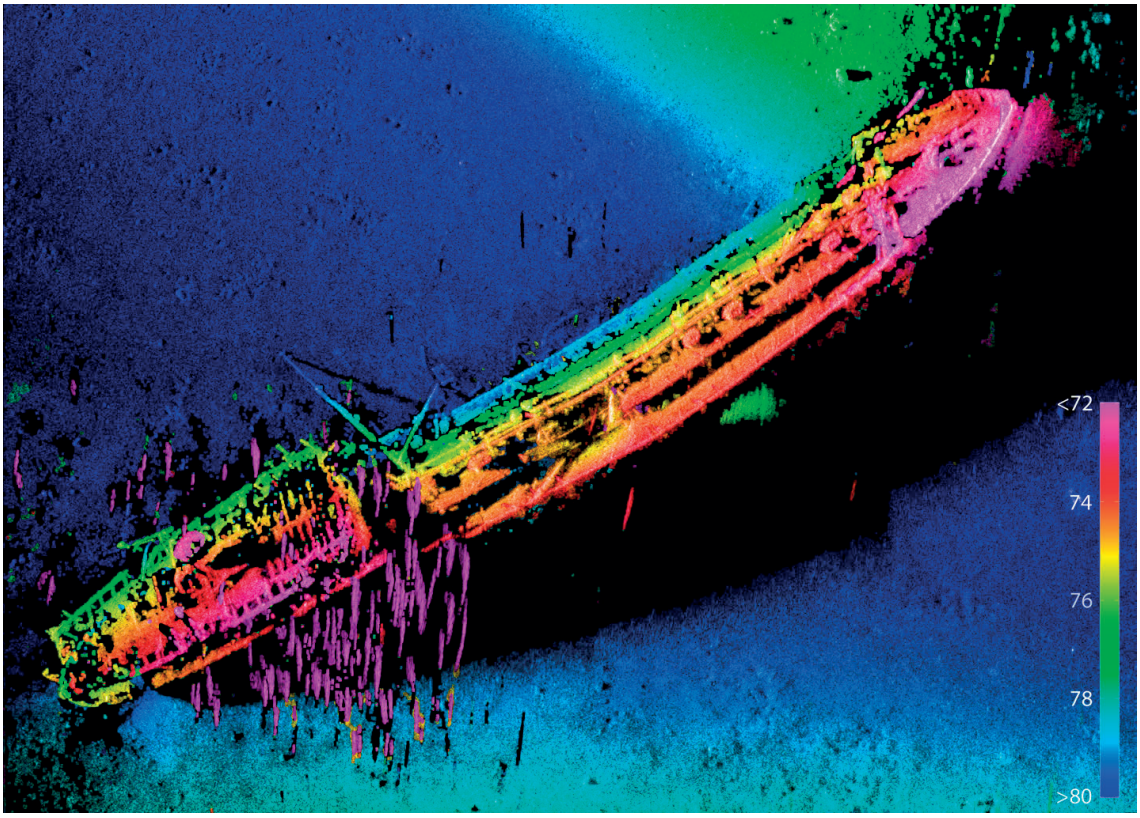

Figure I.11: Wideband SAS interferometry results based on a fusion of image, coherence and bathymetry of the image shown in Figure I.9. Depth is color coded, and brightness is based on image intensity and coherence. The colorbar shows depth in meters relative to the sloping imaging plane which is fitted to match the a-priori seafloor depth. The depth estimates are based on the CCC technique. Data courtesy of Kongsberg Maritime, Norway.

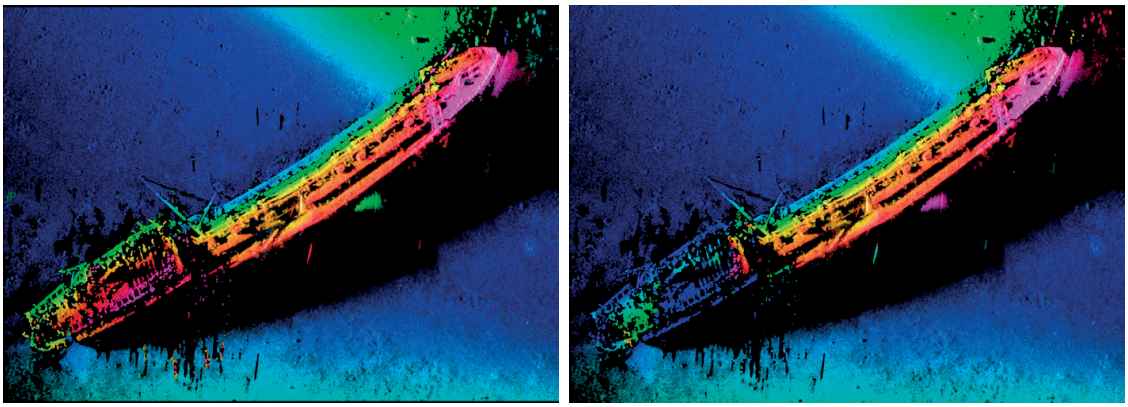

Figure I.12: Fusion of SAS image, coherence and bathymetry. Left: WSSA. Right: Goldstein's Branch cut algorithm. See Figure I.11 for comparison with CCC.

Figure I.11 and Figure I.12 show the wideband SAS interferometry results based on CCC, WSSA and Goldstein's Branch cut algorithm. We see that all three techniques are performing well on the seafloor around the wreck, and on the fore part of the wreck. On the bridge (the aft part), the Goldstein algorithm fails badly. WSSA performs satisfactory and produces plausible depth estimates of all parts of the wreck. CCC performs even better, having more valid measurements compared to WSSA due to the local coregistration. In addition, CCC also produces probable depth estimates of the school of fish (red stripes over the bridge of the wreck in the lower left corner). This part of the image has severe layover with a large elevated structure on the wreck and a school of fish on top.

The fish over the bridge are moving targets that move a large number of wavelengths during the synthetic aperture data acquisition. They therefore cause defocus (Chen et al., 2002, chapter 7) in the SAS image, and each fish mainly appear as a stripe along-track. Somewhat surprisingly, CCC coherence is high on the defocused fish. This is due to the fact that the defocus is approximately equal on the master and slave image, and high coherence is maintained.

I.7 Conclusions

In this paper we have considered different techniques for estimating absolute phase difference in wideband synthetic aperture sonar interferometry. The benefit of using such techniques is that a 2D phase unwrapper where prior knowledge or specific properties of the data is assumed is not needed. The studied techniques are the complex cross correlation (CCC), the split-spectrum algorithm (SSA), the multi-chromatic approach (MCA), and the weighted split-spectrum algorithm (WSSA). We have benchmarked the techniques on a simulated scenario, and demonstrated the techniques on real data. WSSA obtained the best performance on the flat area while CCC obtained the best performance on complicated topographies. MCA has similar performance as multiband SSA for the same choice of subbands. In our implementation, multiband SSA is much faster than MCA. We have found that all four wideband interferometry techniques seems well suited for the HISAS wideband interferometric SAS, and they all outperform a standard Goldstein's Branch cut phase unwrapping algorithm on real data containing a complicated scene containing an elevated target and severe layover.

Acknowledgements. The authors thank Kongsberg Maritime for the kind permission to use data recorded with their HUGIN 1000 AUV. The authors also thank Hayden Callow at Kongsberg Maritime for fruitful discussions and valuable input.

References

Bamler, R. and Eineder, M. (2004). "Split band interferometry versus absolute ranging with wideband SAR systems". In: *Proceedings of the IEEE Interna-*

tional Geoscience and Remote Sensing Symposium (IGARSS). Anchorage, Alaska, pp. 980–984.

Bamler, R. and Eineder, M. (2005). "Accuracy of differential shift estimation by correlation and split-bandwidth interferometry for wideband and delta-k SAR systems". In: *IEEE Geoscience and Remote Sensing Letters* vol. 2, no. 2, pp. 151–155.

Bamler, R. and Hartl, P. (1998). "Synthetic aperture radar interferometry". In: *Inverse Problems* vol. 14, R1–R54.

Bonifant Jr, W. W., Richards, M. A., and McClellan, J. H. (2000). "Interferometric height estimation of the seafloor via synthetic aperture sonar in the presence of motion errors". In: *IEE Proc. Radar, Sonar Navig.* vol. 147, no. 6, pp. 322–330.

Bovenga, F., Giacovazzo, V. M., Refice, A., Veneziani, N., and Vitulli, R. (2009). "A first validation experiment for a Multi-Chromatic Analysis (MCA) of SAR data starting from SLC images". In: *Proceedings of IGARSS'09*. Cape Town, South Africa.

Bovenga, F., Giacovazzo, V., Refice, A., Veneziani, N., Derauw, D., and Vitulli, R. (2011). "Interferometric multi-chromatic analysis of TerraSAR-X data". In: *TerraSAR-X Science Team Meeting*. Oberpfaffenhofen, Germany.

Brcic, R., Eineder, M., and Bamler, R. (2009). "Interferometric absolute phase determination with TerraSAR-X wideband SAR data". In: *Proceedings of IEEE Radar Conference 2009*. Pasadena, California.

Carter, G. C. (1987). "Coherence and Time Delay Estimation". In: *Proc. IEEE* vol. 75, no. 2, pp. 236–255.

Chen, V. C. and Ling, H. (2002). *Time-Frequency Transforms for Radar Imaging and Signal Analysis*. Boston, MA: Artech House.

Fornaro, G. and Franceschetti, G. (1995). "Image registration in interferometric SAR processing". In: *IEE Proc. Radar, Sonar Navig.* vol. 142, no. 6, pp. 313–320.

Fossum, T. G., Sæbø, T. O., Langli, B., Callow, H. J., and Hansen, R. E. (2008). "HISAS 1030 - High resolution interferometric synthetic aperture sonar". In: *Proceedings of the Canadian Hydrographic Conference and National Surveyors Conference*. Victoria, BC, Canada, pp. 1–11.

Ghiglia, D. C. and Pritt, M. D. (1998). *Two-Dimensional Phase Unwrapping: Theory, Algorithms, and Software*. John Wiley & Sons, INC, p. 512.

Griffiths, H. D., Rafik, T. A., Meng, Z., Cowan, C. F. N., Shafeeu, H., and Anthony, D. K. (1997). "Interferometric synthetic aperture sonar for high resolution 3-D mapping of the seabed". In: *IEE Proceedings - Radar, Sonar and Navigation* vol. 144, no. 2, pp. 96–103.

Griffiths, H. D. (1997). "A comparison between radar and sonar synthetic aperture interferometry". In: *IEE Colloquium on Radar Interferometry*. 153, pp. 4/1–4/5.

Hagen, P. E., Fossum, T. G., and Hansen, R. E. (2008). "HISAS 1030: The Next Generation Mine Hunting Sonar for AUVs". In: *UDT Pacific 2008 Conference Proceedings*. Sydney, Australia.

Hagfors, T. (1961). "Some Properties of Radio Waves Reflected from the Moon and Their Relation to the Lunar Surface". In: *J. Geophys Res.* vol. 66, no. 3, pp. 777–785.

Hansen, R. E. (2011). "Introduction to Synthetic Aperture Sonar". In: *Sonar Systems*. Ed. by Kolev, N. Z. Intech. Chap. 1, pp. 3–28. URL: http://www.intechopen.com/books/show/title/sonar-systems.

Hansen, R. E., Callow, H. J., Sæbø, T. O., and Synnes, S. A. V. (2011). "Challenges in Seafloor Imaging and Mapping with Synthetic Aperture Sonar". In: *IEEE Trans. Geosci. Remote Sens.* vol. 49, no. 10, pp. 3677–3687.

Hanssen, R. F. (2001). *Radar Interferometry: Data Interpretation and Error Analysis*. 1st ed. Dordrecht, The Netherlands: Kluwer Academic Publishers, p. 308.

Hayes, M. P. and Gough, P. T. (2009). "Synthetic Aperture Sonar: A Review of Current Status". In: *IEEE J. Oceanic Eng.* vol. 34, no. 3, pp. 207–224.

Hong, S.-H., Jung, H.-S., and Won, J.-S. (2006). "Extraction of ground control points (GCPs) from synthetic aperture radar images and SRTM DEM". In: *International Journal of Remote Sensing* vol. 27, no. 18, pp. 3813–3829.

Jakowatz, J. C. V., Wahl, D. E., Eichel, P. H., Ghiglia, D. C., and Thompson, P. A. (1996). *Spotlight-Mode Synthetic Aperture Radar: A Signal Processing Approach*. 1st ed. Springer, Boston, MA, USA, p. 429.

Johnson, D. H. and Dudgeon, D. E. (1993). *Array Signal Processing: Concepts and Techniques*. Signal processing series. Englewood Cliffs, NJ, USA: Prentice Hall.

Kay, S. M. (1993). *Fundamentals of Statistical Signal Processing: Estimation Theory*. Prentice Hall International Editions.

Knapp, C. K. and Carter, G. C. (1976). "The Generalized Correlation Method for Estimation of Time Delay". In: *IEEE Trans. Acoust., Speech, Signal Process.* vol. ASSP-24, no. 4, pp. 320–327.

Loffeld, O., Nies, H., Knedlik, S., and Wang, Y. (2008). "Phase Unwrapping for SAR Interferometry - A Data Fusion Approach by Kalman Filtering". In: *IEEE Trans. Geosci. Remote Sens.* vol. 46, no. 1, pp. 47–58.

Madsen, S. N. and Zebker, H. A. (1992). "Automated absolute phase retrieval in across-track interferometry". In: *Proceedings of the International Geoscience and Remote Sensing Symposium (IGARSS)*. Houston, Texas, USA, pp. 1–3.

Madsen, S. (1995). "Absolute phase determination techniques in SAR interferometry". In: *Proceedings of SPIE*. Vol. 2487, p. 393.

Nico, G., Palubinskas, G., and Datcu, M. (2000). "Bayesian approaches to phase unwrapping: theoretical study". In: *IEEE Trans. Signal Process.* vol. 48, no. 9, pp. 2545–2556.

Pascazio, V. and Schirinzi, G. (2001). "Estimation of terrain elevation by multifrequency interferometric wide band SAR data ". In: *IEEE Signal Proc. Lett.* vol. 8, no. 1, pp. 7–9.

Pascazio, V. and Schirinzi, G. (2002). "Multifrequency InSAR height reconstruction through maximum likelihood estimation of local planes parameters". In: *IEEE Trans. Image Process.* vol. 11, no. 12, pp. 1478–1489.

Reigber, A. and Moreira, A. (2000). “First Demonstration of Airborne SAR Tomography Using Multibaseline L-Band Data”. In: *IEEE Trans. Geosci. Remote Sens.* vol. 38, no. 5, pp. 2142–2152.

Rosen, P. A., Hensley, S., Joughin, I. R., Li, F. K., Madsen, S. N., Rodriguez, E., and Goldstein, R. M. (2000). “Synthetic Aperture Radar Interferometry”. In: *Proc. IEEE* vol. 88, no. 3, pp. 333–382.

Seymour, M. S. and Cumming, I. G. (1994). “Maximum Likelihood Estimation for SAR Interferometry”. In: *Proceedings of IGARSS’94*. Vol. 4. IEEE. Pasadena, California, pp. 2272–2275.

Sæbø, T. O. (2010). “Seafloor Depth Estimation by means of Interferometric Synthetic Aperture Sonar”. PhD thesis. University of Tromsø, Norway.

Sæbø, T. O. and Hansen, R. E. (2010a). “Comparison between Interferometric SAS and Interferometric SAR”. In: *Proceedings of Synthetic Aperture Sonar and Radar 2010*. Lerici, Italy.

Sæbø, T. O., Hansen, R. E., and Hanssen, A. (2007). “Relative Height Estimation by Cross-correlating Ground-Range Synthetic Aperture Sonar Images”. In: *IEEE J. Oceanic Eng.* vol. 32, no. 4, pp. 971–982.

Sæbø, T. O. and Langli, B. (2010b). “Comparison of EM 3000 multibeam echo sounder and HISAS 1030 interferometric synthetic aperture sonar for seafloor mapping”. In: *Proceedings of European Conference on Underwater Acoustic (ECUA) 2010*. Istanbul, Turkey, pp. 451–461.

Ulander, L. M. H. and Frölind, P.-O. (1998). “Ultra-Wideband SAR Interferometry”. In: *IEEE Trans. Geosci. Remote Sens.* vol. 36, no. 5, pp. 1540–1550.

Veneziani, N., Bovenga, F., Lovergine, F., and Refice, A. (2000). “A frequency domain differential approach to the absolute phase retrieval in SAR interferometry”. In: *Proceedings of IGARSS’00*. Honolulu, Hawaii.

Veneziani, N., Bovenga, F., and Refice, A. (2003). “A wide-band approach to the absolute phase retrieval in SAR interferometry”. In: *Multidimensional Systems and Signal Processing* vol. 14, pp. 183–205.

Veneziani, N. and Giacovazzo, V. (2006). “A multi-chromatic approach to SAR interferometry: differential analysis of interferograms at close frequencies in the spatial domain and frequency domain”. In: *Proceedings of IGARSS’06*. IEEE, pp. 3723–3726.

Weinstein, E. and Weiss, A. (1984). “Fundamental limitations in passive time-delay estimation–Part II: Wide-band systems”. In: *IEEE Trans. Acoust., Speech, Signal Process.* vol. 32, no. 5, pp. 1064–1078.

Weiss, A. and Weinstein, E. (1983). “Fundamental limitations in passive time delay estimation–Part I: Narrow-band systems”. In: *IEEE Trans. Acoust., Speech, Signal Process.* vol. 31, no. 2, pp. 472–486.

Zhu, X. and Bamler, R. (2012). “Demonstration of Super-Resolution for Tomographic SAR Imaging in Urban Environment”. In: *IEEE Trans. Geosci. Remote Sens.* vol. 50, no. 8, pp. 3150–3157.

Paper II

Wideband Synthetic Aperture Sonar Back Projection with Maximization of Wavenumber-Domain Support

II

Stig Asle Vaksvik Synnes, Alan Joseph Hunter, Roy Edgar Hansen, Torstein Olsmo Sæbø, Hayden John Callow, Robbert van Vossen, Andreas Austeng

Abstract

Wideband and widebeam synthetic aperture sonar (SAS) can provide information on the frequency- and aspect-dependent scattering in a scene. We suggest an approach to predict the quality of the sensor data over the available frequencies and aspect angles. We relate the typical spatial domain quality metrics to their wavenumber domain counterpart, and use these to map the data quality in the wavenumber domain. Because SAS arrays often are under-sampled along-track, we pay particular attention to data degradation from aliasing. We use the proposed approach to examine how three SAS image formation algorithms based on time domain back projection access data of different quality from wideband SAS systems. We illustrate the results with predictions for a generic SAS design and demonstrate the findings on two experimental systems. We observe that the maximum support of high-quality data is achieved through back projection on to a high resolution grid followed by wavenumber domain filtering.

Synnes, Hansen and Sæbø are with the Norwegian Defence Research Establishment (FFI), Norway. Synnes is also pursuing a Ph.D. at the University of Oslo, Norway, and Hansen is also adjunct associate professor at the University of Oslo. Austeng is with the University of Oslo where he is associate professor. Hunter is lecturer with the University of Bath, United Kingdom. Callow is with Kongsberg Maritime, Norway. van Vossen is with the Netherlands Organisation for Applied Scientific Research (TNO), The Netherlands.

II.1 Introduction

Synthetic aperture sonar (SAS) has become an established technique for high resolution imaging of the seafloor (Hansen, 2011),(Hayes et al., 2009). Wideband SAS can provide information on the frequency dependence of the acoustic bottom scattering, and at lower frequencies (LF) also of sub-bottom scattering. In addition, widebeam systems increase the probability of echo signals in directions with strong specular scattering (Schock et al., 2001). Applications of LF wideband SAS include naval mine hunting and underwater unexploded ordnance (UXO) remediation with potential of improved detection and classification of both proud and buried targets, together with estimation of the probability of target burial (Christoff et al., 2002),(Williams et al., 2010),(Hunter et al., 2014; Synnes et al., 2015),(Nielsen et al., 2013). Seabed mapping and characterization (Sternlicht et al., 2013) and underwater archeology (Ødegård et al., 2013) may also take advantage of LF and wideband SAS. In this paper we let wideband denote systems with fractional bandwidth $B/f_c \gtrsim 1$, where B represents bandwidth and f_c the center frequency. The upper limit is a full bandwidth system of $B/f_c = 2$. Typical wideband SAS systems are also LF and include the SAMI (5-10 kHz) (Châtillon et al., 1999), BOSS (5-23 kHz) (Schock et al., 2001), MUD (1-4 kHz, 4-9 kHz, 11-26 kHz) (Beckers et al., 2012) and HISAS with LF prototype extension (12-38 kHz concurrently with 60-85 kHz) (Synnes et al., 2013). In these systems the bandwidth at transmission is obtained using one to three transmitters, while at reception each element of the receiver array(s) cover the the entire frequency band.

SAS images map the scattering strength over the scene, and this is strongly influenced by its geometry. Wideband and widebeam systems also provide information on the frequency- and aspect-dependence of the scattering. In order to provide the best starting point for extracting the frequency- and aspect-dependence of scattering, we suggest building a SAS image with the maximum support of high-quality data. We consider different methods for preparing such a SAS image. We suggest that for the derivation of frequency- and aspect-dependence of the scattering, the SAS processing algorithms should be rated based on how they address data of different quality in the wavenumber domain, rather than on a spatial domain image quality that assumes frequency- and aspect-independent scattering. We develop wavenumber domain counterparts of the common spatial domain SAS image quality metrics. We apply these metrics on alternative wideband SAS imaging approaches and a typical SAS design, and on experimental data from two wideband LF SAS systems.

SAS image formation algorithms operate either in the time domain (TD) (Johnson et al., 1993, chapter 4.1),(Soumekh, 1999, chapter 4.7) or in the wavenumber domain (WD)(Soumekh, 1999, chapter 4.5),(Cumming et al., 2005, part II),(Franceschetti et al., 1999, chapter 3). In general the wavenumber domain algorithms are more efficient with respect to computational cost, but can be applied only for trajectories that closely align with one of the coordinate axes

of a separable coordinate system. Linear track wavenumber domain imaging is most common, but also circular tracks have been accommodated (Ferguson et al., 2009). The wavenumber domain algorithms can be adapted to handle small deviations to the ideal track, but at the cost of increased complexity and processing speed (Madsen, 2001). Time domain algorithms produce the best image quality for non-ideal trajectories, but are in general slower (Frey et al., 2009).

In this study we evaluate the performance of different SAS imaging approaches that starts with time domain back projection (BP). The beamwidth of wideband systems can change significantly with frequency, and processing the maximum valid beamwidth for all frequencies has the potential of providing the maximum information on the scene. However, standard BP image formation does not support processing frequency-dependent beamwidths. For wideband systems, splitting the signal into multiple bands and processing each band separately has been suggested to mitigate the negative effects of this limitation (Châtillon et al., 1992),(Hayes et al., 1992). However, new artifacts are introduced from merging sub-band images, as a result of the irregular shape of the combined wavenumber domain coverage. In Section II.3.3 we investigate a third algorithm that takes full use of the available SAS information from wideband systems. This algorithm is based on time domain back projection followed by wavenumber domain filtering. We evaluate the extra computational load related to this hybrid time- and wavenumber domain algorithm.

Our main contribution is a new method for evaluating imaging algorithms, in which we address how they use the information on the scene provided by a wideband SAS system. Primary quality metrics for synthetic aperture imagery are resolution (mainlobe -3 dB width), peak sidelobe ratio, multiplicative noise ratio (from multipaths, sidelobes and grating lobes), additive noise level and geometric distortion (Carrara et al., 1995, chapter 8.1),(Curlander et al., 1991, chapter 6.2). The relative importance of the image quality metrics strongly depends on the application, with its priority of resolution versus suppression of sidelobes and grating lobes (Curlander et al., 1991, chapter 6.5).

We map the data quality in the wavenumber domain expressed through signal to ambient noise ratio (SNR) and signal to grating lobe ratio (SGR), and keep in mind that resolution is directly related to the wavenumber domain coverage. For each of the three imaging algorithms; back projection (BP), multiband back projection (MBP) and wideband back projection (WBP), we map their inherent windowing functions in the wavenumber domain. This allows us to investigate how the different imaging algorithms access data of different quality at different wavenumbers.

We show that the WBP method provides the best wavenumber domain data support, and thus also the best foundation for establishing any frequency- and aspect dependencies of the scattering strength. We do not attempt to address the

quality of the corresponding full-band spatial domain imagery, but expect that the difference between the imaging algorithms will be less prominent as a result of reduced wavenumber domain coverage from the windowing functions used to suppress side-lobes, and from of any frequency- and aspect-dependence of the scattering. The validity of our approach for evaluating data quality is supported by real data measurements from a HISAS system with LF prototype extension on the HUGIN HUS autonomous underwater vehicle (AUV) of the Norwegian Defence Research Establishment (FFI) and from the MUD LF SAS prototype of the Netherlands Organisation for Applied Scientific Research (TNO).

In Section II.2 we give a brief introduction to SAS image formation, address some of the challenges of wideband LF SAS image formation, and give an interpretation of SAS imaging in the wavenumber domain. In Section II.3 we present the three algorithms for image formation in detail. We develop our approach for comparing the performance of different imaging algorithms in Section II.4, with focus on the wavenumber domain data quality. Next we present our wavenumber counterpart to the spatial domain quality metrics in Section II.5. This is also where we compare the performance of the imaging algorithms through an investigation of coverage, SNR and SGR over the wavenumber domain. In Section II.6 we illustrate our findings on data from the two experimental LF SAS systems. Finally we conclude in Section V.9.

II.2 SAS Imaging

SAS images represent information on the backscattering over a scene. In SAS image formation, data from multiple pings are combined coherently in order to synthesize an aperture that is significantly longer than the physical aperture. SAS thus provides increased resolution. Moreover, it provides resolution that is independent of range and frequency when using a fixed-size transducer for all frequencies (Hansen, 2011). Using the same elements over wide frequency spans is the common choice for many SAS-systems (Schock et al., 2001),(Châtillon et al., 1999),(Beckers et al., 2012),(Synnes et al., 2013).

II.2.1 Time Domain Back Projection

SAS image formation by time domain back projection (BP) is also known as delay-and-sum (DAS) beamforming. In this algorithm the received signal is back projected for each ping, from the receiver via each pixel in the scene and into the transmitter (Johnson et al., 1993, chapter 4.1),(Soumekh, 1999, chapter 4.7). This can be summarized as follows: Let i represent ping number, $\boldsymbol{u}_i$ the position along the platform trajectory at ping i and $\boldsymbol{x}$ represent the point to be probed (imaged). Let $\sigma(t)$ represent the received signal for the round-trip period $t(\boldsymbol{x}, \boldsymbol{u}_i)$; from the along-track position $\boldsymbol{u}_i$, to the pixel at position $\boldsymbol{x}$ and back, c.f. Figure II.1. We form the matched-filtered signal, $s_i(t, \boldsymbol{u}_i)$, by cross-correlating

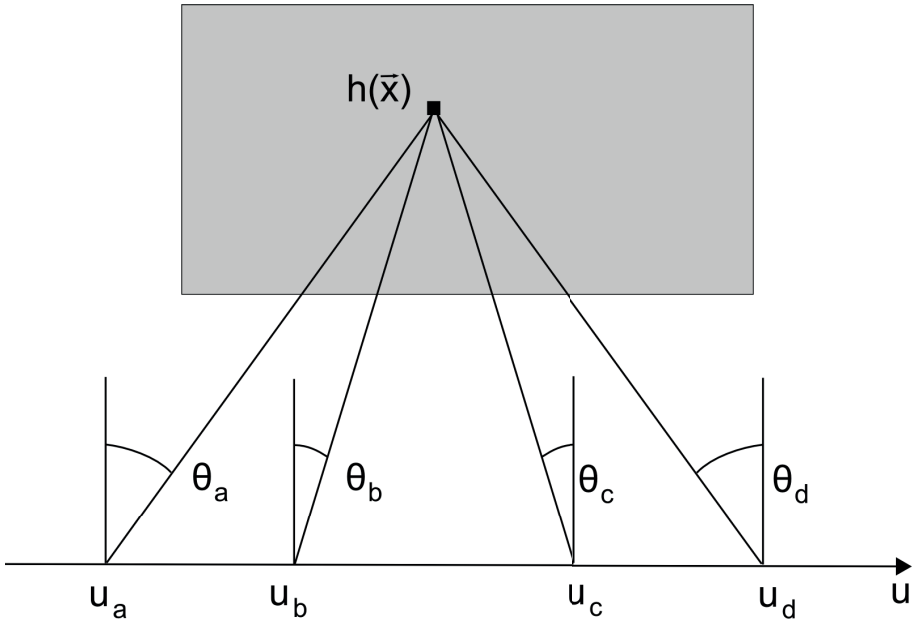

Figure II.1: Imaging geometry for transducer elements of the same size d on two frequency bands: The aperture from u_b to u_c is required to obtain resolution $d/2$ at the upper frequency band with -3 dB beamwidth of $\theta_b - \theta_c$, while the aperture u_a to u_d is required to obtain the same resolution at the lower frequency with -3 dB beamwidth of $\theta_a - \theta_d$. The corresponding image wavenumber domain coverages are shown in Figure II.2.

the received signal $\sigma(t)$ with the transmitted signal $p(t)$:

$$s_i(t, \boldsymbol{u}_i) = \sigma_i(t, \boldsymbol{u}_i) * p^*(-t). \tag{II.1}$$

The scattering coefficient can now be estimated using the expression

$$h(\boldsymbol{x}) = \frac{1}{\beta} \sum_{i \in i_\beta} \mathrm{w}(\theta(\boldsymbol{x}, \boldsymbol{u}_i)) s_i(t(\boldsymbol{x}, \boldsymbol{u}_i), \boldsymbol{u}_i) \Delta\theta(\boldsymbol{x}, \boldsymbol{u}_i), \tag{II.2}$$

where $\mathrm{w}(\theta)$ is an optional weighting function, and $\Delta\theta(\boldsymbol{x}, \boldsymbol{u}_i)$ is the angular span represented by ping i,

$$\Delta\theta(\boldsymbol{x}, \boldsymbol{u}_i) = \theta(\boldsymbol{x}, (\boldsymbol{u}_i + \boldsymbol{u}_{i+1})/2) - \theta(\boldsymbol{x}, (\boldsymbol{u}_i + \boldsymbol{u}_{i-1})/2). \tag{II.3}$$

Here $\theta(\boldsymbol{x}, \boldsymbol{u}_i)$ is the look angle, defined as the angle between the line of sight and the y-coordinate of the image. The summation of (II.2) is over all pings within the processing beamwidth β, i.e. $i_\beta = \{i | \theta(\boldsymbol{x}, \boldsymbol{u}_i) \in \langle -\beta/2, \beta/2 \rangle\}$, and the leading factor $1/\beta$ is a normalization on the processed beamwidth. The received signal must be sampled in accordance with the Nyquist criterion, both temporally and spatially, in order to eliminate aliasing (ambiguities)(Johnson et al., 1993, chapter 3.2). Artifacts caused by spatial aliasing are commonly referred to as grating lobes.

As mentioned in Section II.1, a limitation of time domain back projection is that the processing beamwidth is independent of frequency and the same limitation also applies to the weighting function $\mathrm{w}(\theta)$.

The SAS image formation described in (II.2) does not account for geometric spreading and absorption, nor for the element beampattern. However, it is straightforward to account for the spreading loss in the time domain matched filtering and the element beampattern in the wavenumber domain. The absorption loss is both frequency- and range dependent, but can also be accounted for in a matched filter.

II.2.2 Challenges of Wideband SAS

Challenges of SAS imaging include requirements on navigation accuracy, sound speed accuracy and bathymetric accuracy, together with multiplicative noise due to multipath (Hansen et al., 2011).

In this paper we address the wideband-specific challenge of processing a frequency dependent beamwidth. This challenge must be met in order to include data for processing based on the data quality. The relevance of the problem is illustrated in Figure II.1, showing the synthetic apertures (and span of azimuth-angles) at two frequencies for a wideband SAS system. In order to fully exploit the sensor data, frequency-dependent processing beamwidth is required. This becomes increasingly more important for systems with higher fractional bandwidth.

II.2.3 Image Wavenumber Spectrum

The image wavenumber spectrum is important for wideband data analysis, as it can be interpreted as a map of the response of scene and processing as a function of frequency and look angle. Furthermore, the wavenumber coverage has a direct relation to the point-spread function, and we will later investigate how the various imaging algorithms can be distinguished from one another by addressing the shape of their image wavenumber domain coverage.

We let the image wavenumber spectrum $H(\boldsymbol{K})$ be the 2D Fourier transform of the complex SAS image $h(\boldsymbol{x})$, denoting the image wavenumber vector $\boldsymbol{K}$, following (Soumekh, 1999, chapter 4), (Soumekh, 1994, chapter 4.3), (Ferguson et al., 2009). The image wavenumber vector, also known as the Bragg wavenumber vector or the scattering wavenumber vector, expresses the difference between the reflected and incident wavenumber vectors, $\boldsymbol{k}_{re}$ and $\boldsymbol{k}_{in}$, of the target scattering for a general bi-static configuration (Ishimaru, 1978, Section 16-2):

$$[K_x, K_y] = \boldsymbol{K} = \boldsymbol{k}_{re} - \boldsymbol{k}_{in}. \tag{II.4}$$

For small baseline (distance between transmitter and receiver) we can make the approximations:

$$|\boldsymbol{K}| \quad \approx \quad 2k, \text{ where } k = \frac{2\pi f}{c} \tag{II.5}$$

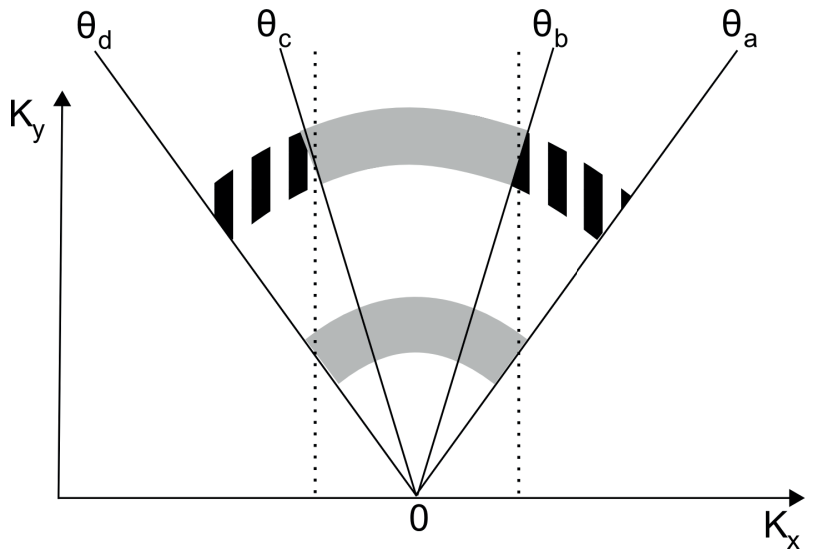

Figure II.2: Coverage in the image wavenumber domain for the upper and lower frequency bands of the imaging geometry in Figure II.1. The dotted lines indicate the -3 dB beamwidth for any frequency. The figure illustrates that when recording data within the -3 dB beamwidth at the low frequency (θ_a to θ_d), we record data within the -3 dB beamwidth at the high frequency (θ_b to θ_c), but also record undesired wavenumbers outside this region as indicated by the black striped areas. Alternatively the data can be processed from θ_b to θ_c, but then valid wavenumbers would be missing for the low frequency.

$$\angle \boldsymbol{K} \quad \approx \quad \theta \tag{II.6}$$

which correspond to a monostatic transmitter/receiver configuration. Here k is the propagating wavenumber at frequency f for phase velocity c, while θ is the aspect angle at which each pixel is observed. In order to give an alias-free representation of the image wavenumber spectrum with discrete sampling, the image grid must meet the Nyquist criterion over the span of the processed bandwidth and beamwidth.

In Figure II.2 we illustrate how the image wavenumber spectrum is populated, given the geometry of Figure II.1. The processed pings are being distributed over an arc length proportional to K, such that the sample density in the K_x, K_y-plane is proportional to $1/K$.

The relation between the spatial image and the image wavenumber spectrum is illustrated on real data in Figure II.3 and Figure II.4, and the image has been formed using the wideband back projection algorithm of Section II.3.3. The SAS data were recorded by HISAS with a LF prototype extension. Here the wavenumber spectrum contains all the data collected on the scene, and the image was formed by processing the along-track wavenumbers K_x over the span indicated by the vertical lines, and compensating for the sample density of $1/K$.

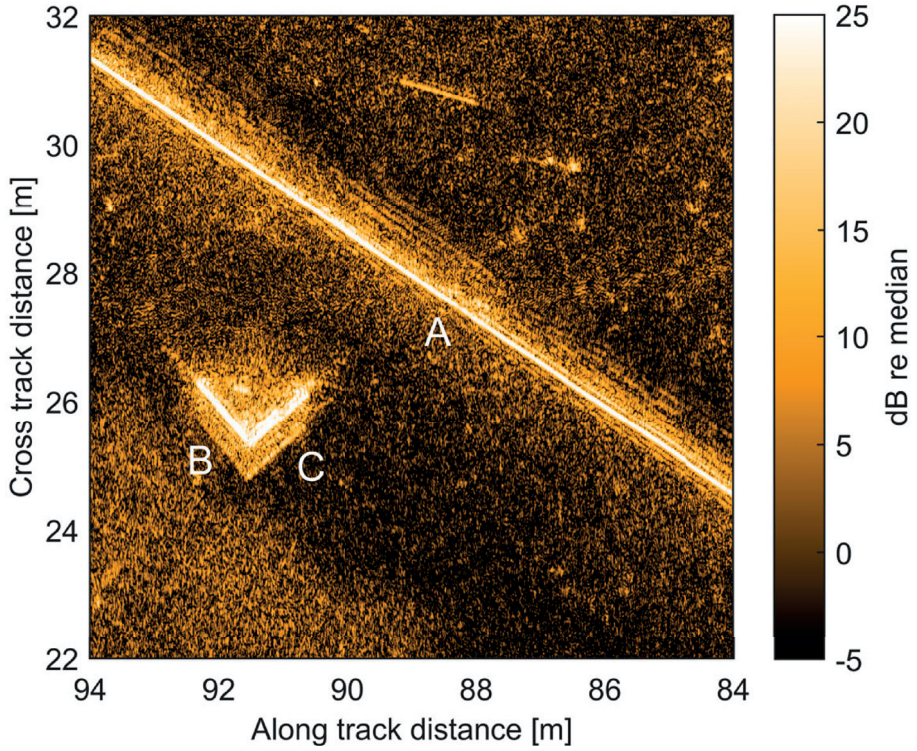

Figure II.3: Spatial domain SAS image at 12-38 kHz processed over the -3 dB bandwidth indicated in Figure II.4. The image shows a 1.2 m x 1.2 m concrete block next to a 0.9 m diameter pipeline. The collected wavenumber domain spectrum is shown in Figure II.4. The data were recorded by HISAS with a LF prototype extension on FFI's HUGIN autonomous underwater vehicle during ARISE'12.

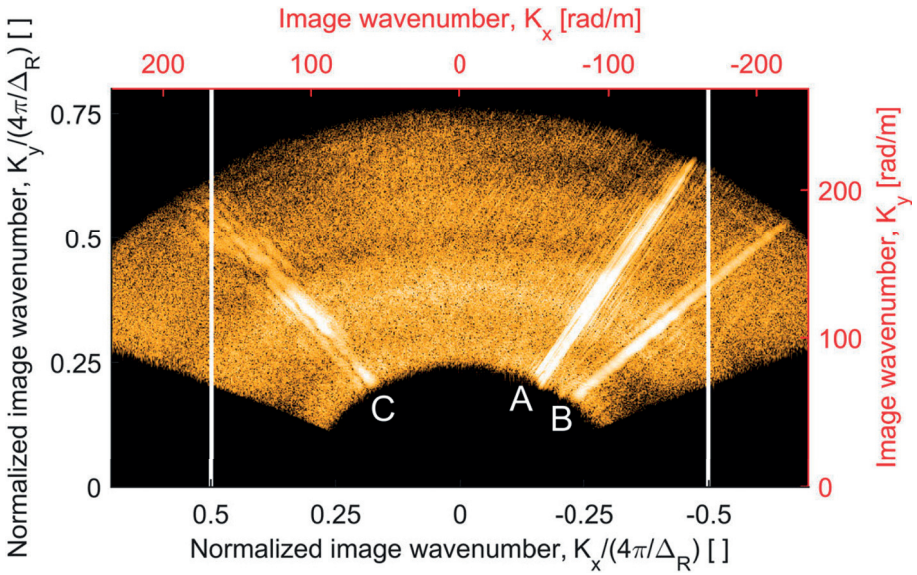

Figure II.4: Image wavenumber domain spectrum for the aperture used in the SAS image of Figure II.3. The vertical white lines roughly indicate the -3 dB bandwidth. We can relate the strong lines of the spectrum to specular reflections off the pipe (A), the lefthand side of the cube (B) and the righthand side of the cube (C).

We recognize the specular reflection off the pipe (A), the lefthand side of the cube (B) and the righthand side of the cube (C) in Figure II.3 as strong lines in the wavenumber spectrum, correspondingly labeled (A), (B) and (C) in Figure II.4. The image was formed in the ground range coordinate system $[x, y]$ and not in the slant range system $[x, \sqrt{y^2 + z^2}]$.

In order to support transition of the results to other systems, we have normalized the image wavenumber coordinates by $4\pi/\Delta_R$, where Δ_R is the receiver array element spacing. For dense receiver arrays with rectangular elements of size $d_R = \Delta_R$, this normalization is numerically identical to normalizing to half the full mainlobe width (i.e. half the null-to-null bandwidth). In addition to the normalized values (in black), we also give the numerical values for the system used (in red), as in Figure II.4.

II.3 Wideband Imaging Methods

In this section we present three algorithms for wideband SAS image formation.

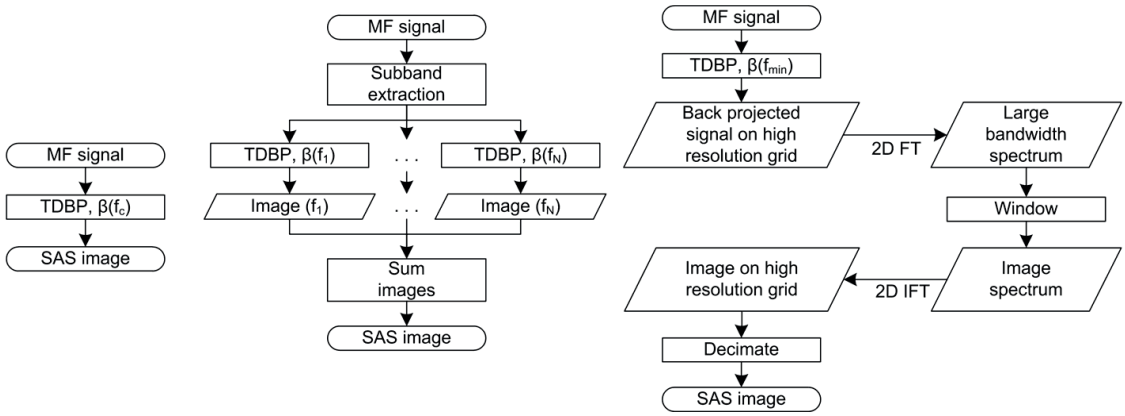

(a) BP (b) MBP (c) WBP

Figure II.5: Image formation processing flow for a) the standard Back Projection (BP) algorithm, using the same processing beamwidth β for the entire signal bandwidth, b) the Multiband Back Projection (MBP) algorithm, dividing the signal bandwidth into multiple subbands and using the standard back projection algorithm on each subband and c) the Wideband Back Projection (WBP) algorithm, performing frequency-dependent windowing in the wavenumber domain.

II.3.1 Back Projection (BP)

Standard BP image formation was outlined in Section II.2.1. The algorithm is illustrated schematically in Figure II.5a, and follows the formulation given in (II.2). We observe that the windowing is independent of frequency, as the weights w(θ) only change with look angle θ to the pixels from each element in the synthetic aperture. For comparison with the other algorithms, we adopt the

along-track wavenumber coverage at the center of the frequency band as the effective coverage, in a compromise between missed low frequency data and added high frequency data, c.f. Figure II.2, and obtain $\Delta K_{x_{eff}} \approx 2K(f_c)\sin(\beta/2)$.

II.3.2 Multiband Back Projection (MBP)

Multiband back projection is also known as the subband method or spectral decomposition (Châtillon et al., 1992),(Hayes et al., 1992). The idea of the multiband algorithm is to split the signal into multiple narrower bands in order to approach a more rectangular wavenumber coverage. The multiband back projection method can be expressed through (II.7), where N is the number of subbands, and $s_i(n, t, \boldsymbol{u}_i)$ and $\beta(n)$ are respectively the bandpass filtered data and the processing beamwidth for subband n.

$$h(\boldsymbol{x}) = \sum_{n=1}^{N} \frac{1}{\beta(n)} \sum_{i \in i_{\beta(n)}} \mathrm{w}(\theta(\boldsymbol{x}, \boldsymbol{u}_i)) s_i(n, t(\boldsymbol{x}, \boldsymbol{u}_i), \boldsymbol{u}_i) \Delta\theta(\boldsymbol{x}, \boldsymbol{u}_i). \tag{II.7}$$

In Figure II.5b we illustrate the processing flow of the multiband algorithm. After splitting the signal into multiple subbands, the standard BP algorithm is applied on each individual band, before the processed subband images are summed coherently to produce the MBP image. The multiband approach can introduce artifacts from merging the discrete bands, as a result of the irregular shape of their combined wavenumber domain coverage.

II.3.3 Wideband Back Projection (WBP)

Wideband back projection supports any wavenumber domain coverage, including rectangular. The approach is based on time domain back projection followed by wavenumber domain filtering (Synnes et al., 2013). It is thus a hybrid time/wavenumber domain approach.

We illustrate the main steps of the wideband algorithm in Figure II.5c. First, the signal is back projected using the maximum processing beamwidth imposed by the lowest frequency. We use a high resolution grid that meets the Nyquist criterion over the processed bandwidth and beamwidth, thus supporting a discrete Fourier transform into the image wavenumber domain. Here we apply the desired processing bandwidth by means of a windowing function. Then, returning to the spatial image domain (for numerical reasons only) we decimate the data in order to obtain the requested spatial grid of the final SAS image.

The approach can be described in a spatial (or time) domain representation through (II.8) for comparison with the other algorithms. We let $(*_{x,y})$ denote a 2D convolution along both the x- and y-axis. The back projected maximum beamwidth wideband signal is expressed in (II.10), and the processing beamwidth is defined through the wavenumber domain windowing function W of (II.9).

$$h(\boldsymbol{x}) = \mathrm{w}(\boldsymbol{x}) *_{x,y} h_0(\boldsymbol{x}), \tag{II.8}$$

where

$$\mathrm{w}(\boldsymbol{x}) = IFT_{2D}\{W(\boldsymbol{K})\} \tag{II.9}$$

and

$$h_0(\boldsymbol{x}) = \frac{1}{\beta(f_{min})} \sum_{i \in i_{\beta(f_{min})}} s_i(t(\boldsymbol{x}, \boldsymbol{u}_i))\Delta\theta(\boldsymbol{x}, \boldsymbol{u}_i). \tag{II.10}$$

The sampling requirement of the WBP algorithm follows from its maximum wavenumber coverage: The output image of the WBP algorithm ideally has the same along-track image wavenumber coverage, $\Delta K_{x_{image}}$, at all frequencies, representing a frequency-dependent processed beamwidth. While the largest beamwidth is required for populating the lowest frequency data only, all frequencies are populated with the back projection processing. As a result, the highest frequency data will span an along-track image wavenumber coverage of $\Delta K_{x_{Nyquist}} = \Delta K_{x_{image}} \frac{f_{max}}{f_{min}}$, and in order to avoid any aliasing, the sampling grid must support $\Delta K_{x_{Nyquist}}$. However, because wavenumbers outside $\Delta K_{x_{image}}$ is excluded from the output image, aliasing in that region does not affect the output image. As a result, the maximum along-track image wavenumber coverage required for the WBP algorithm is $\Delta K_{x_{WBP}} = \Delta K_{x_{image}} \frac{f_{max}+f_{min}}{2f_{min}}$. The corresponding cross-track image wavenumber coverage required for the WBP algorithm is $\Delta K_{y_{WBP}} = K(f_{max}) - K(f_{min})\cos(\beta(f_{min})/2) \lesssim K(f_{max})$. The related pixel spacing follows from the Fourier relation $[d_x, d_y] = [2\pi/\Delta K_x, 2\pi/\Delta K_y]$.

II.4 Performance Evaluation

We argue that the relative performance of the different algorithms for image formation cannot be established solely by evaluating the image quality of large bandwidth images. In particular, wideband and widebeam data fully contribute to improved resolution only where the scattering can be modeled by a point target at a fixed position, independent of frequency and aspect angle(Rihaczek et al., 1996). This criterion is typically not met for wideband widebeam systems, with frequency-dependent scattering and a higher potential of aspect-dependent occlusion. The full bandwidth and beamwidth is nontheless important for the analysis of frequency- and aspect-dependent scattering (Williams et al., 2010),(Synnes et al., 2015). Furthermore, any image will inevitably incorporate application-dependent design choices (Curlander et al., 1991, section 6.5) and of course also the scene contents. We suggest an approach for isolating the performance of the imaging algorithms from the impact of system and scene, thus providing the means to compare and evaluate the performance of the algorithms.

II.4.1 Spatial Domain Evaluation

As cited in Section II.1, the synthetic aperture literature typically uses resolution (mainlobe -3 dB width), peak sidelobe ratio, multiplicative noise ratio (from

multipaths, sidelobes and grating lobes), additive noise level and geometric distortion as primary image quality metrics. The relative importance of the image quality metrics strongly depends on the application. In particular, a compromise must be made between resolution and suppression of sidelobes and grating lobes.

We assume that additive noise, multipath and defocus/geometric distortion (from inaccurate assessment of navigation, medium and/or bathymetry) should have roughly the same impact on the investigated SAS imaging algorithms. However, the inherent windowing function of the imaging algorithms can have different impacts on resolution, peak sidelobe ratio and multiplicative noise ratio (from integrated sidelobe ratio and integrated grating lobe ratio). The latter metrics with potential of discriminating between the processing algorithms can all be derived from the point spread function (PSF), which depicts how a system reproduces a single point scatterer(Curlander et al., 1991, chapter 6.2).

Unfortunately, neither the point spread function, nor all of the image quality metrics can easily be computed from an image of opportunity. In SAR, evaluating the performance of a specific system typically involves imaging a strong point scatterer in order to obtain an estimate of the point spread function (Carrara et al., 1995, chapter 8.7). An indication of the performance for a specific system can also be obtained by simulating a point scatterer as seen through the system (Curlander et al., 1991, chapter 6.5). The performance of a specific system is determined by the system design and the processing choices, both ideally optimized for the systems' intended application.

II.4.2 Wavenumber Domain Evaluation

We choose to evaluate and compare the different algorithms for image formation in the wavenumber domain, with focus on the metrics that can be derived from the point spread functions. The wavenumber domain is chosen because the differences between the three algorithms are more naturally observed in this domain. We assess the data quality as a function of wavenumber, and rate the different algorithms by how well they target the data.

We divide the system point spread function into two wavenumber domain components, the *sensed spectrum* and the *windowing function* as illustrated in Figure II.6. The sensed spectrum represents the scattering coefficients of the scene in the wavenumber domain, filtered by the system response. The windowing function describes the $\boldsymbol{K}$-dependent weighting of the imaging algorithm, and determines the trade-off between resolution and contribution from background noise, sidelobes and grating lobes.

For simplicity, we assume that both the spectrum and the amplitude distribution of the real world scattering coefficients are homogeneous and thus can be ignored in the performance assessment. The remaining components are then the sensor

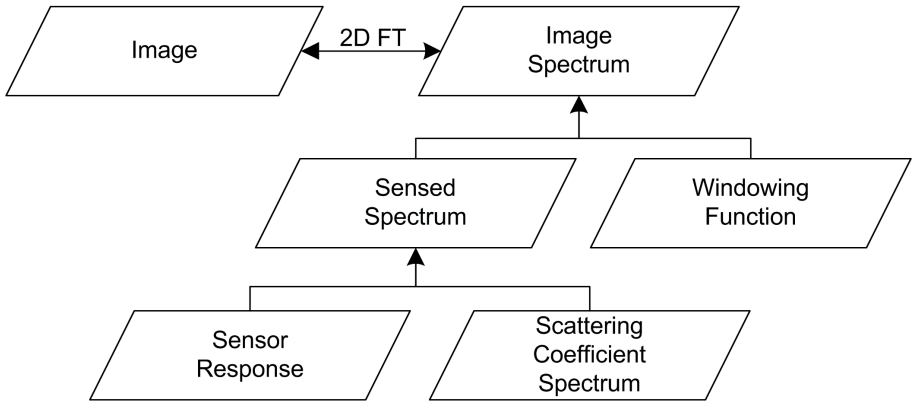

Figure II.6: Decomposition of the image data in the wavenumber domain. The point spread function is addressed when the imaged scene only contains a single point scatterer.

response and the windowing function, where the sensor response reflects the design choices, and the windowing function reflects the processing choices. Both should ideally be optimized for the application based on a set of performance metrics.

We choose to assess how SGR, SNR, resolution and sidelobe level depends on typical design choices and the image formation algorithms. The established way of evaluating the effect of different windowing functions is to start with measured or simulated data from a point scatterer, and for each candidate windowing function generate spatial domain images and estimate their quality metrics. In our complementary approach we emphasise how different factors affect the data quality by mapping the quality metrics SGR and SNR as function of image wavenumber $\boldsymbol{K}$. Based on these maps we analyse how each algorithm accesses data of different quality.

II.5 Wavenumber Domain Performance Metrics

We develop a set of wavenumber domain performance metrics and consider how the imaging algorithms access data of different quality over the wavenumber domain:

1. The shape and distribution of the weighting function $W(\boldsymbol{K})$ inherent to each imaging algorithms is mapped over the sensed spectrum as a function of $\boldsymbol{K}$.

2. The algorithm-independent properties of the weighting function $W(\boldsymbol{K})$ related to resolution, sidelobe level and homogeneity are treated separately.

3. The data quality is expressed through the SNR over the sensed spectrum as a function of $\boldsymbol{K}$.

4. The data quality is expressed through the SGR over the sensed spectrum as a function of $\boldsymbol{K}$.

II.5.1 Algorithm-Dependent Window Shape

The main differences between the output of the three evaluated algorithms for image formation are their inherent wavenumber domain window shapes and the coordinate along which the weights are applied. We illustrate the window shapes in Figure II.7 for each of the algorithms. The BP algorithm only supports weighting on the look angle θ. The weighting of the MBP algorithm is related to that of BP, but with weights determined independently for each frequency band. The WBP algorithm supports any windowing function, but we limit this study to functions on the along-track wavenumber, K_x. Processing a window covering half the zero-crossing beamwidth at all frequencies corresponds to a frequency-dependent beamwidth $\beta_{00/2}(f) = 2\sin^{-1}\left(\Delta K_{x,00/2}/2K\right) = 2\sin^{-1}\left(\lambda(f)/2d_R\right) \approx \lambda(f)/d_R$, where $\lambda = c/f$, and the approximation applies for $\lambda < d_R$.

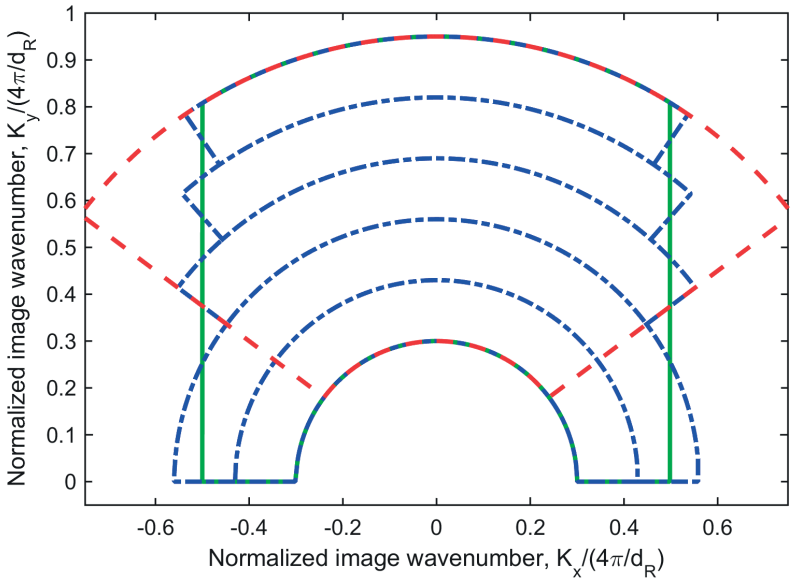

Figure II.7: Illustration of the image wavenumber coverage of three algorithms with cutoff at half the receiver element zero-crossing beamwidth (roughly the -3 dB beamwidth), evaluated at the center frequency of each band for a system with fractional bandwidth $B/f_c = 1$: BP algorithm (red), MBP algorithm (blue) and WBP algorithm (green).

II.5.2 Algorithm-Independent Weighting Function

Through the choice of weighting function, resolution and wavenumber coverage is traded for reduced grating lobe level and reduced sidelobe level (Carrara et al., 1995, chapter 8.3). In order to retain as much as possible of the information on the scene and also obtain the maximum resolution, the window should be as wide as possible while sustaining the required signal to noise level. In order to constrain the (integrated) sidelobe level, the window should have a smooth roundoff. In order to approach uniform sensitivity, the center of the window should be as flat as possible. This gives a set of conflicting requirements, and a compromise must be made based on the application.

In order to obtain valid estimates of the backscattering strength for all look angles, beampattern compensation should be incorporated into the weighting function.

II.5.3 Signal to Ambient Noise Ratio

Ambient noise limits the data quality, and can be expressed in the image wavenumber domain by the signal to ambient noise ratio as a function of image wavenumber.

The signal intensity over the image wavenumber is proportional to the element beampattern as a function of frequency. SAS elements are typically used over a wide range of frequencies and can often be represented by rectangular transducers with length d. The one-way amplitude response, A, of a rectangular element of length d is in the $[k_x, k]$-domain given by

$$A(k_x, k) = \begin{cases} |d|\mathrm{sinc}\left(\frac{k_x}{2\pi/d}\right) & k \in [k_{min}, k_{max}] \\ 0 & \text{otherwise} \end{cases}, \tag{II.11}$$

where sinc denotes the normalized sinc-function, while k_{min} and k_{max} are the lower and upper wavenumbers in the bandwidth. The combined transmitter/receiver response is proportional to the signal to ambient noise ratio with white isotropic noise, illustrated in the upper panel of Figure II.8 for the case of equally sized transmitter and receiver elements, $d_T = d_R$. In practice, the ambient noise spectrum in the 1-50 kHz band is better approximated by a $1/f$ amplitude dependence (Wenz, 1962), and the corresponding signal to ambient noise ratio is illustrated in the lower panel of Figure II.8. For a flat noise spectrum, the signal to ambient noise ratio is a function on K_x only, and the WBP algorithm would provide access to all data above a given quality. With $1/f$ noise, the signal to ambient noise ratio is not perfectly matched by the window function of neither the BP nor the WBP algorithm, but for large beamwidths the WBP algorithm provides a significantly better discrimination between high- and low quality data.

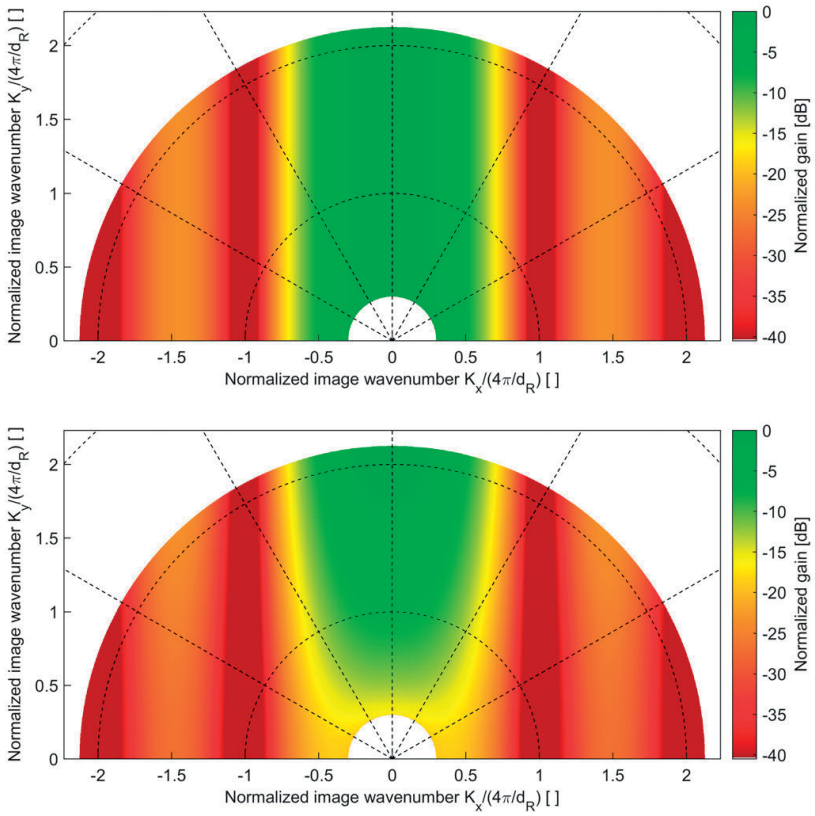

Figure II.8: Signal to ambient noise ratio assuming isotropic noise (upper panel) and assuming 1/f-amplitude noise (lower panel), both normalized to unity at broadside and for the maximum frequency. Equally sized rectangular transmitter and receiver elements, $d_T = d_R$, are assumed, and the illustrated image wavenumber support covers both LF and MF bands of the HISAS system.

II.5.4 Signal to Grating Lobe Ratio

SAS arrays are often under-sampled along-track in a compromise between coverage rate, complexity, cost and data quality. Under-sampling of the aperture will give rise to *grating lobes* (azimuth ambiguities / aliasing of energy) and degrade the SAS image quality(Curlander et al., 1991, chapter 6.5.1),(Rolt et al., 1992),(Moreira, 1993). When using multi-element receiver arrays, the receiver element spacing Δ_R is normally equal to the receiver element size d_R. In accordance with the Shannon Nyquist sampling theorem, these multi-element SAS systems are well-sampled only when $d_R = \Delta_R < \lambda_{min}/2$.

The response of the SAS aperture (including grating lobes) is expressed by its aperture function, and can be represented by the combined transmitter/receiver element beampattern, convolved by the synthesized receiver array positions (Rolt et al., 1992),(Moreira, 1993). The image wavenumber domain response of a sampling function with spacing Δ_R along x is a Dirac comb-function along

K_x with periodicity $\Delta_{K_x} = 2\Delta_{k_x} = 4\pi/\Delta_R$. When imaging a pixel, the entire Dirac comb-function is shifted, and contributions to grating lobes occur when the peaks of the Dirac-comb fall inside the sidelobes of the beampattern. Thus, for an under-sampled SAS array, $\Delta_R > \lambda_{min}/2$, and for the common case of element size $d_R = \Delta_R$, there are no grating lobes when processing broadside data only. However, the impact of grating lobes increases with increasing processing beamwidth, as off-broadside data is included (Rolt et al., 1992). This process is illustrated in Figure II.9, where the response of the sampling function, illustrated for processing broadside data, is overlaid on the combined transmitter/receiver beampattern for a system with $d_T = d_R = \Delta_R$. When processing off-broadside data the grating lobes no longer align with the nulls of the beampattern, and their impact increases. The angle of observation related to processing a specific image wavenumber $\boldsymbol{K}$ follows from (II.6). The beampattern at $|K_x| > K$ corresponds to evanescent waves that decay very rapidly. These are therefore neglected in the following.

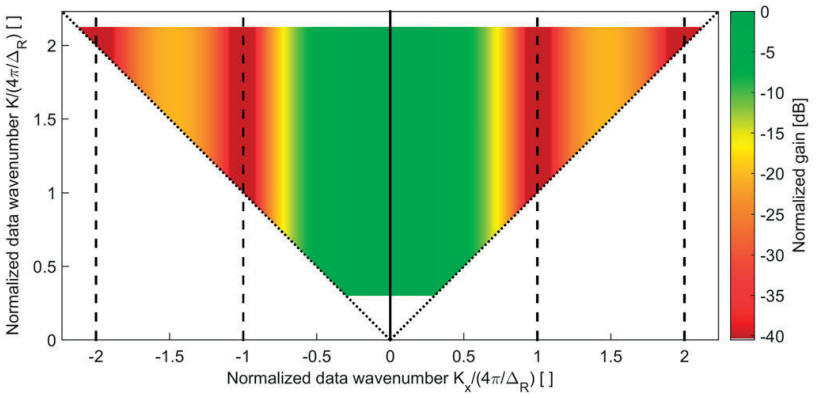

Figure II.9: Combined transmitter/receiver normalized gain along with the sampling function response corresponding to an infinitely long array with broadside steering. The image wavenumber spectrum will contain the sum of both the mainlobe value (solid line) and the grating lobe values (dashed lines). For off-broadside steering, both solid and dashed lines are shifted equally. The elements have been assumed rectangular with transmitter and receiver dimensions $d_R = d_T = \Delta_R$, where Δ_R is the element spacing. Non-propagating waves, outside the white lines are not shown. Note that the shown wavenumber coverage is in the $[K_x, K]$ coordinate system, and *not* in the $[K_x, K_y]$ coordinate system. This choice reflects the native coordinate system of the data recording, and thus the axis along which aliasing can originate. The illustrated wavenumber support covers both LF and MF bands of the HISAS system used in the examples.

Grating lobes affect the wavenumber spectrum in the $[K_x, K]$ coordinate system by replicating the spectrum of the scene at periodicity $4\pi/\Delta_R$ along K_x. The related image wavenumber spectrum in $[K_x, K_y]$ is obtained by applying the

Stolt transform (Carrara et al., 1995, chapter 10.2.3). For narrowbeam systems, $K_y \approx K$, and any grating lobes give object replica at a fixed spatial interval Δ_{x_G} along the x-axis for range r:

$$\Delta_{x_G} = r\lambda/\Delta_R. \tag{II.12}$$

A distortion of the targets are introduced as K_y diverts from K with increasing beamwidth. Regardless, for the case of wideband widebeam systems, a much stronger blurring is introduced from a large relative bandwidth. Both effects can be observed and inspected in the real data image wavenumber spectrum of Figure II.16, which is addressed in Section II.6.2.

How the impact of grating lobes is perceived depends on the application of the image; in particular whether we are interested in speckle or in persistent scatterers. These two cases correspond to studying signals with, respectively, zero or full correlation over the covered frequency and angular span. The degradation experienced for each case depends on the degree of defocus of the grating lobes. We simplify our analysis by limiting it to wideband widebeam systems with at least a few persistent scatterers distributed over the scene, such that the grating lobes are strongly defocused. We study the SGR for a speckle scene in detail, before we briefly address some modifications that apply with the introduction of persistent scatterers.

II.5.4.1 Speckle

For speckle the signal does not add up in phase over look angles and frequency span. The average spatial domain SGR corresponds to the integrated signal to integrated grating lobe ratio (ISIGR) in the wavenumber domain. This is given in (Curlander et al., 1991, chapter 6.5.1) through its reciprocal, the along-track ambiguity to signal ratio (AASR), assuming narrowband and homogeneous scattering distribution. This expression is extended to include weighting over the processing beamwidth in (Hawkins, 1996, chapter 5.2.1):

$$ISIGR(\Delta K_x, K_y) = \frac{\int\limits_{\Delta K_x} W(\boldsymbol{K}) S(\boldsymbol{K})\, dK_x}{\int\limits_{\Delta K_x} W(\boldsymbol{K}) G(\boldsymbol{K})\, dK_x}, \tag{II.13}$$

where

$$S(\boldsymbol{K}) = Z\left\{A^2(K_x, K)\right\} \tag{II.14}$$

and

$$G(\boldsymbol{K}) = Z\{\sum_{\substack{m=-\infty \\ m\neq 0}}^{\infty} A^2(K_x + m\frac{4\pi}{\Delta_R}, K)\} \tag{II.15}$$

are the signal energy and the grating lobe energy respectively, and $Z\{\cdot\}$ denotes the Stolt transform from $[K_x, K]$ to $[K_x, K_y] = \boldsymbol{K}$. Δ_{K_x} expresses the along-track processing bandwidth. The weighting $W(\boldsymbol{K})$ expresses the algorithm-dependent

window shape of Section II.5.1 for the chosen processing beamwidth or bandwidth and the weighting function of Section II.5.2 applied within the window. The weighting can optionally include beampattern compensation through a scaling by $1/S(\boldsymbol{K})$.

Equation (II.13) gives an average result over the processed wavenumber domain spectrum, and thus gives a data or system quality metric. We introduce a new means for analyzing the data quality by mapping and evaluating the signal to grating lobe ratio as function of image wavenumber,

$$SGR(\boldsymbol{K}) = \frac{S(\boldsymbol{K})}{G(\boldsymbol{K})}. \tag{II.16}$$

The SGR thus provides the quality of the added data from changing the processing beamwidth or the window shape.

In Figure II.10 we present the predicted SGR for a typical SAS design of a dense linear receiver array and equally sized transmitter and receiver elements. We observe that we have both a well-sampled and an under-sampled region. The well-sampled region covers the wavenumbers where the along-track array fulfills the Shannon-Nyquist sampling theorem, or $|\boldsymbol{K}|/(4\pi/\Delta_R) < 0.5$. Because we assume that there is no signal arriving from the backside of the array ($K_y < 0$ in the figures), there is a larger region with no aliasing, covering wavenumber vectors fulfilling $(|\boldsymbol{K}| + |K_x|)/(4\pi/\Delta_R) < 1$. For the under-sampled region, we observe that the SGR is a function of K_x only. Taking full advantage of all well-sampled data, together with the under-sampled data up to a given quality, would require a tailored 2D-windowing function.

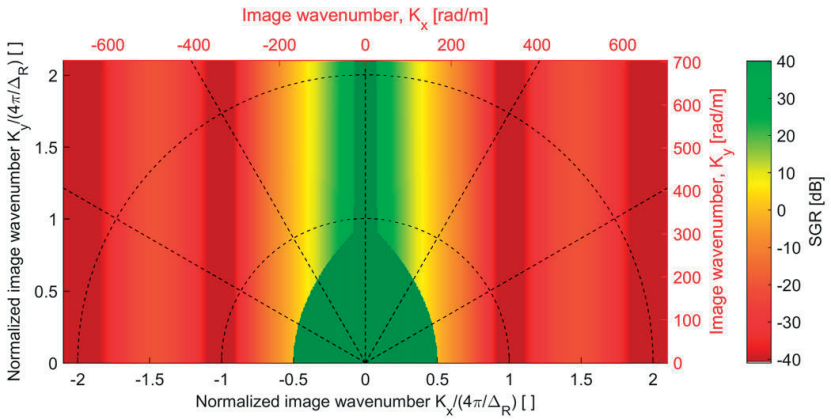

Figure II.10: Main lobe to grating lobe ratio for systems with $d_T = d_R = \Delta_R$.

II.5.4.2 Persistent scatterers

The findings of the previous section address incoherent scatterers. For persistent scatterers the signals add up in phase over look angles and frequency span, and

most targets of interest will be in phase over a span of look angles and frequencies. Assuming that the corresponding grating lobes are added out of phase, this will result in a significant increase of ISIGR versus that estimated for speckle, despite the wavenumber domain SGR being the same. As a consequence, targets might be observed in images also when zero or negative ISIGR is estimated for the speckle case (Curlander et al., 1991, Section 6.5.1).

II.6 Results and Discussion

We first present the predicted performance for a common but idealized SAS system design, and for two existing LF wideband SAS systems. For the existing systems we also include results on measured data for validation of the predicted performance.

Most SAS systems use a uniform linear array with along-track element size similar to the element spacing. These are typically under-sampled along-track for a portion of the frequency band, c.f. Section II.5.4. As a result, the impact of grating lobes is the main candidate for limiting the data quality. We therefore focus on mapping the SGR in the wavenumber domain, and perform the performance predictions for such a system. We also include performance predictions for simplified models of the HISAS with LF prototype extension, and from the MUD prototype SAS. We have also collected experimental data on these two SAS systems. These systems are shown in Figure II.11. Both systems are under-sampled for a portion of their frequency band, such that the data quality is limited by SGR off broadside also for the experimental systems.

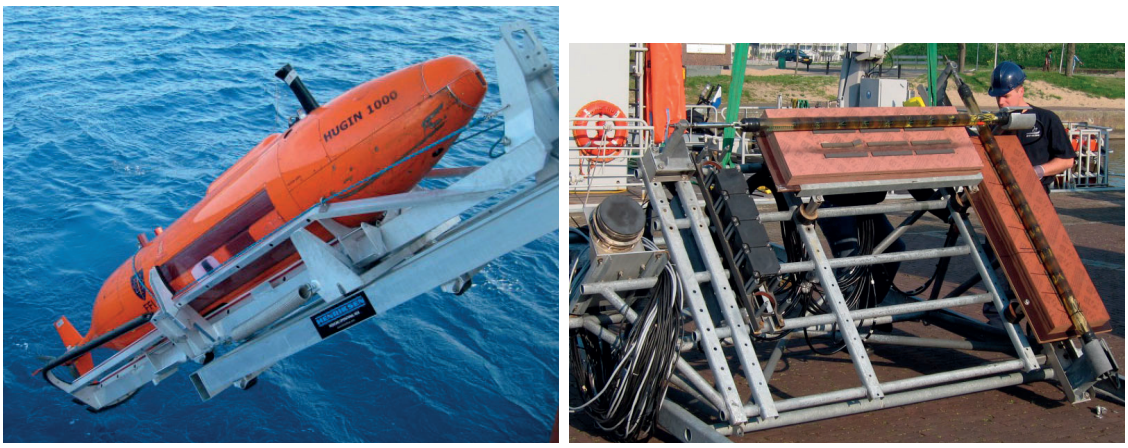

Figure II.11: Left: FFI's HUGIN HUS AUV carrying the HISAS system with prototype LF transmitter, during launch from CMRE's R/V Alliance. Right: TNO's MUD LF SAS prototype before operation from a diver support vessel of the Royal Netherlands Navy.

For the experimental data recordings, HISAS was operated from FFI's HUGIN

HUS autonomous underwater vehicle, and the datasets were collected during the ARISE'12 (Autonomous Reactive Intelligence Sea Experiment) organized by the NATO Centre for Maritime Research and Experimentation (CMRE) (Synnes et al., 2013). The LF band on HISAS spanned 12-38 kHz and was operated concurrently with a MF band spanning 60-85 kHz. We present theoretical predictions for the full band case and experimental results from the LF band. The experimental data from TNO's MUD LF SAS prototype were collected during the MUD-2011 sea trial in Haringvliet, where it was operated from a diver support ship of the Royal Netherlands Navy (Beckers et al., 2012). The system has three transducers, covering the frequency bands 1-4 kHz, 4-9 kHz and 11-26 kHz. The MUD system was designed as an interferometric SAS, with two along-track arrays that meet the Shannon-Nyquist sampling criterion below 11 kHz. Because of severe multipath at low frequencies in the 10-15 m water depth of the trial, data was also recorded with one of its receiver arrays mounted vertically. This allowed for better multipath suppression through vertical beamforming (Hunter et al., 2013). With the along-track array reduced to only one effective element, the data from the MUD system in the vertical configuration was under-sampled above 4 kHz. We present theoretical predictions for both configurations using the full band, but experimental results for the vertical configuration with transmission in the 4-9 kHz band only.

II.6.1 Theoretical Results on Wavenumber Domain Data Quality

We present the performance prediction on SGR for a uniform linear array with along-track element size similar to the element spacing in Figure II.10, where we include frequencies that cover the transition from a well-sampled to an under-sampled system. In Figure II.12, Figure II.13 and Figure II.14 we present the predicted SGR for our experimental systems, modeled by their corresponding transmitter length d_T, receiver length d_R and receiver spacing Δ_R, available from the figure captions. Figure II.12 corresponds to the HISAS LF and MF bands, Figure II.13 to MUD operated in the horizontal configuration for the frequency span 1-26 kHz, and Figure II.14 to MUD operated in the vertical configuration for the same frequency band.

We observe that the SGR for the experimental systems is in line with the predictions for the generalized system design of Figure II.10. To access all under-sampled data above a given SGR, together with all well-sampled data, would require a tailored 2D-window. In the under-sampled region, the SGR is a function on K_x only.

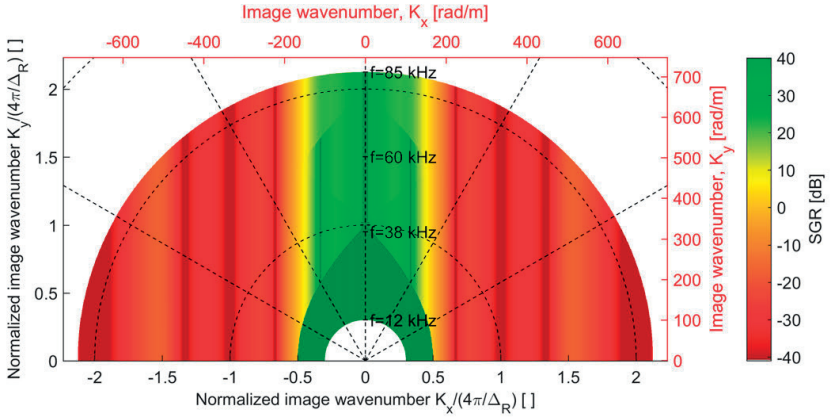

Figure II.12: Main lobe to grating lobe ratio corresponding to the HISAS with LF prototype extension, represented by $d_T 2/3 = d_R = \Delta_R = 3.75$ cm, and illustrated for the frequency interval 12-85 kHz, covering the LF (12-38 kHz) and MF (60-85 kHz) bands.

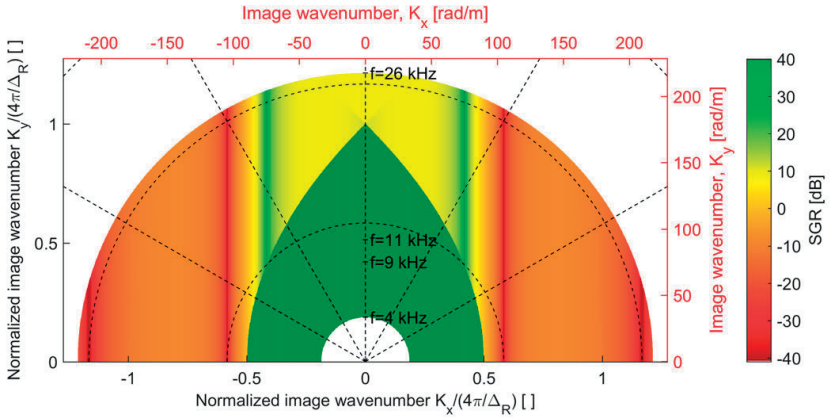

Figure II.13: Main lobe to grating lobe ratio corresponding to the MUD system in the horizontal configuration, represented by $d_T = 0.12$ m, $d_R \approx 0.03$ m, $\Delta_R = 0.07$ m, and illustrated for the frequency interval 4-26 kHz.

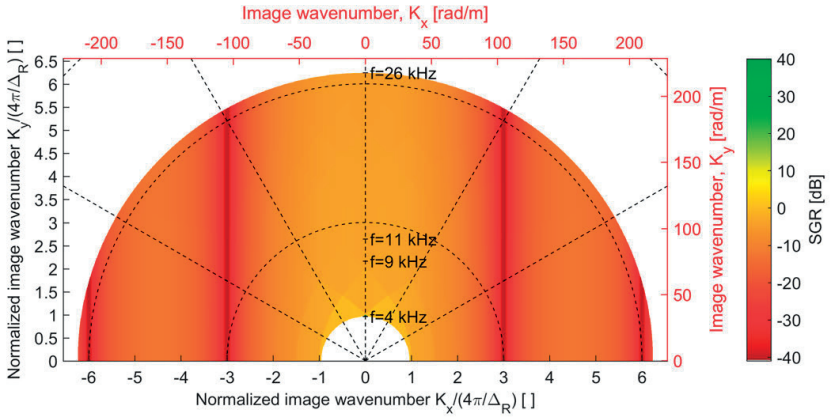

Figure II.14: Main lobe to grating lobe ratio corresponding to the MUD system in the vertical configuration, represented by $d_T = 0.12$ m, $d_R \approx 0.01$ m, $\Delta_R = 0.36$ m (effective multi-element receiver spacing), and illustrated for the frequency interval 4-26 kHz. The configuration provides a significantly lower grating lobe suppression than the design choice of the horizontal configuration. At the measurement site, multipath suppression showed to be of the utmost importance, and for this the vertical configuration was superior.

II.6.2 Experimental Validation of Wavenumber Domain Performance Evaluation

In the presented SAS images we compensate for the sensor beampattern and frequency response, before applying a tapered cosine window (Tukey window) with roundoff over a border covering 10% of the wavenumber domain area included for imaging.

In Figure II.3 we presented an example image from HISAS LF data showing a 1.2 m x 1.2 m concrete block next to a 0.9 m diameter pipeline. The bandwidth within $|K_x/(4\pi/\Delta R)| < 0.5$ was processed and is represented in the image. Some sidelobes can be observed as a result of the low sidelobe suppression of the tapered cosine window. Though the high frequency part of the scattering marked (B) is folded down into the image along-track bandwidth, any effect of folding is not easily observed.

Another example that shows the potential damaging effect of grating lobes on a wideband system is given in Figure II.15 and Figure II.16, using data from the LF band of the HISAS LF SAS prototype. The scene contains a pipeline with broadside at around 30 degrees azimuth. The collected image wavenumber data before windowing is presented in Figure II.16, and we observe that the strong scattering off the pipeline gives rise to a defocused grating lobe signal on the lower along-track wavenumbers. The upper and lower images in Figure II.15 have been formed from an along-track wavenumber interval of 0.5 normalized units width around $K_x/(4\pi/\Delta_R) = 0$ (broadside) and around $K_x/(4\pi/\Delta_R) = -0.5$ respectively. The grating lobe from the pipeline is clearly visible in the lower image, though not as a replica of the pipeline, but as a blurred feature distributed over a large area.

We also tried to illustrate the effect of grating lobes on a small reflector resembling a point scatterer and not a pipeline. This could have provided an estimate of the point spread function, and thus images from subsections of the image wavenumber domain should illustrate how the SGR change with $\boldsymbol{K}$. Due to the widebeam and wideband nature of the HISAS LF data, grating lobe smearing significantly lowers the peak level of the grating lobe contamination. So much so that we were unable to visualize grating lobe contaminations from weaker scattering targets, even those with target strength of up to 35 dB over the seafloor background.

In Figure II.17 we present an example image from MUD operated in the vertical configuration, depicting a deployed chain and a 1.5 m long epoxy-filled cylinder that are completely buried in a muddy seabed. Also here the bandwidth within $|K_x/(4\pi/\Delta R)| < 0.5$ was processed and is represented in the image. We do not present the wavenumber domain spectrum for this image, as it does not reveal any observable features. The predicted SGR was about 0 dB for this system in Figure II.14, but despite this we can still observe the chain and the cylinder at positions $[x, y] = [218\text{ m}, 42\text{ m}]$ and $[x, y] = [238\text{ m}, 44\text{ m}]$, respectively. This

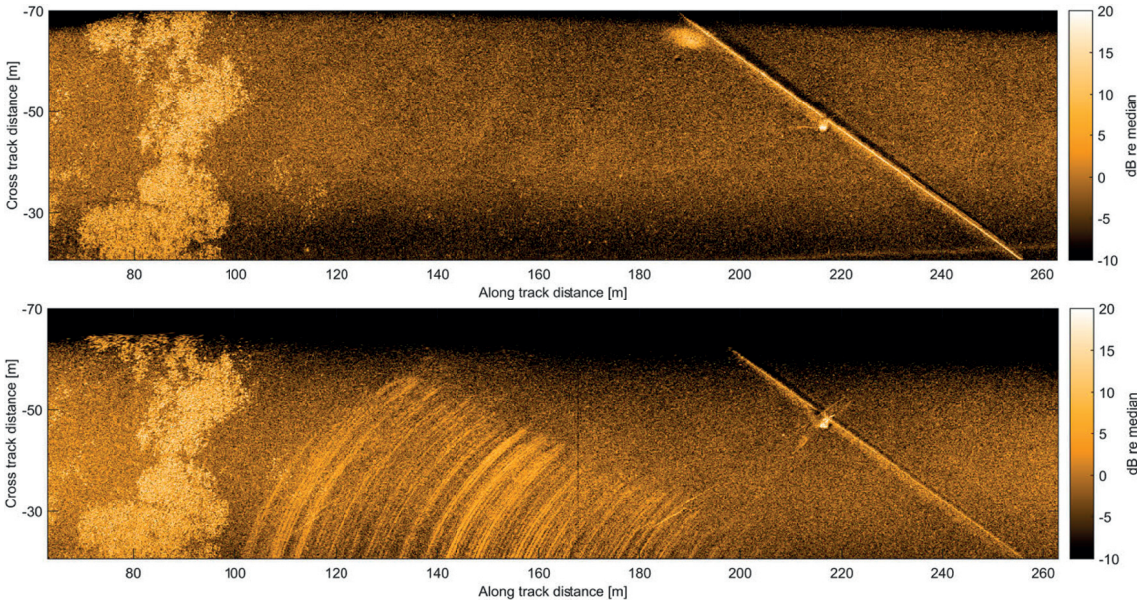

Figure II.15: SAS images from two different along-track processing bands on the same set of image wavenumber data, illustrated in Figure II.16. In the upper panel, we have processed an interval of $\Delta K_x/(4\pi/\Delta R) = 0.5$ centered on $K_x/(4\pi/\Delta R) = 0$, while in the lower panel, the same bandwidth was processed centered on $K_x/(4\pi/\Delta R) = -0.5$. The scene contains a pipeline with broadside at around 30 degrees and a concrete block, situated on a rather homogeneous seafloor with patches of Posedonia sea-grass on the left. The suboptimal lower image reveals a strong influence from grating lobes. The data were collected by HISAS with a LF prototype transmitter from the HUGIN HUS AUV during ARISE'12.

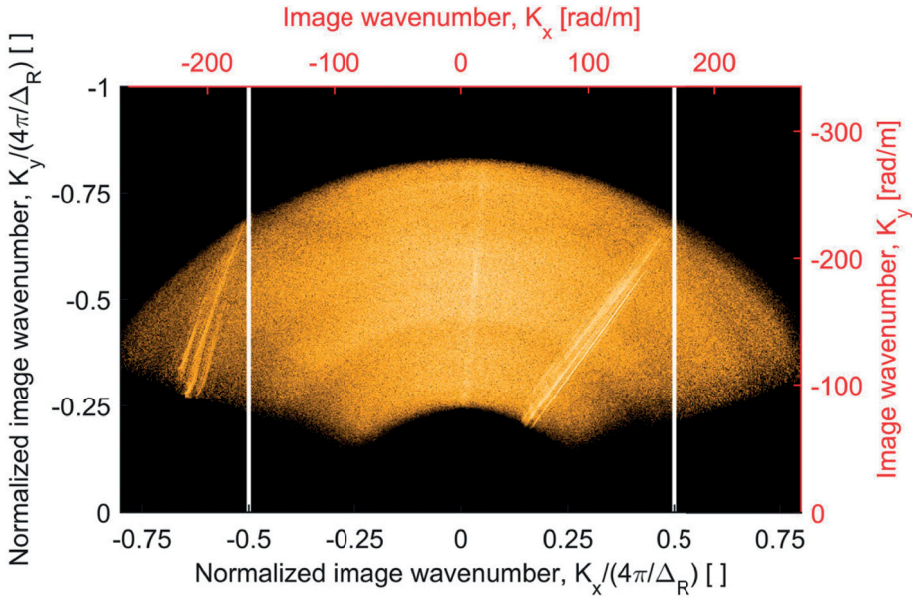

Figure II.16: The collected image wavenumber spectrum of the scene imaged in Figure II.15. The strong scattering off the pipeline around 30 degrees can be observed, along with its grating lobe replica distributed over the span from -30 to -60 degrees.

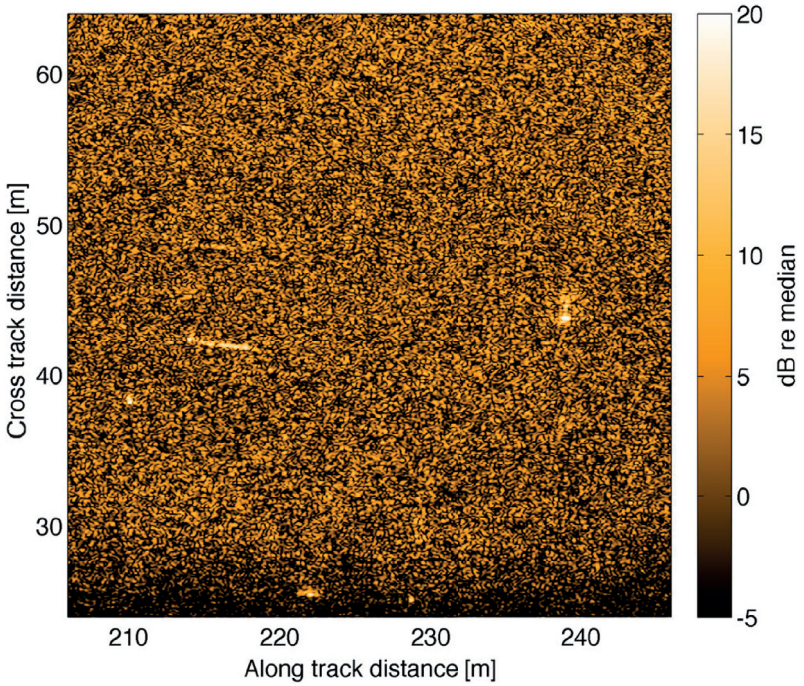

Figure II.17: Example image from MUD with sampling corresponding to Figure II.14. The image was formed using the WBP method on the interval $|K_x/(4\pi/\Delta R)| < 0.5$.

supports our suggestion that we can be able to observe (persistent) targets also when zero or negative SGR is predicted for the speckle case.

II.6.3 Theoretical Results on Full-Band Image Quality

The SGR averaged over the processed wavenumber domain spectrum gives an image quality metric, or a system quality metric regarding image generation. Whilst not the main thrust of this paper, the ISIGR metric from (II.13) gives insight into the various SAS systems used here. We present the ISIGR as a function of processing bandwidth for each system assuming a straightforward beampattern weighting. The results are given as a function of integration limit on K_x for the under-sampled region (or any $K_y/(4\pi/\Delta_R) > 1$), in Figure II.18, and for a region covering well-sampled data broadside out to $|K_x|/(4\pi/\Delta_R) \approx 0.3$, and under-sampled data further away from the broadside direction (that is $K_y/(4\pi/\Delta_R) \approx 2/3$), in Figure II.19.

As expected, we observe that the ISIGR is lower for the purely under-sampled case than for the case also covering well-sampled data. Numerical results for a few variations on the sensor design and processing widths are available in (Hawkins, 1996, Section 5.4.1) and (Barclay, 2007, Section 3.7.2).

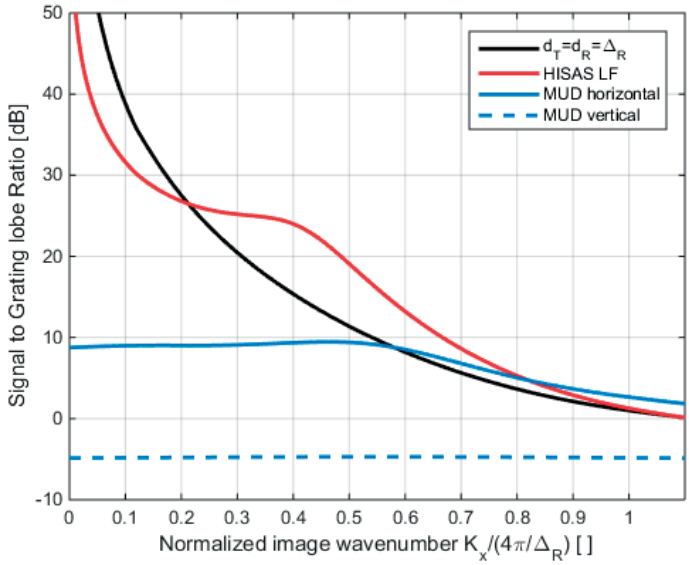

Figure II.18: Estimated spatial domain SGR on a speckle scene, using Eq. (II.13) evaluated in the under-sampled region as function of integration limit K_x. The different systems correspond to the sensor designs of Figure II.10 through Figure II.14, evaluated at any $K_y(4\pi/\Delta_R) > 1$. The only weighting applied is from the sensor beampattern.

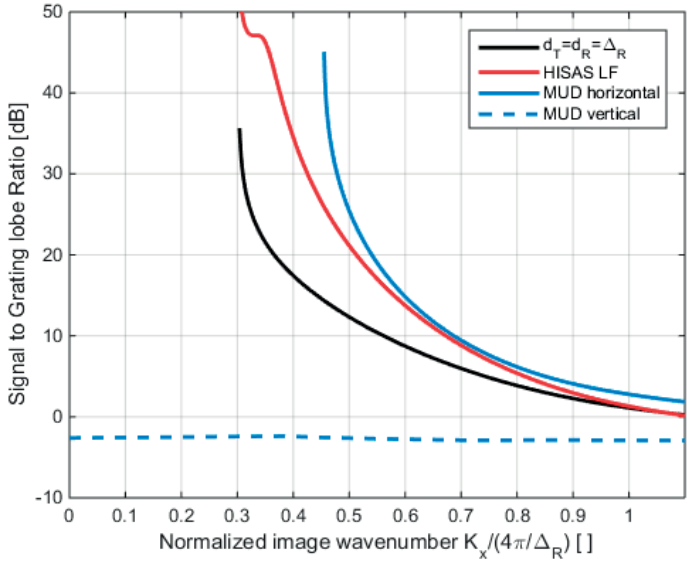

Figure II.19: Estimated spatial domain SGR on a speckle scene, using Eq. (II.13) evaluated at the center of the LF bands as function of integration limit K_x. For the theoretical system of $d_T = d_R = \Delta_R$, the SGR has been evaluated at $K_y/(4\pi/\Delta_R) \approx 2/3$ as for HISAS LF. For the other systems, the SGR have been evaluated at $K_y/(4\pi/\Delta_R) = \Delta_R/\lambda_{c_x}$, where λ_{c_x} is the observed wavelength at the center frequency projected onto the x-axis. The only weighting applied is from the sensor beampattern.

II.7 Conclusion

Wideband and widebeam systems provide information on the frequency- and aspect-dependence of the scattering. A starting point for extracting this frequency- and aspect-dependence is to form a SAS image product with maximum support of high-quality data. We have suggested a new approach for evaluating the quality of the collected data, where we map the quality of the collected data over the wavenumber domain in terms of both signal to ambient noise level and signal to grating lobe level. The signal to grating lobe level is the dominating term for typical SAS designs where the along-track aperture is under-sampled for a part of the frequency band. We have provided predictions on the wavenumber domain data quality both for a typical SAS design, and for two experimental systems. We have summarized three alternative methods of synthetic aperture sonar processing based on time domain back projection, and evaluated how they access data over the wavenumber domain. We observe that the wideband back projection (WBP) algorithm provides the maximum support of information on the frequency- and aspect-dependence over the scene, though to an additional computational cost. The added information does not necessarily lead to an improved quality of the corresponding spatial domain image.

Acknowledgements

The authors would like to thank the SAS development team at Kongsberg Maritime; Terje Gunnar Fossum, Johannes Martens Anderssen and Bjørnar Langli for excellent collaboration during the integration of the LF prototype extension to HISAS. We also thank the NATO Centre for Maritime Research and Experimentation (CMRE) for facilitating the ARISE'12 scientific measurement campaign where we participated with FFI's HUGIN HUS AUV.

References

Barclay, P. J. (2007). "Interferometric Synthetic Aperture Sonar Design and Performance". Ph.D. thesis. Christchurch, New Zealand: University of Canterbury, p. 203.

Beckers, G., Vossen, R. v., and Vlaming, G. (2012). "Low-Frequency Synthetic Aperture Sonar For Detecting Explosives in Harbors". In: *Sea Technology Magazine*, pp. 15–17.

Carrara, W. G., Goodman, R. S., and Majewski, R. M. (1995). *Spotlight Synthetic Aperture Radar: Signal Processing Algorithms*. Norwood, MA, USA: Artech House.

Châtillon, J., Adams, A. E., Lawlor, M. A., and Zakharia, M. E. (1999). "SAMI: A Low-Frequency Prototype for Mapping and Imaging of the Seabed by Means of Synthetic Aperture". In: *IEEE J. Ocean. Eng.* vol. 24, no. 1, pp. 4–15.

Châtillon, J., Bouhier, M.-E., and Zakharia, M. (1992). "Synthetic aperture sonar for seabed imaging: relative merits of narrow-band and wide-band approaches". In: *IEEE J. Ocean. Eng.* vol. 17, no. 1, pp. 95–105.

Christoff, J. T., Fernandez, J. E., and Cook, D. A. (2002). "Unmanned Underwater Vehicle Broadband Synthetic Aperture Sonar". In: *Proc. OCEANS'02 MTS/IEEE Conf.* Biloxi, Mississippi, pp. 1871–1877.

Cumming, I. G. and Wong, F. H. (2005). *Digital Processing of Synthetic Aperture Radar Data: Algorithms and Implementation*. Norwood, MA, USA: Artech House.

Curlander, J. C. and McDonough, R. N. (1991). *Synthetic Aperture Radar System and Signal Processing*. John Wiley & Sons, Inc, p. 647.

Ferguson, B. G. and Wyber, R. J. (2009). "Generalized Framework for Real Aperture, Synthetic Aperture, and Tomographic Sonar Imaging". In: *IEEE J. Ocean. Eng.* vol. 34, no. 3, pp. 225–238.

Franceschetti, G. and Lanari, R. (1999). *Synthetic Aperture Radar Processing*. New York, USA: CRC Press, p. 307.

Frey, O., Magnard, C., Rüegg, M., and Meier, E. (2009). "Focusing of Airborne Synthetic Aperture Radar Data From Highly Nonlinear Flight Tracks". In: *IEEE Trans. Geosci. Remote Sens.* vol. 47, no. 6, pp. 1844–1858.

Hansen, R. E. (2011). "Introduction to Synthetic Aperture Sonar". In: *Sonar Systems*. Ed. by Kolev, N. Z. [Online]. Available: http://www.intechopen.com/books/sonar-systems. Intech. Chap. 1, pp. 3–28.

Hansen, R. E., Callow, H. J., Sæbø, T. O., and Synnes, S. A. V. (2011). "Challenges in seafloor imaging and mapping with synthetic aperture sonar". In: *IEEE Transactions on Geoscience and Remote Sensing* vol. 49, no. 10, pp. 3677–3687.

Hawkins, D. W. (1996). "Synthetic Aperture Imaging Algorithms: with application to wide bandwidth sonar". Ph.D. thesis. Christchurch, New Zealand: University of Canterbury, p. 258.

Hayes, M. P. and Gough, P. T. (1992). "Broad-band Synthetic Aperture Sonar". In: *IEEE J. Ocean. Eng.* vol. 17, no. 1, pp. 80–94.

Hayes, M. P. and Gough, P. T. (2009). "Synthetic Aperture Sonar: A Review of Current Status". In: *IEEE J. Oceanic Eng.* vol. 34, no. 3, pp. 207–224.

Hunter, A., Vossen, R. van, Quesson, B., and Beckers, G. (2013). "Acoustic signatures of underwater UXO measured by low frequency broadband SAS". In: *Proc. 1st Int. Conf. and Exhib. on Underwater Acoustics (UA 2013)*. Corfu, Greece, pp. 865–872.

Hunter, A. J. and Vossen, R. v. (2014). "Sonar target enhancement by schrinkage of incoherent wavelet coefficients". In: *J. Acoust. Soc. Am.* vol. 135, no. 1, pp. 262–268.

Ishimaru, A. (1978). *Wave Propagation and Scattering in Random Media*. New York, NY, USA: Academic Press, p. 572.

Johnson, D. H. and Dudgeon, D. E. (1993). *Array Signal Processing: Concepts and Techniques*. Signal processing series. Englewood Cliffs, NJ, USA: Prentice Hall.

Madsen, S. (2001). “Motion compensation for ultra wide band SAR”. In: *IEEE Geoscience and Remote Sensing Symposium. IGARSS’01*. Vol. 3, pp. 1436–1438.

Moreira, A. (1993). “Suppressing the Azimuth Ambiguities in Synthetic Aperture Radar Images”. In: *IEEE Trans. Geosci. Remote Sens.* vol. 31, no. 4, pp. 885–895.

Nielsen, P. L., Hollett, R. D., Canepa, G., and Fox, W. L. J. (2013). “Unique low-frequency mine hunting and seabed characterization sonar”. In: *Proc. 1st Int. Conf. and Exhib. on Underwater Acoustics (UA 2013)*. Corfu, Greece, pp. 385–392.

Rihaczek, A. W. and Hershkowitz, S. J. (1996). “Man-Made Target Backscattering Behavior: Applicability of Conventional Radar Resolution Theory”. In: *IEEE Trans. Aerosp. and Electron. Syst.* vol. 32, no. 2, pp. 809–824.

Rolt, K. D. and Schmidt, H. (1992). “Azimuthal Ambiguities in Synthetic Aperture Sonar and Synthetic Aperture Radar Imagery”. In: *IEEE J. Ocean. Eng.* vol. 17, no. 1, pp. 73–79.

Schock, S. G., Tellier, A., Wulf, J., Sara, J., and Ericksen, M. (2001). “Buried object scanning sonar”. In: *IEEE J. Ocean. Eng.* vol. 26, no. 4, pp. 677–689.

Soumekh, M. (1994). *Fourier Array Imaging*. Englewood Cliffs, NJ, USA: Prentice Hall.

Soumekh, M. (1999). *Synthetic Aperture Radar Signal Processing*. New York, NY, USA: John Wiley & Sons.

Sternlicht, D. D., Fernandez, J. E., and Dr. Marston, T. M. (2013). “Advances in Synthetic Aperture Sonar Transform Mine Countermeasures and Undersea Warfare”. In: *CHIPS Magazine*. [Online]. Available: http://www.doncio.navy.mil/CHIPS.

Synnes, S. A. V. and Hansen, R. E. (2013). “Ultra wideband SAS imaging”. In: *Proceedings of the 1st Underwater Acoustics Conference and Exhibition (UACE)*. Corfu, Crete, Greece, pp. 111–118.

Synnes, S. A. V. and Hansen, R. E. (2015). “Aspect-dependent scattering in widebeam synthetic aperture sonar”. In: *Proceedings of the 3rd Underwater Acoustics Conference and Exhibition (UACE)*. Chania, Crete, Greece, pp. 129–136.

Wenz, G. M. (1962). “Acoustic ambient noise in the ocean: Spectra and sources”. In: *J. Acoust. Soc. Am.* vol. 34, no. 12, pp. 1936–56.

Williams, K. L., Kargl, S. G., Thorsos, E. I., Burnett, D. S., Lopes, J. L., Zampolli, M., and Marston, P. L. (2010). “Acoustic scattering from a solid aluminum cylinder in contact with a sand sediment: Measurements, modeling, and interpretation”. In: *The Journal of the Acoustical Society of America* vol. 127, no. 6, pp. 3356–3371.

Ødegård, Ø., Ludvigsen, M., and Lågstad, P. A. (2013). “Using Synthetic Aperture Sonar in Marine Archaeological Surveys - some first experiences”. In: *Proc. OCEANS’13 MTS/IEEE Conf.* Bergen, Norway.

Paper III

Aspect-Dependent Scattering in Widebeam Synthetic Aperture Sonar

Stig Asle Vaksvik Synnes, Roy Edgar Hansen

Published in *3rd Underwater Acoustics Conference and Exhibition (UACE)*, June 2015, Chania, Crete, Greece, pp. 129–136.

Abstract

Widebeam synthetic aperture sonar (SAS) gathers information on the acoustic scattering over a scene. From the aspect-dependent scattering of facets we can extract information on their orientation and size. This is information that can be useful in target detection and classification. Each pixel of a SAS amplitude image represents the backscattering at a given location. In SAS imaging the backscattering is normally assumed to be independent of look angle within the beamwidth. This assumption of aspect-independent scattering is only valid for narrowbeam systems. For widebeam systems the backscattering of real scatterers can show a strong angular dependency over the beamwidth. We suggest to extract this additional information, and investigate the aspect-dependency of the backscattering going into each pixel. We are able to estimate both the orientation of facets and their size. We demonstrate the method on SAS data recorded from a HUGIN autonomous underwater vehicle using a HISAS system with a prototype low frequency transmitter covering the band 12-38 kHz with a -3dB beamwidth exceeding 100 degrees at the center frequency. The approach is based on adaptive matched filter feature extraction developed in synthetic aperture radar (SAR).

III.1 Introduction

In synthetic aperture sonar (SAS) imaging algorithms, the backscattering is normally assumed to be independent of look angle. This assumption is usually

Synnes and Hansen are with the Norwegian Defence Research Establishment (FFI), Norway. Synnes is also pursuing a Ph.D. at the University of Oslo, Norway, where Hansen is adjunct associate professor.

not met when processing wide beamwidths. For example man-made objects with facets exhibit a strong aspect-dependent back-scattering, whereas other objects, such as small rocks, can reflect more like point-targets. This is the notion behind a series of feature-extraction and detection algorithms developed for synthetic aperture radar (SAR) (Rau et al., 2000, Section VII.C). We recognize the methods presented in (Allen et al., 1994), (Chaney et al., 1994) and (Allen et al., 1995) as the most fundamental of these. Rather than assuming isotropic backscattering during the imaging, they suggest to perform *adaptive matched filtering* in order to estimate size and orientation of the dominating scatterers (assumed planar) for each pixel, and they also build an *adaptive matched filter image*. The approach has been followed-up only to a small extent in SAR. Within SAS one related study extracts the dominating orientation and size, represented by coherence length of targets, though only on (simulated) target snippets and not individual pixel level data (Brown et al., 2014).

In this paper we focus on pixel level *feature extraction*. We suggest to use the features as *complementary information* to the original SAS image. One potential beneficial application is target recognition.

III.2 Method

The angular contribution to an image pixel is obtained by delaying the pulse compressed signal of each transmitter-receiver element along the aperture until they all focus onto the pixel. In traditional SAS imaging the contribution from each aperture element (all look angles) are then averaged to give the pixel intensity. In adaptive matched filter SAS imaging and feature extraction,we do matched filtering on this angular scattering information in place of summation.

We suggest an alternative approach for extracting the angular contribution of the scattering from a single look complex SAS image. The SAS image is transformed into the image wavenumber domain through a 2D Fourier transform, focused onto each pixel position, and the angular dependency of the scattering is extracted.

III.2.1 Example Image

We form the widebeam SAS image in accordance with the wideband back projection (WBP) approach of (Synnes et al., 2013)(Synnes et al., 2015). For demonstrating the approach, we choose the low frequency (LF) SAS image of Figure III.1. The image data was recorded using FFI's HUGIN-HUS autonomous underwater vehicle (AUV) outside Horten in 2012 using the HISAS synthetic aperture sonar with a prototype LF transmitter. The LF band covers 12-38 kHz and was recorded concurrently with a medium frequency (MF) band covering 60-85 kHz. The scene contains targets of opportunity at 70 m depth and approximately 50 m ground range.

We assure maximum *angular coverage* by addressing images with samples

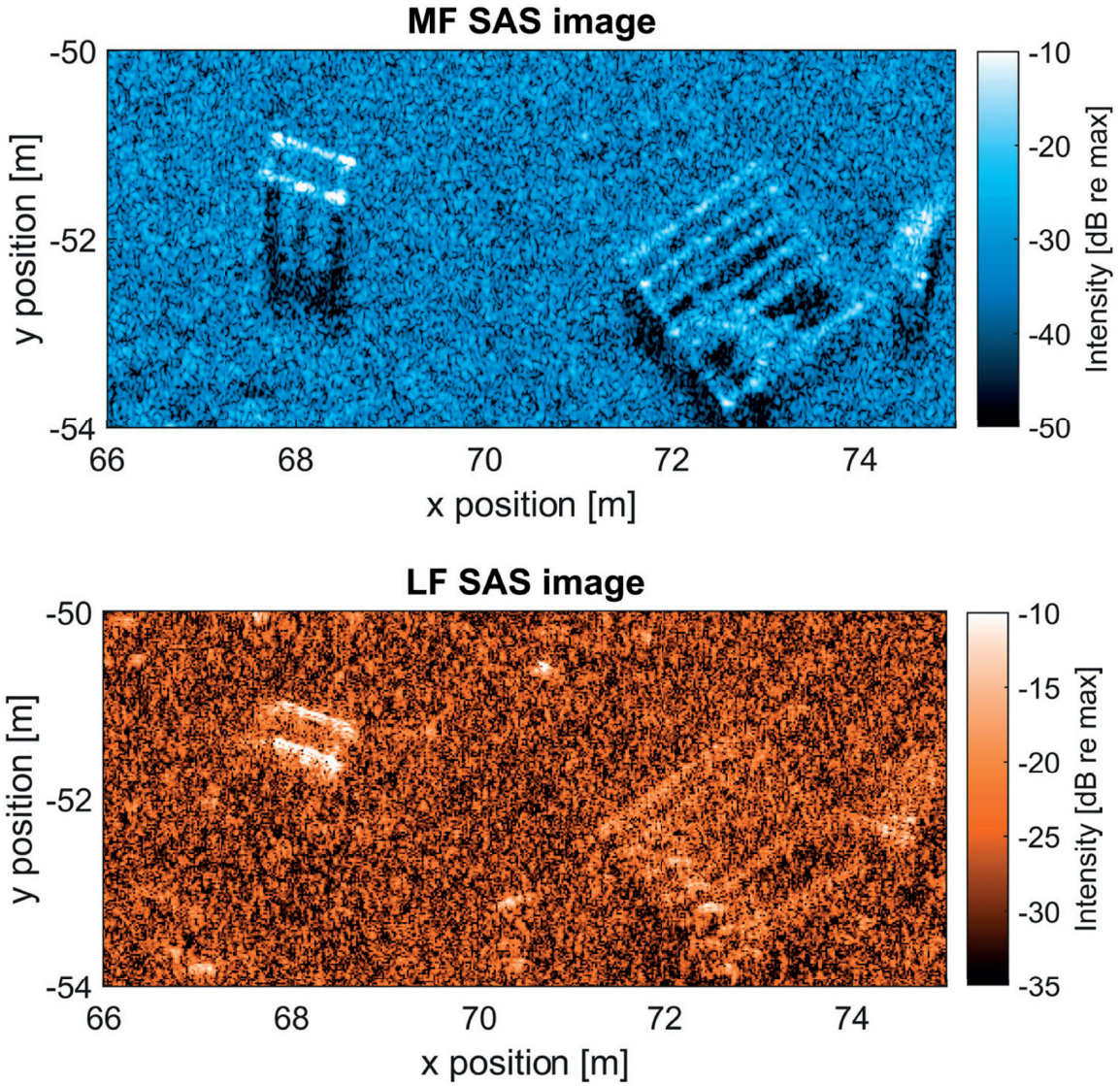

Figure III.1: SAS images of the example scene generated from concurrently recorded MF and LF data, using the HISAS 1030 on FFI's HUGIN HUS AUV with a LF prototype transmitter. The LF band spans 12-38 kHz with a center frequency beamwidth of 106 degrees, and the MF band spans 60-85 kHz with a center frequency beamwidth of 32 degrees.

evaluated at a spacing d_x equal to or smaller than that supported by our sensor and the image processing ($d_x = 2\pi/\Delta K_x \leq 2\pi/\Delta K_{x,max\_theo}$) (Synnes et al., 2015). We assure a good *angular resolution* by addressing images with hundreds of along-track samples, thus supporting the same number of image wavenumber bins.

III.2.2 Wavenumber Domain Focusing

We let h denote the SAS pixel value. Using the Matlab implementation of the Fourier transform, and ignoring the shift, we obtain:

$$H[\mu,\eta] = \sum_{m=1}^{M}\sum_{n=1}^{N} h[m,n]\cdot e^{-i2\pi(\mu-1)(m-1)/M}\cdot e^{-i2\pi(\eta-1)(n-1)/N}, \qquad \text{(III.1)}$$

where $m \in [1,M]$ and $\mu \in [1,M]$ address the along-track pixel number and image wavenumber component and $n \in [1,N]$ and $\eta \in [1,N]$ the corresponding across-track indices. The individual pixel values can be reconstructed using the inverse Fourier transform:

$$h[m,n] = \sum_{\mu=1}^{M}\sum_{\eta=1}^{N} \frac{H[\mu,\eta]}{MN}\cdot e^{i2\pi(\mu-1)(m-1)/M}\cdot e^{i2\pi(\eta-1)(n-1)/N}. \qquad \text{(III.2)}$$

The term inside the summations of (III.2) contains data from $H([\mu,\eta])$ focused onto image pixel $[m,n]$ and we denote these $F([\mu,\eta])|_{[m,n]}$.

In the above relations, the indices $[m,n]$ address the position $\vec{x} = (x[m], y[n])$, and the indices $[\mu,\eta]$ address the image wavenumber vector, $\vec{K} = (K_x[\mu], K_y[\eta])$. The Image wavenumber vector is related to the acoustic wavenumber vector $\vec{k}$ through the combined incident and reflected waves, $\vec{K} = \vec{k}_{re} - \vec{k}_{in}$. Thus we have $|\vec{K}| = 2|\vec{k}| \approx 4\pi/\lambda$, and $\angle\vec{K} = \arctan(K_x/K_y) = \theta$, where λ represents the wavelength and θ the look angle off broadside and defined positive counter-clockwise.

By collecting all the wavenumber domain components focused onto a single pixel before summation, we have decomposed the pixel contributions to individual frequencies and aspects. These data also contain information on all other pixels, but while these contributions are incoherent, the contribution for the pixel will be coherent over (nearby) aspects and frequencies. The approach can be summarized as follows:

$$\boxed{h(x,y) \rightarrow H(K_x,K_y) \rightarrow F(K_x,K_y)|_{(x_i,y_i)}}$$

Changing the focus point by similar approaches is also applied in fixed focusing for enhancement of shadows and elastic scattering (Groen et al., 2009)(Baik et al., 2011).

The image wavenumber domain intensity spectrum $|H(K_x,K_y)|$ of our example scene is shown in Figure III.2. By changing focusing point, the phase $\angle H(K_x,K_y)$ is altered while the intensity spectrum remains the same.

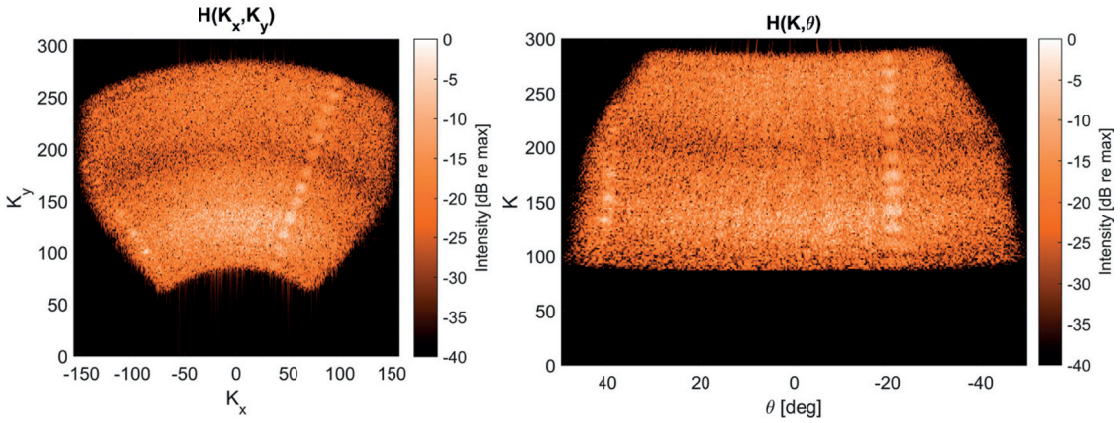

Figure III.2: Amplitude spectrum for the LF SAS image of FIG. III.1, represented as function of image wavenumber in Cartesian coordinates (left) and polar coordinates (right). The effective beamwidth is limited to 90 degrees due to limited recording range.

III.2.3 Matched Filtering

At each pixel location, the focused wavenumber domain data can be matched to candidate target responses with potentially better match than that of an isotropic scatterer. In (Allen et al., 1994), (Chaney et al., 1994) and (Allen et al., 1995), it is suggested to match-filter for linear (dihedral) targets of a few different lengths and many candidate orientations. We adopt their general approach, and extend it to cover the response of any linear scatterers (or rectangular facets), with length d and orientation (expressed by broadside direction) θ.

III.2.3.1 Uniform Linear Scatterer

The scattering response of a uniform linear scatterer resembles the beampattern of a uniform linear array. This is well known to be represented by a sinc-function. A linear scatterer with broadside at angle θ will give (a frequency-independent) maximum scattering for look angles of θ. In the image wavenumber domain, the scattering strength will change only with distance orthogonal to the line described by θ, and follow a sinc pattern. The -3 dB bandwidth ΔK_{-3dB} of the sinc-function follows from the length of the scatterer, D, as

$$\Delta K_{-3dB} \approx \Delta K_{00/2} = 2\pi/D, \tag{III.3}$$

where $\Delta K_{00/2}$ is half the zero-crossing bandwidth. This image wavenumber domain metric can be transformed to the beamwidth β at any frequency-dependent wavelength through

$$\beta = 2\arcsin(\lambda/2D). \tag{III.4}$$

In this study we ignore the full sinc beampattern and match to the scattering response described through its mainlobe only.

III.2.3.2 Orientation Estimation

The orientation of an uniform linear scatterer at position (x_i, y_i) can be found by locating the look angle with the maximum coherent signal. We address the image wavenumber domain spectrum $F(K_x, K_y)|_{(x_i,y_i)}$ and apply a Cartesian to polar transform (left to right panel in Figure III.2). Next we average over the K-axis to obtain the orientation dependency of the scattering $f(\theta)|_{(x_i,y_i)}$. The approach can be summarized as follows:

$$\boxed{F(K_x, K_y)|_{(x_i,y_i)} \rightarrow F(K, \theta)|_{(x_i,y_i)} \rightarrow f(\theta)|_{(x_i,y_i)}}$$

Next we examine the orientation dependency of the scattering in order to find the orientation of strongest coherent contribution. Example scattering distributions for different target positions and background positions are given in Figure III.3, with the obtained orientation at the peak of the coherent contribution and its -3 dB width indicated by blue circular marks.

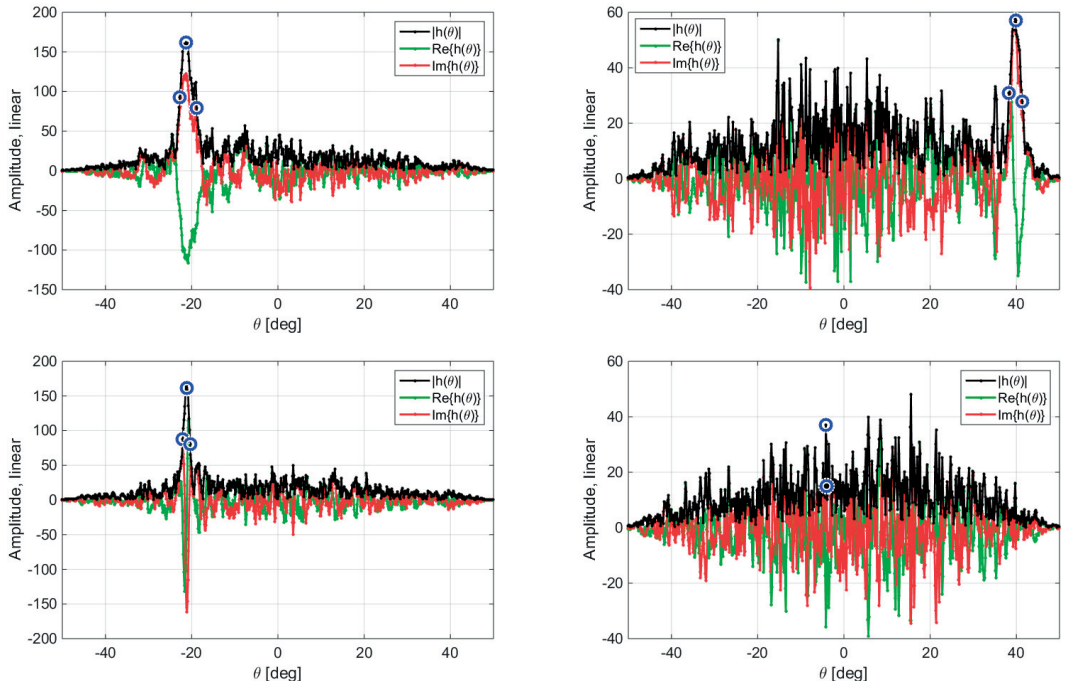

Figure III.3: $h(\theta)|_{(x,y)}$ for focusing on 4 different points in the scene, together with the related estimations of orientation and beamwidth, indicated by blue circles. Top left: point at center of strong scattering line on "box". Top right; point on "frame". Bottom left: in "sidelobe" outside strong scattering line on "box". Bottom right: random pixel on the background.

III.2.3.3 Length Estimation

The length of a scatterer is most accurately estimated through its scattering response by first rotating the focused image wavenumber domain spectrum to align with the look angle to the broadside orientation θ. The rotated data can be averaged along the direction expressed by θ, giving the wavenumber domain response along the orientation of the scatterer. From this we can estimate the scatterer length in accordance with equation (III.3). However, for now we approximate the result by investigating the coherent scattering contribution as function of orientation as derived earlier for the orientation estimate and illustrated in Figure III.3. We assume that the angular response corresponds to that of the center frequency and use (III.4) to estimate the scatterer length.

$$F(K_x, K_y)|_{(x_i,y_i)} \rightarrow F(\theta_o, \theta_{n_o})|_{(x_i,y_i)} \rightarrow f(\theta_{n_o})|_{(x_i,y_i)} \approx f(\theta)|_{(x_i,y_i)}$$

III.3 Results and Discussion

In Figure III.4 we present the estimated orientation and effective scatterer length for the sample scene, and also include the LF SAS image for reference. Both orientation and effective length is expressed through color coding. The orientation is represented in a linear scale over the covered look angles, but note that the effective length is represented in a logarithmic scale. The minimum effective length corresponds to using the full 3dB bandwidth supported by the system, while the maximum effective length corresponds to a mainlobe width of two samples, c.f. equation (III.3).

We observe that the estimates are quite consistent for the strong scatterers that can be observed in the SAS image. The estimated orientations of -21 degrees and 40 degrees for the two objects are correct. The effective length of the strong scattering lines to the left are estimated to between 0.9 and 1.4 m correspond roughly to the observed length of 0.8 m for the lines. The effective length for the object on the right is estimated to between 1.1 and 1.4 m, which is a bit shorter than the actual length of 1.7 m. We have not yet investigated on the origin of this discrepancy.

For positions with background only, the vast majority of the estimates give random orientations and rather long scattering lengths. This would correspond to choosing a narrow random peak of coherent signal contribution (as illustrated in the lower right panel of Figure III.3), and is expected. For positions on the background that are along a linear extension of a strong scatterer, the estimates of these scatterers appear to extend onto the background. More advanced estimation of orientation and effective length might avoid this artefact, and if not, a mask might be provided to present the valid measurements.

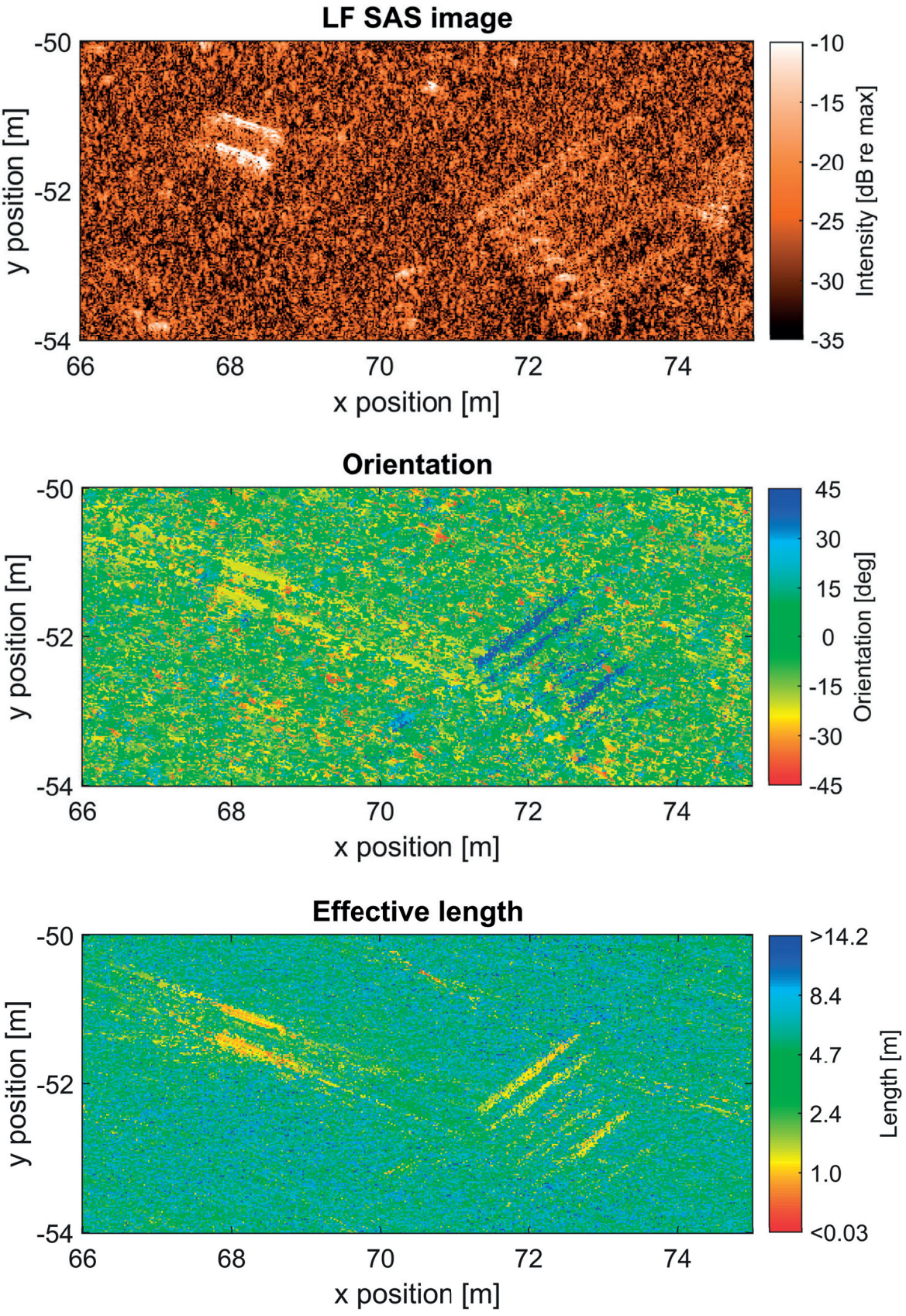

Figure III.4: The LF SAS image (top), together with the estimated orientation (center) and the estimated effective length (bottom).

III.4 Conclusion

Widebeam SAS gathers information on the aspect-dependency of the acoustic scattering. We have successfully demonstrated the estimation of orientation and effective length of facets, based on this aspect-dependent scattering represented in widebeam SAS images. In addition to providing orientation on facet orientation and length, the features can also support estimation of roughness and also be used for target segmentation.

Follow-up studies could investigate the effect of these new features on target detection and classification. Further studies could also investigate which related features can be extracted from a single pass when the specular reflection is not recorded, as with more narrowbeam (high frequency) SAS.

Acknowledgements

Thanks to Marc Geilhufe and Torstein Sœbø at FFI and Andreas Austeng at UiO for good feedback during the preparation of this paper.

References

Allen, M. R., Jauregui, J. M., and Hoff, L. E. (1995). "FOPEN-SAR detection by direct use of simple scattering physics". In: *Proc. SPIE 2487*, pp. 45–55.

Allen, M. R., Phillips, S. A., and Sofianos, D. J. (1994). "Wide-angle SAR matched filter image formation for enhanced detection performance". In: *SPIE 2093, Substance Identification Analytics*. Innsbruck, Austria, pp. 381–387.

Baik, K., Dudley, C., and Marston, P. L. (2011). "Acoustic quasi-holographic images of scattering by vertical cylinders from one-dimensional bistatic scans". In: *J. Acoust. Soc. Am.* vol. 130, no. 6, pp. 3838–3851.

Brown, D. C., Lyons, A. P., and Cook, D. A. (2014). "Spatial coherence theory and its application to synthetic aperture systems". In: *SASSAR 2014, Institute of Acoustics Proceedings*. Vol. 36, pp. 104–111.

Chaney, R. D., Willsky, A. S., and Novak, L. M. (1994). "Coherent aspect-dependent SAR image formation". In: *Proc. SPIE 2230*, pp. 256–274.

Groen, J., Hansen, R. E., Callow, H. J., Sabel, J. C., and Sæbø, T. O. (2009). "Shadow enhancement in synthetic aperture sonar using fixed focusing". In: vol. 34, no. 3, pp. 269–284.

Rau, R. and McClellan, J. H. (2000). "Analytic models and postprocessing techniques for UWB SAR". In: *IEEE Trans. Aerosp. and Electron. Syst.* vol. 36, no. 4, pp. 1058–1074.

Synnes, S. A. V., Hunter, A. J., Hansen, R. E., Sæbø, T. O., Callow, H. J., Vossen, R. van, and Austeng, A. (2015). "Wideband synthetic aperture sonar image formation and performance analysis". In: *To be submitted to IEEE Journal of Oceanic Engineering*.

Synnes, S. A. V. and Hansen, R. E. (2013). "Ultra wideband SAS imaging". In: *Proceedings of the 1st Underwater Acoustics Conference and Exhibition (UACE)*. Corfu, Crete, Greece, pp. 111–118.

Paper IV

Calibration Target for Estimation of Frequency Dependence in Synthetic Aperture Sonar

Stig Asle Vaksvik Synnes, Ole Jacob Lorentzen

Published in *5th Underwater Acoustics Conference and Exhibition (UACE)*, July 2019, Hersonissos, Crete, Greece, pp. 147–154.

Abstract

Synthetic aperture sonar (SAS) can provide high resolution images of the seafloor backscatter. A current research topic is whether wider bandwidth and lower frequencies can support better discrimination of different materials. In principle, the frequency dependence of the backscatter can be estimated at high resolution over the image. We suggest a calibration target that can provide simultaneous ground truth on both strength and frequency dependence of the backscatter.

We develop an extended target consisting of objects with different combinations of scattering strength and frequency dependence. In order to provide deterministic frequency dependencies, we use solid geometrical shapes in the form of spheres, cylinders/cones and corners as reflectors. The scattering strengths of these reflectors are functions of frequency to the power of 0, 1 and 2, respectively. These three frequency dependencies are combined with different scattering strengths by using replicas of different sizes. We try to limit the acoustic footprint of the targets to a point where possible, in order to support processing at the maximum SAS resolution. We mount the objects on a metal plate, and elaborate on the choice of material and thickness needed to provide the required acoustic properties at the frequencies under investigation.

Finally, we present SAS images of a prototype target measured both at and outside of the design frequency. The suggested calibration target should

Both authors are with the Norwegian Defence Research Establishment (FFI), Norway. Both authors are also pursuing their Ph.D. at the University of Oslo, Norway.

be well suited to validate algorithms extracting the frequency dependence, and their ability to isolate the frequency dependence from the scattering strength.

IV.1 Introduction

Synthetic aperture sonar (SAS) has become a major success for seafloor surveillance, providing high resolution images with large area coverage. Its applications are wide and include, but is not limited to, naval mine hunting, searching for wrecks, mapping of dumped WWII conventional and chemical munitions, underwater archeology, pipeline inspection and mapping for oil rig decommissioning (Hansen et al., 2019; Neto et al., 2017; Ødegård et al., 2018).

A current trend in SAS research is to investigate the added value of wider bandwidth and lower frequency, as these have the potential of supporting better discrimination of different materials, thereby improving the performance for many applications (Hansen, 2013).

At FFI we have been developing an algorithm to extract the frequency dependence of the scattering at high resolution over a SAS image. When testing the algorithm, we observed that the estimated frequency dependence increases with the estimated scattering strength. The correlation was not expected and could indicate an error in the algorithm. We therefore are in need of a calibration and validation target, that contains different combinations of scattering strength and its frequency derivative.

In this paper we develop a SAS target that allows for validating methods and algorithms designed to extract the frequency dependence of the acoustic scattering, and to isolate frequency dependence from scattering strength.

IV.2 Method

We suggest and develop a calibration target consisting of reflectors with different combinations of frequency dependence and scattering strength. It would be hard to find materials with the same scattering strength or frequency dependence over a wide frequency area. We therefore opt for using targets of simple geometrical shapes that provide different frequency dependencies. In order to support high resolution SAS, we also choose scatterers with a single point acoustic footprint where possible.

We choose to arrange the reflectors in a matrix pattern, such that row number reflects the intensity and the column number reflects the frequency dependence. Thus the calibration target can be used to validate estimation of both intensity and frequency dependence, in the presence of variations on the other.

We choose to mount the targets on top of a smooth metal plate, that is thick

enough that the reflection off the seafloor is minimal. This will make it possible to isolate also weaker scatterers, in contrast to mounting the targets on a frame where they would be observed on top of the seafloor scattering.

IV.2.1 Frequency Dependent Scattering with Geometrical Shapes

In order to provide deterministic frequency dependencies, we use solid geometrical shapes in the form of spheres, cylinders/cones and corners as reflectors. The scattering strength of geometrical shapes can be estimated directly from the geometry when the target dimensions are much larger than the wavelength. At wavelength λ the target cross section is $\sigma = 4\pi A^2/\lambda^2$, where A is the effective area (of a flat plate with the same scattering strength) and the scattering strength in dB re 1m follows as $TS = 10\log(\sigma/4\pi)$ (Lurton, 2010, Sec 3.2).

We have examined the list of reflectors in (Gallman, 2005) and focus on the few listed in Table IV.1. We observe that the scattering strength of these reflectors is a function of frequency to the power of 0, 1 and 2, depending on whether they are curved around two, one or no axes, respectively. Trihedrals provide single point acoustic footprint, as does the bicone when observed from its symmetry plane. The maximum scattering strengths for the shapes are listed in Table IV.1. For simplicity of predicting the targets' scattering cross sections, we assume small grazing angles and choose targets of scattering strengths $0.01\,\mathrm{m}^2$, $0.1\,\mathrm{m}^2$ and $1.0\,\mathrm{m}^2$.

Mirrored Shape	**Scattering Cross Section**
Half Sphere	πr^2
Cylinder	$4\pi r h^2/\lambda$
Balancing Cone	$16\pi r^3/(9\lambda)$
Triangular Trihedral	$8\pi h^4/\lambda^2$

Table IV.1: Maximum scattering cross section σ for geometrical shapes mounted on a reflecting infinite plane and observed at low grazing angles. The arguments are target radius r and height h, and the acoustic wavelength λ. The frequency dependence follows from $\lambda = c/f$, with sound speed c and frequency$f$. The formulas were derived from (Gallman, 2005, Chapter 6) and (Doerry et al., 2009).

IV.2.2 Plate Thickness

We would like the plate to provide a no-return area, masking the seafloor reflection, such that the object return is clean. This can be obtained by a low transmission through the plate for relevant seafloor grazing angles. For SAS, typical grazing angles are between 5 and 40 degrees.

Formulas for predicting the reflection and transmission off metal plates suspended in water are derived in (Fiorito et al., 1979). For plates described through their dilational and shear wave speeds, along with density and thickness, sample

predictions of reflection and transmission are showed in Figure IV.1. For a given

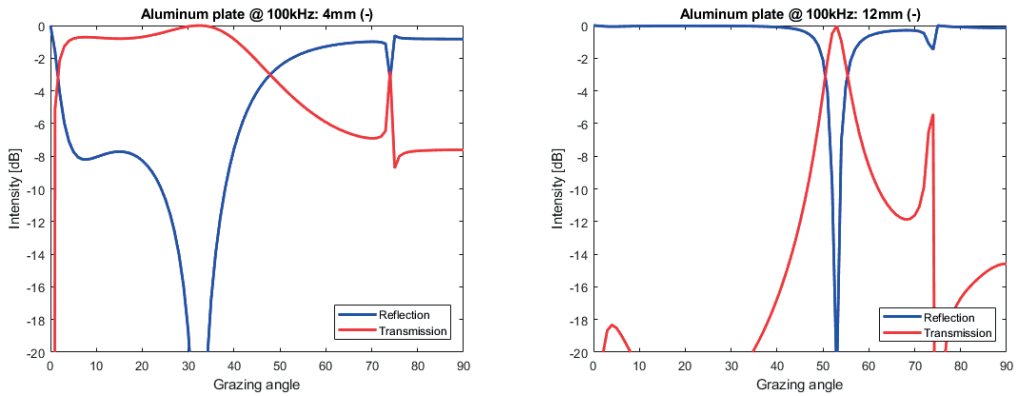

Figure IV.1: Reflected and transmitted energy off 4 mm and 12 mm thick aluminum plates at 100 kHz, predicted from (Fiorito et al., 1979).

material, the prediction can be transferred to another sensing frequency or plate thickness by keeping the product of frequency and thickness fixed. We find that for grazing angles below 30-40 degrees, aluminum plates provide *two-way transmission loss* at 100 kHz of around 2dB@4mm, 20dB@8mm, 40dB@12mm and 60dB@16mm plate thickness. For steel plates, the corresponding *two-way transmission loss* at 100 kHz is around 4dB@4mm, 20dB@6mm and 40dB@8mm. Steel has roughly three times the density of aluminum, with 7820 $\mathrm{kg/m^3}$ versus 2700 $\mathrm{kg/m^3}$.

If we have strong reflection off the plane at near normal incidence, the bicone target can be simplified by using a single standing cone, mirrored on the plate. In order to construct the trihedral corner reflector from plates, we depend on strong scattering for any incident angle. We observe that both for aluminum and for stainless steel, the intensity loss for the reflected signal at 100 kHz is smaller than 1 dB from grazing angles above 60 degrees. There is, however, a strong intensity loss around 45-55 degrees for both materials and most plate thicknesses. As a result, corners made of metal plates will not provide the desired scattering strength.

IV.3 Experimental Results

We present SAS images of a prototype calibration target that was made before our knowledge on plate reflection and transmission was gathered. This target was first measured in the spring of 2017 during FFI's MAREX'17 marine robotics exercise, using the HISAS 1032 SAS of FFI's HUGIN-HUS autonomous underwater vehicle (AUV). The system was operated with 30 kHz bandwidth around 100 kHz. After examining the results and observing that the target was barely visible, we acquired the mentioned knowledge on plate reflection and transmission, and found that our prototype should work more as intended at higher frequencies.

At the time, Kongsberg Maritime was developing their new HISAS 2040 SAS for operation from their new MUNIN AUV and from the Hydroid REMUS 600 AUV (*MUNIN AUV* accessed April 11, 2019). During the testing of their first MUNIN AUV around the summer of 2018, Kongsberg Maritime accepted to both deploy our target and record a few lines past it. The onboard HISAS 2040 system operated with 60 kHz bandwidth around 250 kHz. However, as the deployment of the plate was challenging, we only have recordings of the plate upside-down and standing-on-the-edge. Though these data cannot be used for calibration, they still prove useful for evaluating the design of the prototype calibration target and as benchmark for the theory as reported here.

IV.3.1 Prototype Calibration Target

We present a photo of our prototype target in Figure IV.2. Note that this target was made before the knowledge on plate reflection and transmission was acquired, based on the assumption that the mounting plate would allow only minimal transmission. The target measures 1.8 by 1.2 m, and the mounting plate is made of 4 mm aluminum. The distance between objects with the same scattering cross section is 0.6 m, and the distance between lines of different scattering cross section is 0.3 m. The solid shapes are made of aluminum, and the trihedral corner reflectors of 1.5 mm acid-resistant steel. On the far right corner, there is a 35 cm long cylinder holding an acoustic transponder used for positioning.

Figure IV.2: Photo of the prototype target before deployment. Photo: Kongsberg Maritime.

IV.3.2 Measurements at 100 kHz

In the 100 kHz SAS images, the plate appears transparent, but the edges normal to the line of sight can be made out. With the geometry of the plate known, also the transponder position can be discriminated, and at low grazing angles

also some of the stronger scatterers. It was confirmed by optical images that the target plate rests on a flat seafloor with the targets facing up.

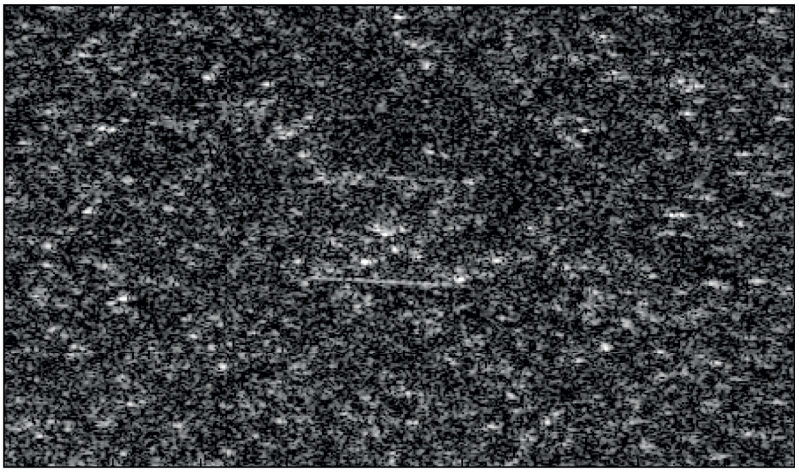

Figure IV.3: SAS intensity image measured at 85-115 kHz with HISAS1032 from the HUGIN-HUS AUV. The image shows a 9 m x 5 m area covering plate and was recorded at 60 m distance and 10 m altitude.

IV.3.3 Measurements at 250 kHz "upside-down"

The two SAS images of Figure IV.4, recorded around 250 kHz from a HISAS 2040 on a MUNIN AUV, shows the target plate observed from two opposite directions. The images strongly indicate that the target plate is deployed upside-down, resting on the 35 cm long cylinder and the opposite short edge of the plate. The two SAS images shows the target plate observed from two opposite directions.

In the left image both the down-facing side of the plate with the reflectors and the seafloor beneath the plate are illuminated. The target intensities increase with the modeled target scattering strength. However, as the corner reflectors are illuminated normal to one of the cross-plates, a strong specular scattering occurs. Also, as the seafloor scattering is overlaid on the target scatterers, the weakest of the targets cannot be isolated from the background.

The right image shows the up-facing (rather smooth) back-side of the plate. The corner reflectors are clearly outlined, which is consistent with the fact that only these scatterers protrude through the plate. Some of the scatterers with low cross section are also more prominent than those of higher cross section, indicating that the target shapes closer to the edge could by partly insonified. We observe that there is a shadow beneath and behind the plate. The shadow is more filled-inn closer to the resting face of the plate.

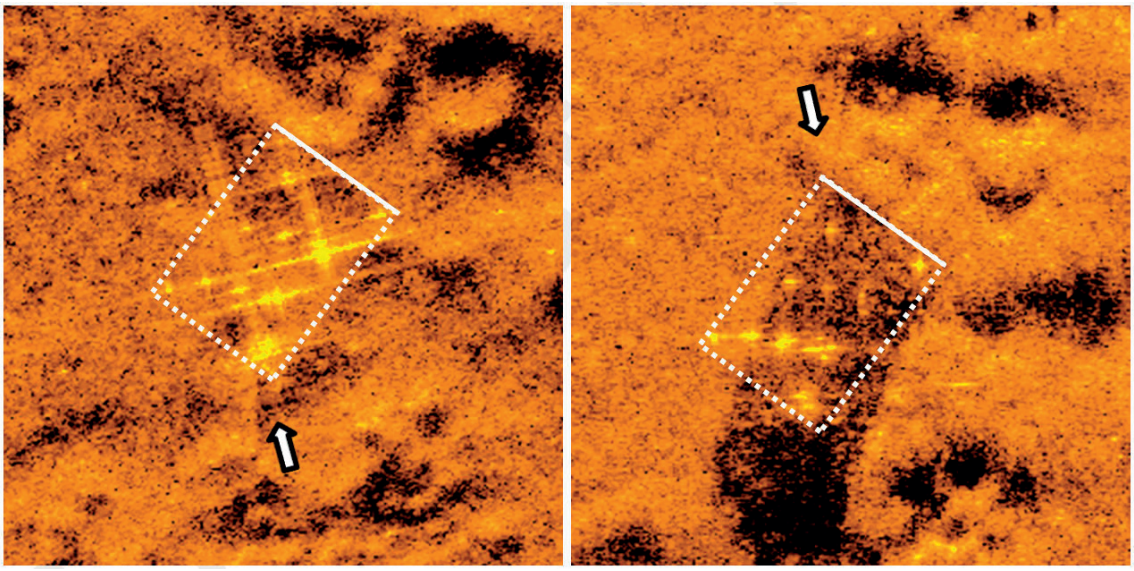

Figure IV.4: SAS intensity images measured over 60 kHz around 250 kHz with HISAS 2040 from a MUNIN AUV. The two images are recorded from opposite directions at 33 m range and 4.5 m altitude, and the observation directions are indicated by white arrows. The plate appears to be resting upside-down, on a 35 cm long cylinder in the corner and on the opposite short edge of the plate. The outline of the plate is indicated by the white rectangle, and the solid line marks the edge resting on the bottom.

IV.3.4 Measurements at 250 kHz "on-the-edge"

The two SAS images recorded around 250 kHz of Figure IV.5 indicate that the target plate is deployed vertically, resting on the 35 cm long cylinder (holding an acoustic transponder) and its closest short edge of the plate. The two SAS images show the target plate observed from two opposite directions.

In the left image, the bottom side of the plate is illuminated at close to normal incidence. All the scattering is gathered on a short range-interval close to the resting face of the plate, and a high contrast shadow is observed behind the plate. (A junction between two images can be observed as an artefact on the left side of the scene.)

In the right image, the front side of the plate with reflectors is illuminated. Because of the vertical orientation of the plate, these are also gathered on a rather short range interval. Also here, a high contrast shadow is observed at some range behind the plate. However, at short range a seafloor is observed. This is in fact a mirror reflection of the seafloor in front of the plate, resulting from the top edge of the plate being closer to the sensor than the resting edge of the plate. Because of the opposite direction of observation, this patch resembles more a flipped cutout of the image with the opposite direction of observation.

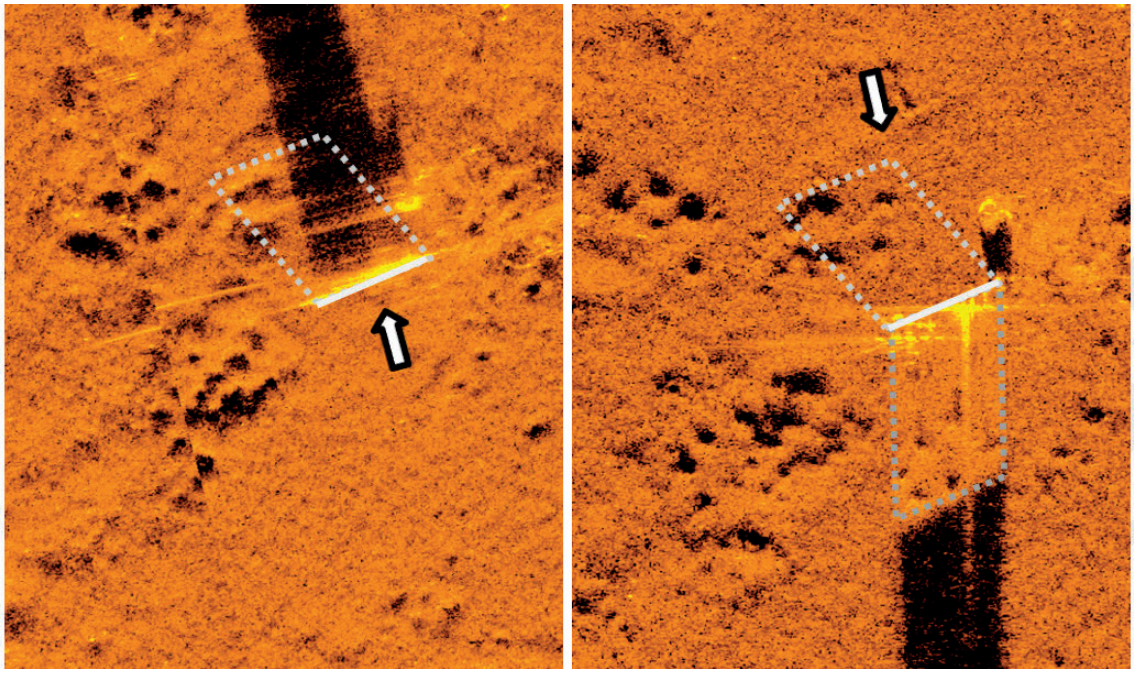

Figure IV.5: SAS intensity images measured over 60 kHz around 250 kHz with HISAS 2040 from a MUNIN AUV. The two images are recorded from opposite directions at 33 m range and 5.0 m altitude, and the observation directions are indicated by white arrows. The plate appears to be resting vertically on a 35 cm long cylinder in the corner and on the closest short edge of the plate. The outline of the plate is indicated by the white trapezoid, and the solid line marks the edge resting on the bottom. The gray trapeze indicates an area filled-in by mirroring off the plate.

IV.4 Discussion and Analysis

Our measurements of the prototype target shows that its mounting plate is transparent at 100 kHz, and that the attached reflectors are hard to separate from the seafloor. Our initial assumption that the 4 mm aluminum plate would not support transmission at 5-40 degrees grazing angles around 100 kHz was clearly wrong. After gathering the theory on scattering off metal plates in Section IV.2.2, these predictions confirm that the plate should provide only 2 dB reduction of the seafloor scattering at this frequency. However, the reduction of the seafloor scattering should rapidly increase if switching to a higher frequency. At 250 kHz the reduction should be around 30 dB, and this is qualitatively confirmed in Section IV.3.3. The targets are also strong compared to the background at 250 kHz, in contrast to what we experienced at 100 kHz, where our observations are consistent with the sound being transmitted through the plate, rather than reflecting off it. For normal incidence the theory indicates strong reflection, and indeed, with the vertically oriented plate of Section IV.3.4, we observe both a good image of the seafloor reflected off the plate, and a deep shadow.

In general, our measurements are in line with the predicted scatterings off both the aluminum plate and the targets. The prototype target has been useful as a benchmark for the theoretical models, but a redesign is needed for its intended use at 100 kHz: First, the mounting plate must be replaced by a 12 mm aluminum plate or a 8 mm steel plate in order to provide 40 dB reduction of the seafloor scattering. Next, the trihedral reflector should get a solid backside, in place of being constructed from metal plates, as metal plates are predicted to give strong transmission for the important 40-50 degrees incidence angle of looking directly into the corner.

IV.5 Conclusion

With the suggested changes, our calibrated target should be well suited for independent validation of scattering strength and frequency dependence estimates at 100 kHz. The target can be adapted for other frequencies by scaling the plate thickness and target dimensions inversely to the applied scaling of frequency.

Acknowledgments

The authors wish to thank Georgia Tech and in particular Daniel A Cook for directing us to the theory for transmission and reflection off elastic plates. The authors also wish to thank FFI's Prototype Workshop and in particular Pål Halvorsen for producing refined drawings and building the prototype target based on our hand sketch. The authors wish to thank Kongsberg Maritime and in particular Terje Halvorsen for recording data on our test target as they were finalizing the first HISAS 2040 SAS system on the new MUNIN AUV. And furthermore, the authors wish to thank all the participants of MAREX'17, including the RNoN who provided optical underwater images of the target with their HUGIN-MR AUV. And finally the authors wish to thank our colleagues Roy E Hansen, Torstein O Sæbø and Marc Geilhufe in FFI's SAS-team for ever enthusiastic and inspiring discussions.

References

Doerry, A. W. and Brock, B. C. (2009). *Radar cross section of triangular trihedral reflector with extended bottom plate*. Tech. rep. SAND2009-2993. Sandia National Laboratories, p. 38.

Fiorito, R., Madigosky, W., and Überall, H. (1979). "Resonance theory of acoustic waves interacting with an elastic plate". In: *The Journal of the Acoustical Society of America* vol. 66, no. 6, pp. 1857–1866.

Gallman, P. G. (2005). *Radar Reflectors for Cruising Sailboats*. Ulyssian Publications, p. 172.

Hansen, R. E. (2013). "Synthetic Aperture Sonar Technology Review". In: *Marine Technology Society Journal* vol. 47, no. 5, pp. 117–127.

Hansen, R. E., Lågstad, P., and Sæbø, T. O. (2019). *Search and monitoring of shipwreck and munitions dumpsites using HUGIN AUV with synthetic aperture sonar - technology study*. Tech. rep. FFI-rapport 19/00245. Norwegian DefenceResearch Establishment, pp. 1–33.

Lurton, X. (2010). *An Introduction to Underwater Acoustics, Principles and Applications*. Second. Springer, p. 680.

MUNIN AUV (accessed April 11, 2019). https://www.kongsberg.com/maritime/products/mari robotics/autonomous-underwater-vehicles/AUV-munin/.

Neto, A. A., Rodrigues, G. P., and Alvarenga, I. D. (2017). "Seabed mapping with HISAS sonar for decommissioning projects". In: *Sea Technology*, pp. 15–18.

Ødegård, Ø., Hansen, R. E., Singh, H., and Maarleveld, T. J. (2018). "Archaeological use of Synthetic Aperture Sonar on deepwater wreck sites in Skagerrak". In: *Journal of Archaeological Science* vol. 89, pp. 1–13. URL: http://linkinghub.elsevier.com/retrieve/pii/S0305440317301516.

Paper V

Spatial Coherence of Speckle for Repeat-Pass Synthetic Aperture Sonar Micronavigation

Stig Asle Vaksvik Synnes, Roy Edgar Hansen, Torstein Olsmo Sæbø

 DOI: 10.1109/JOE.2021.3060812.

Abstract

Accurate positioning of autonomous underwater vehicles (AUVs) is a major challenge. The long-term drift is problematic if global position updates are not available, and for applications such as repeat-pass interferometry and coherent change detection, millimeter accuracy is needed. Repeat-pass synthetic aperture sonar (SAS) micronavigation is one potential technique for countering both challenges. While single-pass SAS micronavigation enabled successful coherent processing within one track, the potential is that repeat-pass SAS micronavigation can support coherent processing between passes. Both techniques are based on recognizing the speckle pattern in the seafloor return, but repeat-pass SAS micronavigation has additional challenges with the larger temporal and spatial separations between the observations. In this study, we investigate the spatial correlation of speckle as observed from SAS systems. We divide the different contributions to spatial decorrelation into three groups: speckle decorrelation, footprint mismatch and stretching. We examine each contribution separately and develop simplified formulas for their decorrelation baselines. When correlating synthetic aperture images, decorrelation from stretching dominates. When correlating single element data recorded at low grazing angles common to SAS, speckle decorrelation dominates. We validate our findings on experimental data, and by combining elements into larger effective elements, we demonstrate increasing the across-track baseline for repeat-pass SAS micronavigation updates from less than 1 m to 10 m.

All authors are with the Norwegian Defence Research Establishment (FFI), Norway. Synnes is pursuing a Ph.D. at the University of Oslo, Norway, where Hansen is also adjunct professor.

V.1 Introduction

Autonomous underwater vehicles (AUVs) with synthetic aperture sonar (SAS) are used for a wide range of applications, including search and survey (Sæbø et al., 2015), marine geology (Denny et al., 2015), habitat monitoring (Sture et al., 2018), environmental monitoring (Neto et al., 2017), naval mine countermeasures (Midtgaard et al., 2016), change detection (Myers et al., 2014; Myers et al., 2020) and underwater archeology (Ødegård et al., 2018), and there is a huge potential of using SAS for bathymetric mapping (Callow et al., 2012; Griffiths et al., 1997). Many of these applications pose challenging demands for the AUV navigation, both regarding short time position accuracy and long term drift. A range of techniques are available both for absolute and relative position updates (Jalving et al., 2003). Absolute position updates can be obtained from global navigation satellite systems (GNSS), either by relaying position updates from a surface vessel or through surfacing. However, operating a surface vessel can be costly, and surfacing the underwater vehicle is not practical for operations at large depth or in highly trafficked areas. The use of terrain navigation with pre-made maps is a well demonstrated alternative for acquiring absolute or relative navigation updates in the underwater domain (Roman et al., 2007; Ånonsen et al., 2017). While this technique exploits terrain variations, its companion technique of feature based navigation can operate on smaller features or objects. Correlation of images can also be used for navigation, supporting distributed features or feature-points in intensity images (Midtgaard, 2013; Wang et al., 2017), or even direct correlation of image snippets using either intensity data or complex data (Hunter et al., 2017; Myers et al., 2020). Furthermore, successful SAS image formation is usually only obtained after incorporating micronavigation updates from the SAS sensor into the vehicle navigation (Bellettini et al., 2002). Initial studies have demonstrated that SAS micronavigation measurements can be used to obtained navigation updates also between passes under controlled experimental setups (Hunter et al., 2016; Hunter et al., 2015; Synnes et al., 2010).

V.1.1 Repeat-Pass SAS Micronavigation

Acoustic measurements on the seafloor typically return a speckle intensity pattern, originating from the superimposed backscattering of randomly distributed scatterers within each resolution cell (Oliver et al., 1998, Ch. 4.3). If the relative distance to the individual scatterers changes, the speckle pattern also changes. SAS micronavigation is based on recognizing the speckle pattern between time series of acoustic backscatter. Using a SAS system with a multi-element receiver array, element data of partially overlapping array positions from consecutive pings are cross-correlated in a search for the element pair and relative time delay with the highest degree of coherence, and the corresponding arguments give the along-track displacement and slant-range displacements (Bellettini et al., 2002; Dickey et al., 1978; Doisy, 1998).

Successful correlation of sensor data between passes is limited by temporal decorrelation, the relative orientation of the tracks, and the spatial separation between tracks (Zebker et al., 1992). Temporal decorrelation periods for the seafloor vary from days to perhaps a month in coastal shallow water at 100 kHz, but will be significantly shorter at higher frequencies, in rough weather, with strong currents, or with high animal activity at the seafloor (Lyons et al., 2013; Myers et al., 2014; Myers et al., 2013). Decorrelation from relative orientation between tracks was derived in (Zebker et al., 1992) and measured in (Hunter et al., 2016). Its impact can be minimized by minimizing the relative orientation of the tracks, and potentially also through beam-steering. The decorrelation with across-track separation has been visited only in preliminary studies, demonstrating valid repeat-pass micronavigation measurements for across-track separations of up to 0.7 m (Hunter et al., 2015; Synnes et al., 2010). A potential applicability to significantly longer separations has been indicated (Synnes et al., 2010). With a larger tolerance to across-track separation, navigation updates can also be acquired after a larger drift from the original position. The tolerance to across-track separation thus constitutes a key parameter for the feasibility of repeat-pass SAS micronavigation updates (Hunter et al., 2017).

In this article, we perform an in-depth study of the limitations to spatial separation for successful repeat-pass SAS micronavigation. Initially, we review the current status on estimation of the spatial coherence.

V.1.2 Spatial Coherence

The similarity of the speckle pattern between two recordings of acoustic backscatter can be expressed by the degree of coherence. The correlation function – or the spatial variance of the coherence – for an aperture is predicted from the van Cittert-Zernike theorem. This theorem has been successfully applied to optics and radio astronomy, and also to pulsed echo ultrasound (Born et al., 1999, Ch. 10.4.2.a), (Thompson et al., 2017, Ch. 15), (Mallart et al., 1991).

The decorrelation with *along-track baseline* is used for motion estimation in correlation sonar, including SAS micronavigation. Accurate knowledge of its functional form is crucial for acquiring navigation estimates of high accuracy and low bias (Bellettini et al., 2002; Dickey et al., 1978; Doisy, 1998), (Heremans et al., 2009, Ch. 5), (Brown et al., 2020).

The decorrelation with *range baseline* is fundamental for the applicability of SAS data from repeated passes. However, we have been unable to locate any prior study on the range baseline. We therefore evaluate the van Cittert-Zernike theorem for this dimension, and also derive simplified expressions on the feasible baselines for both along-track and range correlation.

The decorrelation with *change of grazing angle* between observations has been studied for the application of repeat-pass SAR interferometry. Using an approach

in line with the van Cittert-Zernike theorem, the decorrelation was first derived for an idealized geometry and shortly thereafter for more realistic scattering surfaces and interferometer geometries (Li et al., 1990; Rodriguez et al., 1992; Zebker et al., 1992). This decorrelation was later related to the ground wavenumber mismatch originating from a relative stretch between the observations (Cervenka, 2012; Gatelli et al., 1994).

We find it useful to group the different contributions to decorrelation into the three groups of *footprint mismatch*, addressing decorrelation from different illumination of the scene; *speckle decorrelation*, addressing decorrelation caused by different coherent contributions from scatterers within each range sample; and *stretching*, addressing decorrelation from different coherent contribution between range samples. We recognize that decorrelation by footprint mismatch can be reduced by beam steering and beam forming, and decorrelation from stretching can be reduced by de-stretching the time series. In contrast, speckle decorrelation is fundamental and cannot be avoided.

V.1.3 Claim

We investigate the spatial coherence of speckle for repeat-pass SAS micronavigation. In particular:

1. We derive *simple formulas* for the baseline decorrelation for each of the contributions to spatial decorrelation.

2. We show that *speckle decorrelation* with range baseline constitutes the most prominent source of decorrelation for single elements at small grazing angles.

3. We show that when combining elements into practical synthetic aperture lengths, decorrelation from *wavenumber stretching* constitutes the most prominent source of decorrelation if the stretching is left uncompensated.

4. We show how decorrelation from wavenumber stretching dominates over *wavenumber mismatch*, for the case of uncompensated stretching when using the same frequency band for both observations.

5. We estimate a *coherence floor*, or lower limit on the expectation value, for estimating coherence values through cross-correlation.

6. We demonstrate good *agreement* of spatial decorrelation estimates from the theoretical predictions, our simplified formulas and the experimental results.

7. We demonstrate *an increase of* the across-track baseline of successful repeat-pass SAS micronavigation updates from the less than 1 m reported in (Hunter et al., 2015; Synnes et al., 2010) to more than 10 m.

V.1.4 Outline

In Section V.2 we introduce the system geometry of interferometric SAS and the estimation of spatial coherence, including our derivation of the coherence floor. We evaluate the theoretical limit on the spatial coherence from the van Cittert-Zernike theorem, and derive simplified formulas for the maximum feasible along-track and range baselines limited by speckle decorrelation in Section V.3. In Section V.4 we evaluate the decorrelation by footprint mismatch, and in Section V.5 we evaluate the decorrelation from a change of grazing angle, expressed as a relative stretching of the ground wavenumber spectrum. We estimate both the decorrelation without de-stretching, and we quantify the remaining effect of wavenumber mismatch after a presumed ideal de-stretching. In Section V.6 we assemble our predictions in a table of simplified formulas for decorrelation baselines of coherence 0.5 for each of the investigated sources of decorrelation. We validate our findings on SAS measurements from an operational AUV in Section V.7. In Section V.8 we examine both our theoretical predictions and our measurement results. Finally, we summarize our main findings in Section V.9.

V.2 Spatial Coherence Estimation

In this section we present the geometry of interferometric SAS system and micronavigation measurements, before we give a brief introduction to the estimation of spatial coherence through cross-correlation of time series. We contribute by evaluating the effective coherence floor (or bias) on the expectation value of the maximum degree of coherence from a cross-correlation.

V.2.1 System Geometry

SAS processing is based on combining data from multiple pings in order to synthesize long apertures, allowing for generation of high-resolution images also at long range. SAS systems also employ multi-element receiver arrays, allowing them to transit further between pings, thereby increasing the area coverage rate (Hansen, 2011).

Figure V.1 shows the measurement geometry of an interferometric SAS system on an AUV with one transmitter and two vertically displaced receiver arrays. Using an interferometric SAS additionally allows for estimating the seafloor bathymetry (Sæbø et al., 2007b). We have indicated the relevant local earth-fixed coordinate system [x, y, z] that represents the along-track and across-track positions, and the altitude. The SAS system insonifies the seafloor within the sonar beamwidth, and we illustrate two range-patches through their seafloor footprint. The sonar data are recorded as a function of time, and thereby correspond to the slant range representation. The footprint of a patch on the seafloor constitutes the ground range representation.

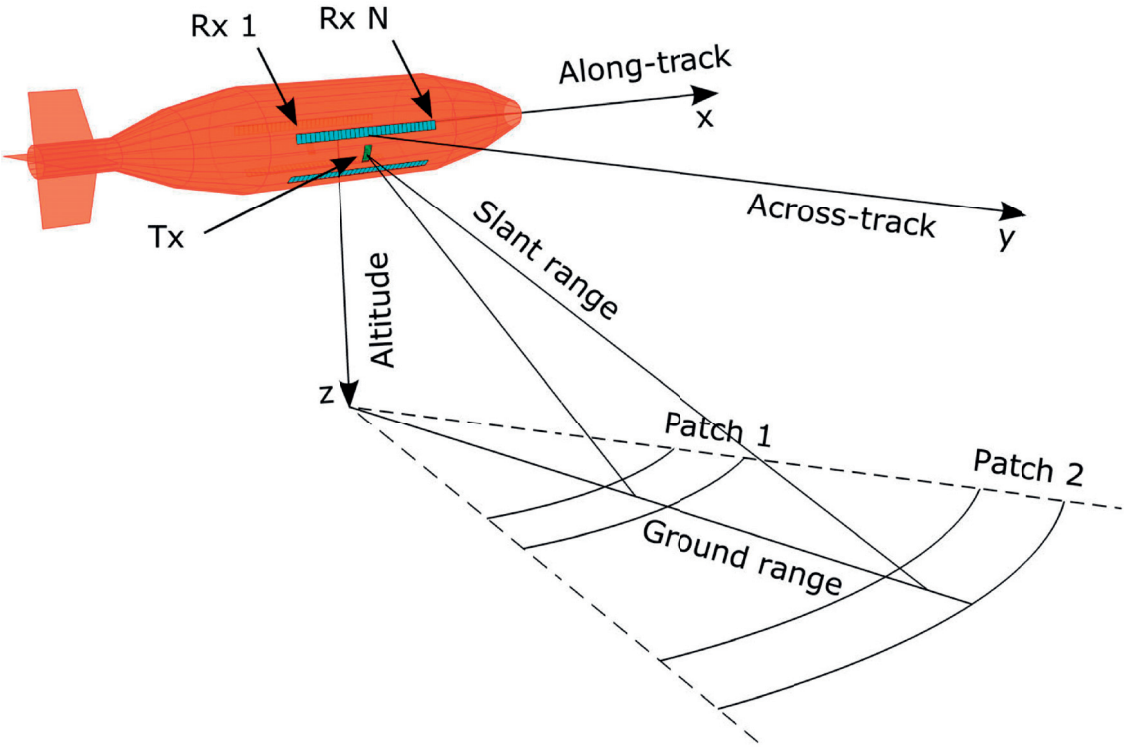

Figure V.1: The observation geometry of an interferometric SAS system, together with the acoustic footprint on the seafloor and relevant coordinate systems.

V.2.2 Phase Center Approximation

The use of multi-element receiver arrays and a moving AUV platform leads to a bistatic recording geometry, with the transmitter in one focal point, and each receiver in the other. This geometry can be simplified by representing each pair by an effective monostatic element at the phase center between the transmitter and each receiver. This approximation is valid for ranges $r \gg D^2/4\lambda$, where D is the distance between the transmitter and receiver positions and λ is the wavelength at the center frequency (Bellettini et al., 2002). Throughout this paper we adopt the phase center approximation (PCA), and obtain an array of PCA-elements with half the effective element spacing of the physical receiver element spacing.

V.2.3 SAS Micronavigation

The SAS system transmits an acoustic signal into the water. The signal is scattered back by the seafloor and is observed by the receiver array. The receiver elements make spatially independent observations of the *scattered field*. Element data from different pings, recorded at roughly the same position, can be correlated to provide navigation updates. Overlapping phase centers will have the highest coherence, and give the along track displacement, while the relative change in round trip time gives the slant range displacement (Bellettini et al., 2002; Dickey

et al., 1978; Doisy, 1998). The accuracy of the estimates follows from the degree of coherence and the system parameters (Bellettini et al., 2002). Revisiting a phase center position between consecutive pings in a pass can be achieved by operating with overlapping phase centers in the technique of micronavigation (Bellettini et al., 2002), and between passes by re-running a pass at a small crossing angle (Synnes et al., 2010). The resulting element combinations are illustrated in Figure V.2.

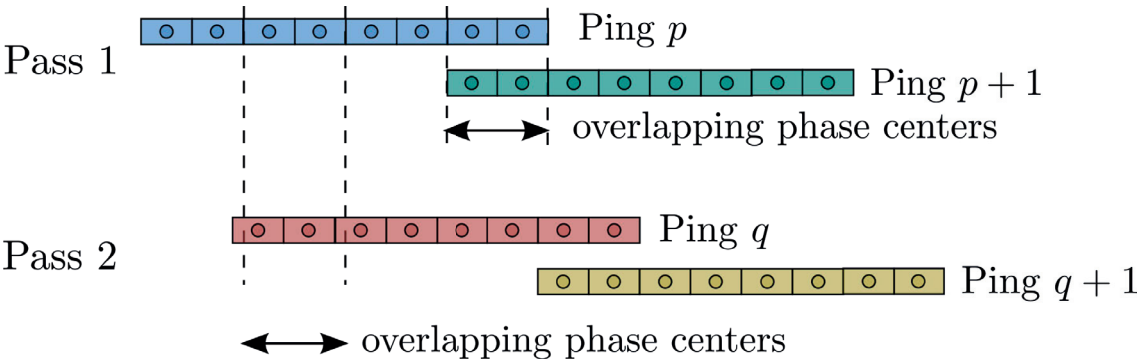

Figure V.2: Overlapping phase centers between consecutive pings p and $p+1$ from pass 1, and between ping p from pass 1 and ping q from pass 2. For the latter case, we indicate only two out of many overlapping phase centers.

V.2.4 Signal Model

Assume a scene containing a random distribution of scatterers that are small compared to a resolution cell. This results in a speckle scene, and the pixel values possesses a circularly-symmetric complex Gaussian distribution (Oliver et al., 1998, Ch. 4.3). We assume that the noise is additive and white and thus also possesses a circularly-symmetric complex Gaussian distribution.

We model the data $a_i(t)$, recorded as a function of ping propagation time t from two repeated passes $i \in \{1, 2\}$ over a scene, as the combination of one common signal component $g(t)$, with amplitude s, and a random noise realization $h_i(t)$, with amplitude n:

$$\begin{aligned} a_1(t) &= sg(t) && + nh_1(t) \\ a_2(t, \tau_0) &= sg(t - \tau_0) && + nh_2(t) \end{aligned} \tag{V.1}$$

where τ_0 is an unknown relative delay of signal 2.

V.2.5 Degree of Coherence

We choose to express the similarity between the two signals a_1 and a_2 through their *degree of coherence* γ, representing their linear dependence versus time

delay τ between the signals,

$$\hat{\gamma}(\tau) = \frac{|\langle a_1^*(t) a_2(t-\tau)\rangle|}{[\langle |a_1(t)|^2\rangle \langle |a_2(t)|^2\rangle]^{1/2}}. \tag{V.2}$$

Here $\hat{}$ indicates an estimate, * represents the complex conjugate, and $\langle\ \rangle$ is an ensemble over time. By insertion of (V.1) into (V.2) and accounting for the delay by setting $\tau = \tau_0$, it follows that if the noise components are independent both of each other and of the signal, the population coherence directly relates to the signal energy s^2 and the noise energy n^2 (Zebker et al., 1992),

$$\gamma = \frac{s^2}{s^2 + n^2}. \tag{V.3}$$

For *finite time series*, the assumptions of independence between the time series do not hold, and the coherence estimator of (V.2) will have a bias towards higher values. This bias is most prominent for lower coherence values and few independent samples, as derived from the probability density function $p(\hat{\gamma}|\gamma, M)$ of the coherence estimate $\hat{\gamma}$, which is available as a function of population coherence γ and a number of independent samples M in (Carter et al., 1973).

V.2.6 Cross-Correlation

An unknown time delay between two complex time series can be estimated by cross-correlation, evaluating the degree of coherence from (V.2) for a range of candidate delays, and choosing the delay corresponding to the maximum degree of coherence. However, in the case of finite length uncorrelated sequences, selecting the maximum value over many delays causes an increase in the maximum value. This again, causes an increased bias in the estimated coherence. We find that in-depth knowledge of this bias is important for choosing a good implementation of the time delay estimation. In the remainder of this section, we derive this bias, and compute the resulting coherence floor.

V.2.6.1 Bias

We choose a cross-correlation implementation that estimates the coherence over all candidate lags using a sliding window inner product. We thus avoid any bias (or weighting) from non-overlapping time series for non-zero lags. Next, we assume that the signals are critically sampled and estimate the coherence for lags corresponding to L different sample offsets. Thus, all except one of the lags should correspond to correlating noise with noise. Their expected maximum value will increase with the number of lags evaluated, and constitutes a bias on the cross-correlation estimate. Such a bias can be expressed as

$$b = E\{\hat{x}\} - x, \tag{V.4}$$

where $\hat{x}$ is the estimated value and x the true value. For a distribution with non-zero probability of estimates $\hat{x} > 0$ only, the expected value can be calculated

directly from the cumulative distribution function (CDF) $P(\hat{x})$ (Ewens et al., 2005, p. 29),

$$E\{\hat{x}\} = \int_0^\infty (1 - P(\hat{x}))\, d\hat{x}. \tag{V.5}$$

The criteria for using (V.5) is met when operating on the degree of coherence from (V.2). Furthermore, the CDF for the coherence estimate as a function of true coherence γ and number of independent samples M, $P(\hat{\gamma}|\gamma, M)$, is available from (Carter et al., 1973). If we can also express the CDF of the maximum over multiple lags, that can be used with (V.4) and (V.5) to provide the expected bias on the coherence of the cross-correlation estimate.

V.2.6.2 Coherence Floor

For the case of $\gamma = 0$, the true coherence is zero for any lag, such that the maximum over L lags at critical sampling corresponds to the maximum over L independent samples from $P(\hat{\gamma}|\gamma = 0, M)$. The CDF for the maximum of L independent samples $P_{\max}(\hat{x}, L)$ taken from a distribution with CDF $P_x(\hat{x})$ is (Ewens et al., 2005, p. 92),

$$P_{\max}(\hat{x}, L) = P_x(\hat{x})^L. \tag{V.6}$$

Thus, for $\gamma = 0$, we can use $P(\hat{\gamma}|\gamma, M)$ from (Carter et al., 1973) with (V.5) and (V.6) to predict the estimated coherence from a sliding window cross-correlation,

$$\hat{\gamma}(\gamma = 0, M, L) \; = \int_0^1 \left(1 - P(\hat{\gamma}|0, M)^L\right) d\hat{\gamma}. \tag{V.7}$$

The coherence estimate has its lowest expectation value for $\gamma = 0$, where only the bias contributes, and we denote this minimum the coherence floor. In order to illustrate the impact of the bias, we evaluate the coherence floor for different numbers of independent samples M and lags L, and present the results in Figure V.3. We observe that in order to keep the coherence floor at a minimum, the search of the cross-correlation should use long time series and cover a minimum number of lags. The latter can be achieved by exploiting any a priori information on the expected lags.

V.3 Speckle Decorrelation

In this section we evaluate the theoretical limit on the spatial coherence from the van Cittert-Zernike theorem, and we derive simplified formulas for the maximum feasible along-track and range baselines.

V.3.1 The van Cittert-Zernike Theorem

A speckle pattern originates from the superimposed backscattering of all scatterers within each resolution cell. If the relative distance to the individual scatterers changes, the speckle pattern also changes.

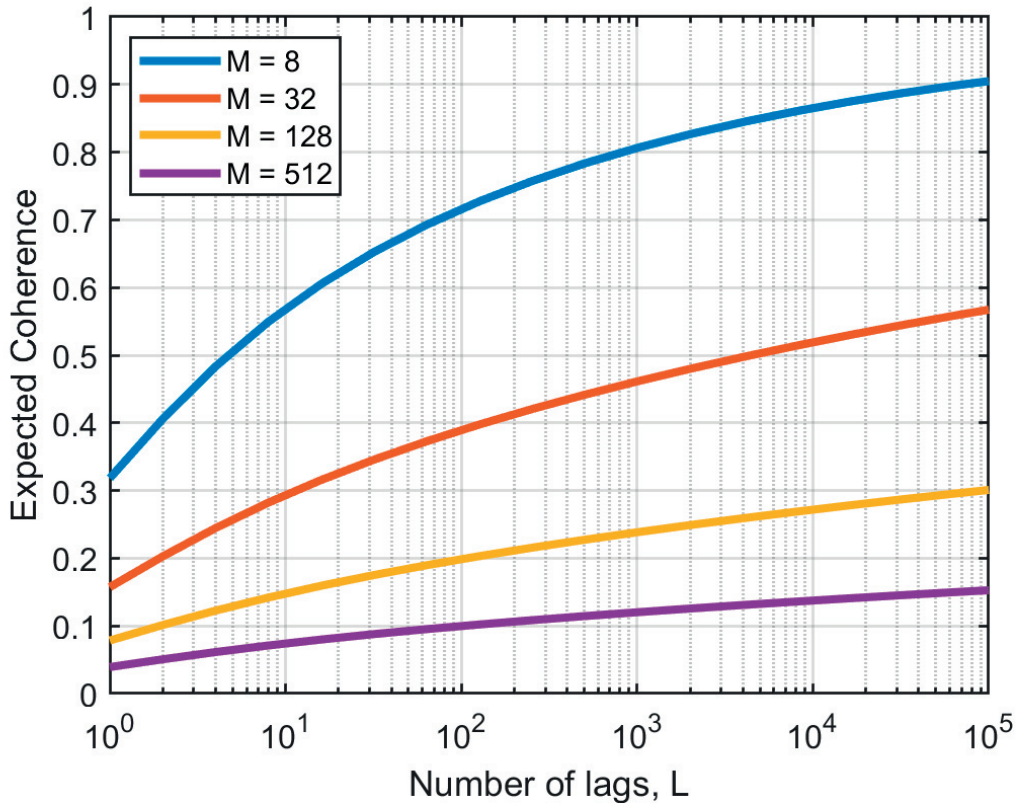

Figure V.3: Effective coherence floor of the cross-correlation estimator for different number of independent samples M and number of lags L evaluated, using a sliding window cross-correlation.

The van Cittert-Zernike theorem, developed in the field of statistical optics, relates the spatial coherence of the field measured at two points to the spatial intensity distribution of an incoherent source (Born et al., 1999, Ch. 10.4.2). The theorem cannot be applied directly to coherent acoustic sources, though it can be applied to the incoherent acoustic field scattered off a speckle scene, treating this as an incoherent source (Mallart et al., 1991): The pressure field $H_i(\vec{p})$ at seafloor position $\vec{p}$ and originating from transducer i, can be estimated by integrating the contributions from all positions $\vec{s}$ on the front surface of the transducer. With $O_i(\vec{s})$ representing the aperture function of transducer i, the pressure field becomes

$$H_i(\vec{p}) = \iint_{\text{transducer}} O_i(\vec{s}) \frac{e^{jkr_i}}{r_i} dS, \tag{V.8}$$

where $r_i = |\vec{p} - \vec{s}|$ and $k = 2\pi/\lambda$ is the acoustic wavenumber at wavelength λ. The scattered field follows as the product of the pressure field and the scattering function. Assuming an unresolvable, randomly distributed microstructure, the autocorrelation of the scattering function is non-zero for zero spatial lag only, where it returns the scattering amplitude χ_0 of the medium. The spatial

covariance, Γ_{12}, between the two transducers at their separate positions thus follows from the van Cittert-Zernike theorem as

$$\Gamma_{12} = \chi_0 \iiint_{\text{scene}} \frac{H_1 H_2^*}{r_1 r_2} e^{jk(r_2 - r_1)} dV, \tag{V.9}$$

where we have assumed that χ_0 is representative over the scene. The spatial coherence follows by normalization,

$$\gamma_{12} = \Gamma_{12} / \sqrt{\Gamma_{11}\Gamma_{22}}. \tag{V.10}$$

While the van Cittert-Zernike theorem propagates the spatial correlation in 3D, it is perhaps most known for describing a 2D Fourier relation orthogonal to the look direction between the spatial coherence and the spatial intensity distribution of an incoherent source. This Fourier relation applies as long as both the dimensions of the source and the distance between the observations are small compared to the distance to the source (Born et al., 1999, Ch. 10.4.2). With pulse echo measurements, the scattered field from a speckle scene can be treated as a distributed incoherent source (Mallart et al., 1991). We note that there is a 2D Fourier relation also between the aperture function and the scattered field in the far field region (Goodman, 2005, Ch. 4.3). The spatial coherence (orthogonal to the look direction) from the combined use of multiple apertures is given by the product of the spatial coherence of each aperture. From the Fourier relations, it follows that the spatial coherence orthogonal to the look direction can be obtained directly from a normalized convolution of the individual aperture functions.

V.3.2 Numerical Evaluation

In order to establish the correlation function for along-track and range baselines between two single ping SAS measurements, we have performed a numerical evaluation of the van Cittert-Zernike theorem.

The spatial covariance of (V.9) is separable on range and the cross-range coordinates (Mallart et al., 1991), such that for short patch lengths l, the spatial coherence can be estimated through an evaluation at a single range. We simplify this evaluation by adopting a flat seafloor and by positioning the transducers in the seafloor plane. Switching to a polar coordinate system (r_1, α_1) with transducer 1 at the origin and facing $\alpha_1 = 0$, the Jacobian becomes r_1, and the integral of (V.9) can be reduced to

$$\Gamma_{12}(r_1) \approx l\chi_0 \int_{-\pi/2}^{\pi/2} \frac{H_1 {H_2}^*}{r_2} e^{jk(r_2 - r_1)} d\alpha_1. \tag{V.11}$$

In our numerical evaluation, we computed H_i over a fine Cartesian 2D grid, using a transmitter element of length $d = 2.5\lambda$, corresponding to a -3dB beamwidth

of 23°, and using a different number, N, of combined receiver elements for reception. We windowed H_1 around a patch range of $r_1 = 100\,\mathrm{m}$, and convolved this range-tapered H_1 with H_2 in order to estimate the covariance from (V.11) as a function of along-track and across-track baselines. We present the resulting predictions of the coherence $\hat{\gamma}$ in Figure V.4, where we have normalized the baselines on the element length d and wavelength λ.

For the along-track baseline, the spatial coherence could also have been obtained from the autocorrelation of the combined transmitter-receiver aperture function. If either transmitter or receiver is small, the shape should approximate a triangle, and with transmitters and receivers of equal length, the shape should approach a Gaussian (Brown et al., 2020; Mallart et al., 1991). This is in line with our results in Figure V.4 for respectively long and short effective receiver elements.

For the range baseline we have been unable to find any published results. Our numeric evaluation shows that for baselines larger than δ^2/λ, similar to the nearfield-farfield crossover (Lurton, 2010), the coherence decays exponentially with the baseline. For shorter baselines, the coherence decays more weakly with baseline. The different decays of the two regions are consistent with different processes dominating at either side of the nearfield-farfield crossover. In both regions, the decorrelation is slower for large apertures or small wavelengths.

V.3.3 Critical Baseline and Decorrelation Baseline

The *critical baseline* is the minimum baseline, Δ, for which two observations decorrelate completely, and we denote this $\Delta_{\gamma=0}$. The expression is commonly used as a compact representation of decorrelation from stretching, caused by a relative change of grazing angle, which is assumed to decay linearly with the baseline. In order to relate the impact of contributions to decorrelation with non-linear decay, including the across-track decorrelation that only asymptotically approaches zero, we choose to consider the baseline where the coherence between two observations is 0.5, $\Delta_{\gamma=0.5}$, and we define this the *decorrelation baseline*.

V.3.4 Predicted Decorrelation Baseline at Far Range

We develop an approximate expression for the decorrelation baseline of coherence 0.5 at far range. We simplify the task by addressing only the two scatterers within the -3dB beamwidth that encounter the maximum relative phase shift with changed along-track and range baselines, as illustrated in Figure V.5. We hypothesize that the baseline that changes the two-way traveled distance over the -3dB beamwidth β by one wavelength corresponds to the decorrelation baseline of coherence 0.5. We have validated our results on the along-track and across-track baselines through a comparison with both the numerical evaluation of V.3.2, and to already published experimental results.

We let r_0 denote the one-way traveled distances between the original sensor

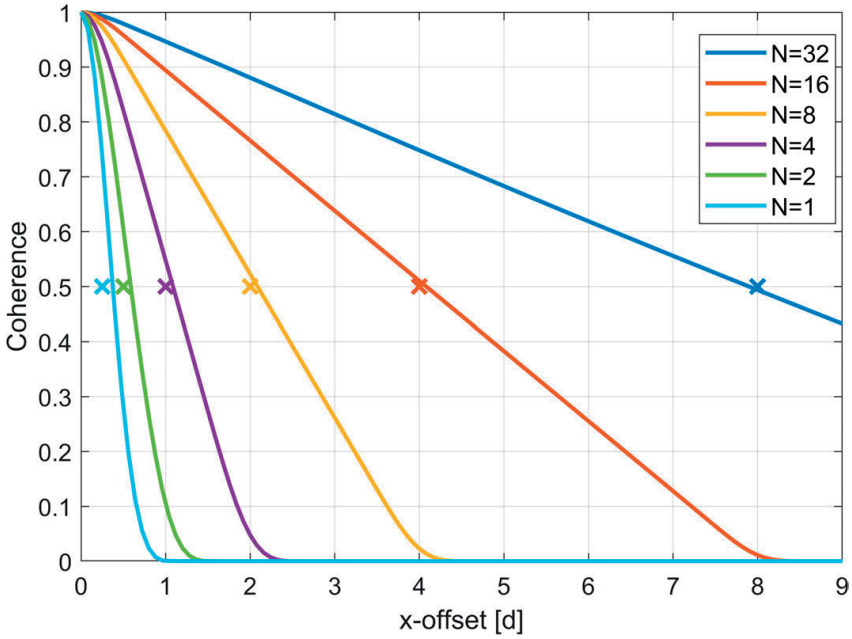

(a) Along-track baseline decorrelation

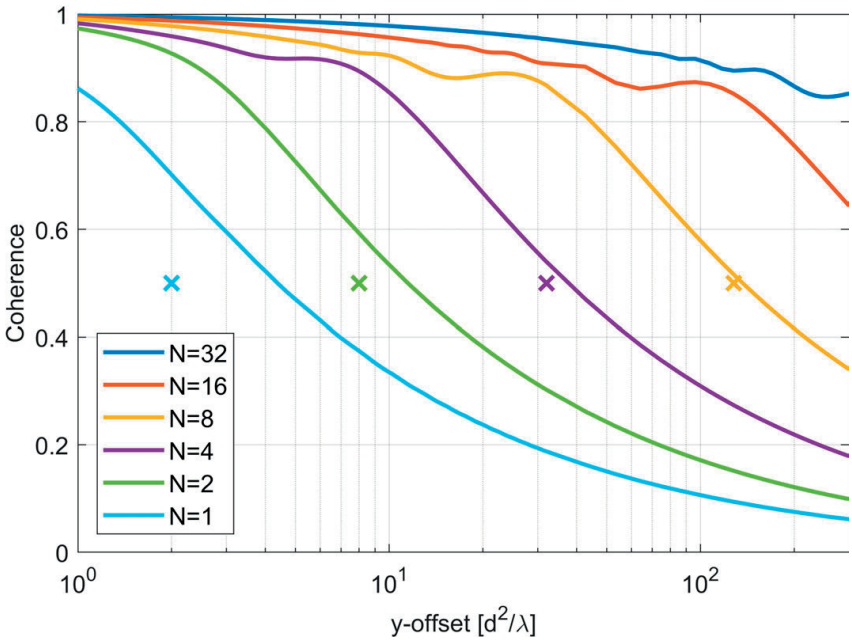

(b) Across-track baseline decorrelation

Figure V.4: Baseline decorrelation for SAS systems as predicted from the van Cittert-Zernike theorem, shown as solid lines. For simplicity, we have assumed equally sized transmitter- and receiver-elements and an in-plane seafloor, and results for combining multiple receiver elements N into larger effective elements are displayed in the labeled colors. The decorrelation baseline of coherence 0.5 from our simplified formulas of (V.15) and (V.16) for effective element length of $\delta_{\text{eval}} = Nd$ is included as crosses (x). The evaluation has been executed for a patch range of 100 m, a wavelength of $\lambda = 1.5\,\text{cm}$ and an element length of $d = 2.5\lambda$ resulting in an element beamwidth of 23°.

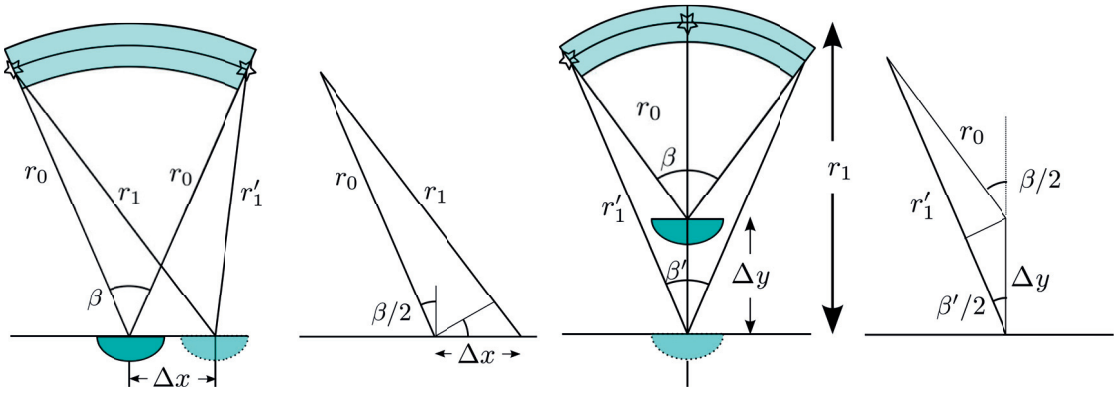

(a) Along-track baseline decorrelation (b) Across-track baseline decorrelation

Figure V.5: Baseline decorrelation on a speckle scene follows from the relative change of traveled distance, $\Delta r = |\Delta r_0 - \Delta r_1|$, within the sensor footprint as a function of along-track baseline, Δx, and across-track baseline, Δy. The beamwidth is β and the stars indicate the location of the scatterers with the maximum relative change of traveled distance for each geometry.

position and either scatterer, and for shifted sensor positions, we use the notation r_1 and r_1', to obtain the relative change of the one-way traveled distance between the two scatterers,

$$\Delta r = (r_1 - r_0) - (r_1' - r_0) = r_1 - r_1'. \tag{V.12}$$

For the along-track offset $\Delta x \ll r_0$ of Figure V.5a we obtain

$$\Delta r(\Delta x) \approx 2(r_1 - r_0) \approx 2\Delta x \sin(\beta/2). \tag{V.13}$$

The relative change of the one-way traveled distance between the two scatterers of Figure V.5b for an across-track offset $\Delta y \ll r_0$ is

$$\Delta r(\Delta y) = \; r_1 - r_1' \approx \Delta y - \Delta y \cos(\beta/2). \tag{V.14}$$

We insert for the relative two-way distance of one wavelength, $2\Delta r = \lambda$ in (V.13) and (V.14), and assume an linear array of effective length $\delta > \lambda$, such that we can approximate $\sin \beta/2 \approx \lambda/2\delta$ and $\cos(\beta/2) \approx 1 - (\beta^2/8)$. We thereby predict the decorrelation baselines

$$\Delta x_{\gamma=0.5} \approx \frac{\delta}{4} \tag{V.15}$$

$$\Delta y_{\gamma=0.5} \approx \frac{2\delta^2}{\lambda} = \frac{2d}{\beta}, \tag{V.16}$$

valid for baselines $\Delta x \ll r_0$ and $\Delta y \ll r_0$. Here δ is an effective element length with -3dB beamwidth matching that of the combined transmitter and receiver beampatterns. Where either transmitter or receiver is long and the other short, the effective array length is roughly the length of the longest, such that for

using a receiver of N times the length of the transmitter length d, we approach $\delta = Nd$ for large N. Where both transmitter and receiver are of equal length, the effective element length is $\delta = \sqrt{2}d$ (Rindal, 2019, App. A).

We have validated the along-track decorrelation baseline predicted from using (V.15) with $\delta = Nd$ by comparing with the experimental results for $N = 16$ and $N = 31$ from (Mallart et al., 1991). While we have moved both transmitter and receiver (in order to represent correlation between SAS pings), they only moved the receiver. Thus their result of twice our predicted baselines is consistent with the expectations, as they only experience half our change of travel distance.

We also indicate our predicted decorrelation baselines of (V.15) and (V.16) for effective element lengths of $\delta_{\text{eval}} = Nd$ and $r_0 = 100\,\text{m}$, by crosses in Figure V.4. This allows for comparison with the along-track and across-track baseline decorrelation from our evaluation of the van Cittert-Zernike theorem in V.3.2. We observe that for large N, both the along-track decorrelation baseline of (V.15) and the across-track decorrelation baseline of (V.16) are in line with our evaluation of the van Cittert-Zernike theorem. For smaller N, there is an increasing discrepancy, but we observe that for $N = 1$, this error matches the approximation error of $\delta_{\text{eval}} = \delta_{\text{true}}/\sqrt{2}$ and δ^2_{eval} for the along-track and across-track decorrelation baselines respectively. This indicates that our expressions for these decorrelation baseline are quite accurate.

V.3.5 Predicted Decorrelation Baseline at Near Range

We recognize that the requirements of $\Delta x \ll r_0$ and $\Delta y \ll r_0$ for the validity of (V.15) and (V.16) roughly correspond to matching beamwidths and ranges of the two observations. This requirement is typically met for the along-track baseline Δx, as the minimum practical operation ranges for synthetic aperture systems is a huge number of element lengths, and even many physical array lengths. For the across-track baseline, however, the requirement is challenged for long effective baselines and/or short wavelengths. We therefore revisit the derivation of speckle decorrelation with across-track baseline for this domain. We stress that this derivation only addresses decorrelation within the overlapping footprints, while the effect of decorrelation from the footprint mismatch with across-track baseline is treated separately in V.4.2.

The relative change Δr of the one-way traveled distance between the two scatterers of Figure V.5b can be expressed as a function of the across-track offset Δy from inserting the relation $r_1 = r_0 + \Delta y$ into (V.12) to provide

$$\Delta r = r_0 + \Delta y - r_1'. \tag{V.17}$$

The unknown r_1' can be obtained by applying the law of cosines on Figure V.5b to give

$$r_1'^2 = r_0^2 + \Delta y^2 + 2r_0 \Delta y \cos(\beta/2). \tag{V.18}$$

We can now obtain $r_1'^2$ both from (V.17) and (V.18) and solve the equations for Δy. In order to estimate the decorrelation baseline of coherence 0.5, again we insert for the relative two-way distance of one wavelength, $2\Delta r = \lambda$, and assume a linear array of effective length $\delta > \lambda$, such that we can approximate $\cos(\beta/2) \approx 1 - (\beta^2/8)$, where $\beta = \lambda/\delta$. We then reach an expression for the across-track decorrelation baseline from curvature mismatch,

$$\Delta y_{\gamma=0.5} = \frac{1 - \frac{\lambda}{4r_0}}{\frac{\lambda}{4\delta^2} - \frac{1}{r_0}} \approx \left(\frac{\lambda}{4\delta^2} - \frac{1}{r_0} \right)^{-1}, \tag{V.19}$$

where the approximation is valid for the general case of $r_0 \gg \lambda/4$. We may rewrite (V.19) as a scaling of the far-range decorrelation baseline $\Delta y_\infty = 4\delta^2/\lambda$ of coherence 0.5 from (V.16) to give

$$\Delta y_{\gamma=0.5}(r_0) = \Delta y_\infty \left(1 - \Delta y_\infty / r_0\right)^{-1}. \tag{V.20}$$

Here r_0 represents the shortest of the two ranges, such that $\Delta y > 0$. The near range extension of (V.16) through (V.19) and (V.20) is thus applicable for any $r_0 > \Delta y_\infty$, while for ranges $r_0 < \Delta y_\infty$, the coherence is always above 0.5.

We recall that the speckle decorrelation of (V.20) is evaluated over the overlapping footprint only. It is therefore always accompanied by the decorrelation from footprint mismatch with an along-track baseline, addressed in Section V.4.2. Comparing the two shows that speckle decorrelation has the shortest decorrelation baseline of the two contributions only for ranges $r_0 < 2\Delta y_\infty$.

V.4 Footprint Mismatch

In this section we investigate decorrelation from a footprint mismatch between observations, and specifically its effect in change of scene illumination after accounting for any difference in time delay. We note that the related term of *footprint shift* is typically used for the offset before delay compensation (Cervenka, 2012). Here, we focus on the change of azimuth look direction, causing an azimuth mismatch between the sensor footprints, and on changes of across-track or vertical distance, causing changes of the sector span of the footprint. We note that changes of the footprint illumination with recording geometry can be reduced and potentially mitigated if the beam can be steered and the beamwidth altered to compensate for any changes induced by the recording geometry. This can be done in post-processing for the case of combining multiple elements before cross-correlating.

V.4.1 Azimuth Look Direction

The decorrelation with change of azimuth look direction, $\Delta\alpha$, has been investigated in (Zebker et al., 1992). The coherence was found to fall linearly

with $|\Delta\alpha|$ and pass the coherence of 0.5 at an azimuth look direction of

$$|\Delta\alpha|_{\gamma=0.5} \approx \frac{\beta}{2\cos\varphi}, \tag{V.21}$$

where φ is the grazing angle on the seafloor. The result applies to a sinc azimuth beampattern, and can thus be adopted for linear arrays with -3dB beamwidth $\beta < \cos\varphi$.

V.4.2 Across-Track Baseline

The decorrelation from footprint mismatch with across-track baseline can be related to the overlapping sector lengths of Figure V.5b. By adopting the simplified beampattern from V.3.4 with unity intensity within the -3dB beamwidth and zero outside, the coherence follows from the radial overlap,

$$\gamma_{\text{rad}} = \frac{\beta'}{\beta} \approx \frac{r_0}{r_1'} \approx \left(1 + \frac{\Delta y}{r_0}\right)^{-1}, \tag{V.22}$$

where we have inserted r_1' from (V.17) and approximated $\beta \ll 1$ and $\Delta y \gg \Delta r$. We solve for Δy and obtain

$$\Delta y \approx r_0 \left(\frac{1}{\gamma_{\text{rad}}} - 1\right). \tag{V.23}$$

The across-track decorrelation baseline of coherence 0.5 from across-track baseline footprint mismatch is therefore $\Delta y \approx r_0$.

V.4.3 Altitude

A sensor with -3dB beamwidth β has a footprint of length $l = r\beta$ when the sensor is located at the ground level. From the derivation of (V.21), we deduce that an elevated sensor, observing the ground with a grazing angle φ, will have a footprint of length

$$l(\beta, \varphi) \approx \frac{r\beta}{\cos\varphi} \tag{V.24}$$

for $\beta < \cos\varphi$. By adopting a simple model of the beampattern with unity amplitude within the -3dB width and zero outside, we estimate that a change of grazing angle will give a decorrelation from the related footprint mismatch of

$$\gamma \approx \frac{l(\beta, \varphi_{\min})}{l(\beta, \varphi_{\max})} = \frac{\cos\varphi_{\max}}{\cos\varphi_{\min}}. \tag{V.25}$$

We evaluate the decorrelation baseline of coherence 0.5 from (V.25), and find that the resulting change of grazing angle roughly can be numerically approximated by

$$\Delta\varphi_{\gamma=0.5} \approx \frac{1}{3}(\pi - 2\varphi_{\min}). \tag{V.26}$$

V.5 Stretching

In this section we investigate decorrelation from a change of grazing angle, through examining the related relative stretching of the ground range sampling. Our contribution is to relate the stretching to decorrelation, and to develop a formula for the decorrelation baseline. We conclude the section by examining candidate approaches for stretch compensation, which can be used to reduce or sometimes even mitigate decorrelation from change of grazing angle.

V.5.1 Change of Grazing Angle

Observations of the seafloor with different grazing angles measure different spectral components of the seafloor scattering. This results in a decorrelation caused by a combination of wavenumber mismatch and stretching of the data within the overlapping wavenumbers (Li et al., 1990; Rodriguez et al., 1992; Zebker et al., 1992), (Gatelli et al., 1994). The decorrelation from stretching within the overlapping wavenumbers can be reduced or even mitigated if the stretching is accurately estimated and compensated for. The limitations by volume or out-of-plane contribution has been studied in (Gatelli et al., 1994; Rodriguez et al., 1992). The decorrelation from wavenumber mismatch can be avoided either by changing the measurement frequency, or at the cost of reduced range-resolution by bandpass filtering the overlapping ground wavenumbers, under the assumption that there is some overlap (Gatelli et al., 1994; Reigber, 1999).

The wavenumber shift for small relative bandwidth and homogeneously sloping ground was estimated and compensated for in (Gatelli et al., 1994). This approach was extended to large relative bandwidths by including wavenumber stretching and de-stretching in (Cervenka, 2012). Here we use a ground wavenumber interpretation to reach their expression on stretching as a function of a change of grazing angle.

Consider an acoustic signal interacting with the seafloor at grazing angle φ, that maps the seafloor scattering at ground wavenumber

$$K_g(\varphi) = 2k_a \cos\varphi, \tag{V.27}$$

where the acoustic wavenumber is $k_a = 2\pi f/c = 2\pi/\lambda$. If the grazing angle is increased by $\Delta\varphi$, the same acoustic signal will map a smaller ground range wavenumber,

$$K_g(\varphi + \Delta\varphi) = 2k_a \cos(\varphi + \Delta\varphi), \tag{V.28}$$

reflecting that the seafloor is sampled more sparsely, and is illustrated in Figure V.6. Following (Cervenka, 2012), we obtain the scaling factor $\chi \in \langle 0, 1]$ (or inverse stretching factor) from the ratio of (V.28) to (V.27), and can derive

$$\chi(\varphi, \Delta\varphi) \quad = \quad \frac{K_g(\varphi + \Delta\varphi)}{K_g(\varphi)} = 1 - \frac{\Delta K_g(\varphi, \Delta\varphi)}{K_g(\varphi)}$$

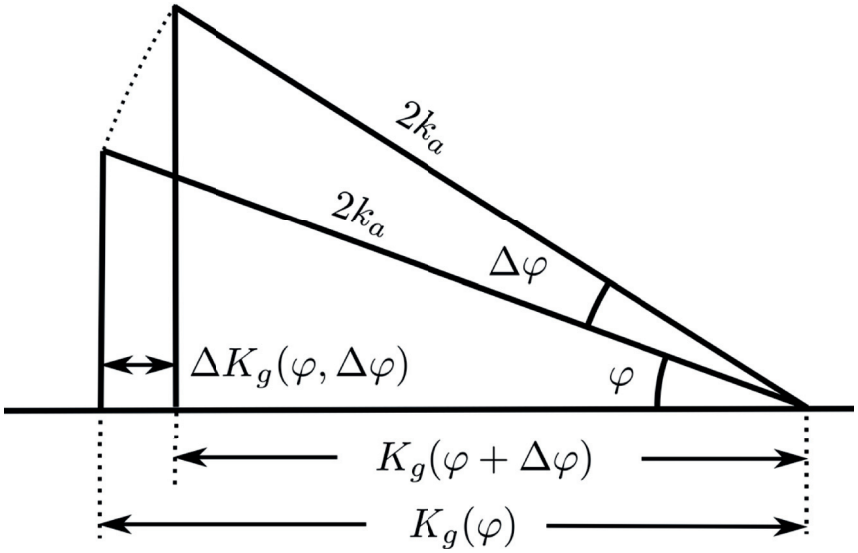

Figure V.6: The acoustic signal of wavenumber k_a maps the seafloor scattering at different ground wavenumbers K_g at seafloor grazing angles φ and $\varphi + \Delta\varphi$.

$$= \frac{\cos(\varphi + \Delta\varphi)}{\cos(\varphi)} \approx 1 - \Delta\varphi \tan(\varphi), \tag{V.29}$$

where the approximation is valid for a small change of grazing angle, where $\cos(\Delta\varphi) \approx 1$ and $\sin(\Delta\varphi) \approx \Delta\varphi$.

V.5.2 Ground Wavenumber Mismatch

Vertical baseline and bottom slope can give a reduction of ground range wavenumber overlap between two observations. We quantify this decorrelation through the critical baseline. When the change of grazing angle between two observations results in a relative reduction of ground wavenumber that matches the ratio of bandwidth B to maximum frequency $f_{\max}$, there is no common information between the two observations, and we have reached the critical baseline (represented by the change of angle $\Delta\varphi_{\gamma=0}$),

$$\frac{\Delta K_g(\varphi, \Delta\varphi_{\gamma=0})}{K_g(\varphi)} = \frac{B}{f_{\max}} = \eta. \tag{V.30}$$

We choose to denote η the bandwidth relative to the maximum frequency. Generally η differs from both fractional and relative bandwidth as defined in (Taylor, 1994, p. 2), but we find that it provides the most compact and easily interpretable expressions in our following derivations. We recognize the relative change of ground wavenumber from (V.29), and readily obtain

$$\Delta\varphi_{\gamma=0} \approx \frac{\eta}{\tan(\varphi)}, \tag{V.31}$$

valid for $\varphi \gg \eta$. The equations yield the same result as in (Gatelli et al., 1994), but without the narrowband approximation of $\eta \approx B/f_c$. For smaller baselines

$\Delta\varphi < \Delta\varphi_{\gamma=0}$, it follows that the coherence is proportional to the fractional wavenumber overlap,

$$\hat{\gamma} \approx 1 - \frac{\Delta\varphi}{\Delta\varphi_{\gamma=0}}. \tag{V.32}$$

The overlapping part of the spectra can be isolated through bandpass filtering, either using a fixed filter over a range interval of choice (Cervenka, 2012; Gatelli et al., 1994), or using range dependent filtering (Reigber, 1999). This bandpassed part of the signals will have full wavenumber overlap, and thus no decorrelation, though at the cost of degraded resolution.

V.5.3 Stretch within Overlapping Wavenumbers

We now quantify the decorrelation as a function of uncompensated stretch. Changing the grazing angle between two observations results in decorrelation also within the overlapping ground wavenumbers. This decorrelation is caused by the different sample spacing – or stretching – between different angles of observation. The decorrelation can therefore be reduced and potentially mitigated by projecting the data onto a common frame of reference, and will be examined in V.5.4. In this section, we quantify the decorrelation from stretching within the overlapping wavenumbers (as if left uncompensated).

The analytic expression for decorrelation as a function of stretching has been derived for a Gaussian weighted spectrum in (Varghese et al., 1997). For a SAS, a bandpass signal with flat spectrum might be more representative, and we adopt a numerical estimate of the coherence expectation value as a function of the applied stretching factor $1/\chi$. We evaluate (V.2) for $\tau = 0$ with $a_2(t) = a_1(\chi t)$ for signals $a_1(t)$ of different bandwidth and center frequency. After normalizing on both the bandwidth relative to the maximum frequency η and on the theoretical resolution δt, we obtain the general result presented in Figure V.7. The normalization on $\eta\delta t$ can be reduced to $f_{\max}$, but for the applications of this study we find that the former can provide more insight.

We let coherence 0.5 indicate the point of impact for decorrelation from stretching, and from Figure V.7 we observe that this occurs for a stretching of 1.25η independent samples out from a fixed end. When stretching both ends as for our case of transmit-receive, the coherence of 0.5 thus occurs for a one-way stretching of 0.63η samples. This gives a scaling factor of $\chi_{\gamma=0.5} \approx 1 - 0.63\,\eta\,/M$, where M is the number of independent samples. We obtain the corresponding grazing angle by insertion into (V.29);

$$\Delta\varphi_{\gamma=0.5} \approx \frac{0.63}{M}\frac{\eta}{\tan(\varphi)} \approx \frac{0.63}{M}\Delta\varphi_{\gamma=0}, \tag{V.33}$$

valid for $\varphi \gg \eta/M$. We observe that the baseline for coherence 0.5 from stretching is 0.63/M times the critical baseline of ground wavenumber mismatch.

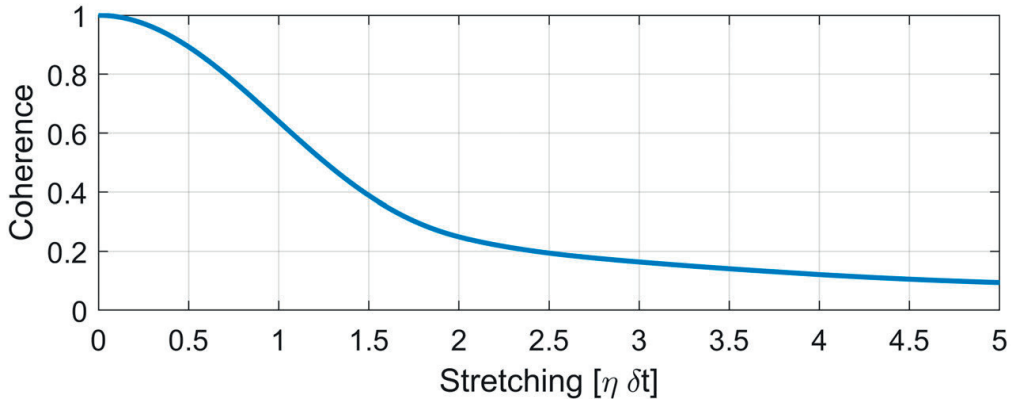

Figure V.7: Decorrelation as a function of applied stretching out from a fixed end. The plot is normalized on the bandwidth relative to the maximum frequency η and the theoretical resolution (or Nyquist sample rate) δt.

V.5.4 Improving Coherence by Compensating for Stretch

The decorrelation from stretching can be reduced and ideally mitigated over the region of overlapping wavenumbers if the stretch between observations is estimated and compensated for. There are at least three candidate approaches to such a compensation, that can be applied depending on which information is available:

V.5.4.1 Common terrain model and known baseline

This is typically the case for SAR, when accurate track navigation and digital terrain models are common. This information allows for estimating and compensating for the wavenumber shift or stretching encountered for narrow band systems and wide band systems respectively (Gatelli et al., 1994), (Cervenka, 2012).

V.5.4.2 Individual terrain models and unknown baseline

This is typically the case with interferometric SAS, that allows for generation of a terrain model based on each pass (Sæbø et al., 2007b). For this case, the slant range data can be mapped onto the ground, and thereby express the local ground wavenumber (Cervenka, 2012). In order to search for the horizontal baseline through correlation, we suggest re-sampling the ground range data onto a grid that is equispaced horizontally, and adapting the phase such that it represents a horizontal planar propagation.

V.5.4.3 No terrain model and unknown baseline

This will be the case for repeated passes of a non-interferometric SAS, but the method might also be pursued for mitigating residual stretch after de-stretching

using terrain models. For this case, a two-parameter search over baseline and stretching needs to be performed within the framework of (Cervenka, 2012). One candidate method for such a search in interferometry is (Sæbø et al., 2007a). We are also aware that decorrelation from stretching is a major challenge in elastography, and methods successfully countering small deformations in that field should be considered adapted to sonar (Ophir et al., 1999, Ch. 5.2)(Alam et al., 1997).

V.6 Summary of Predicted Decorrelation Baselines

In this section we summarize our derived expressions on the decorrelation baseline of coherence 0.5 caused by speckle decorrelation, footprint mismatch and stretching in Sections V.3, V.4 and V.5, into Table V.1. Evaluated decorrelation baselines can be used to indicate the baseline of impact for the individual contributions. Because their functional dependence on the baseline differ, the relative impact of the contributions may change for other coherence values. For sources of decorrelation with near linear dependence to baseline, the baseline of zero coherence, often denoted the critical baseline, is twice the decorrelation baseline of coherence 0.5, c.f. V.3.3.

We recall that δ is the effective element length as defined in Section V.3.4, λ is the wavelength, β is the -3dB beamwidth, r is the average range to the patch over two observations, with $r_{\min}$ the shortest, η is the ratio of bandwidth to maximum frequency, φ is the grazing angle on the ground, M is the number of independent samples, and α is the azimuth look angle.

Table V.1: Predicted Decorrelation Baselines of Coherence 0.5

Source	**Comp**	**Baseline**	**Assumption**
Speckle Decorrelation	x	$\Delta x \approx \frac{\delta}{4}$	$r_{\min} \gg \Delta x$
Speckle Decorrelation	y	$\Delta y_\infty \approx \frac{2\delta^2}{\lambda}$	$r_{\min} \gg \Delta y_\infty$
Speckle Decorrelation	y	$\Delta y \approx \Delta y_\infty \left(1 - \frac{\Delta y_\infty}{r_{\min}}\right)^{-1}$	$r_{\min} > \Delta y_\infty$
Wavenum. Mismatch	φ	$\Delta\varphi \approx \frac{1}{2}\frac{\eta}{\tan(\varphi)}$	$\varphi \gg \frac{\eta}{2}$
Wavenum. Stretching	φ	$\Delta\varphi \approx \frac{0.63}{M}\frac{\eta}{\tan(\varphi)}$	$\varphi \gg \frac{\eta}{M}$
Footprint Mismatch	y	$\Delta y \approx r_{\min}$	$\beta < 1$
Footprint Mismatch	φ	$\Delta\varphi \approx \frac{1}{3}(\pi - 2\varphi_{\min})$	$\varphi_{\min} < \cos^{-1}(\beta)$
Footprint Mismatch	α	$\lvert\Delta\alpha\rvert \approx \frac{\beta}{2\cos\varphi}$	$\varphi < \cos^{-1}(\beta)$

Effective element length δ, wavelength λ, shortest range to patch $r_{\min}$, ratio of bandwidth to maximum frequency η, grazing angle on the ground φ, number of independent samples M and -3dB beamwidth β.

V.7 Experimental Results

In order to validate and demonstrate our findings, we present results from a dedicated and controlled experiment in this section. In the experiment, we collected data from two trajectories, crossing at a small relative azimuth angle, thereby recording measurements from a continuous span of across-track baselines, and over a wide span of grazing angles.

V.7.1 Experiment

The experiment was conducted on June 5$^{\text{th}}$ 2010 using the Royal Norwegian Navy's HUGIN-MR AUV with its HISAS 1030 synthetic aperture sonar (Hagen et al., 2008). The SAS system constitutes an interferometric SAS configuration with two vertically displaced 32 element arrays on either side. Each of the receiver elements are 0.0375 m long, and the transmitter is 50% longer. The center frequency is a 100 kHz chirp signal with a programmed bandwidth of 30 kHz. HUGIN navigates using a Doppler velocity log (DVL) aided inertial navigation system (INS), and has a navigation drift in the order of 0.1% of the traveled distance for straight lines, and only around 0.01% of the traveled distance when revisiting a position (Jalving et al., 2003). From the same reference, we find a heading bias for the gyro compass of 0.04°. Because HISAS is an interferometric sensor, it can also estimate the bathymetry. The collected data should therefore be well suited to estimate and account for the angle of incidence on the seafloor by projecting the data onto ground range, following V.5.4.2.

The experiment was planned such that it collected data from repeated passes with crossings at an angle of 5°. Because the system has a -3dB beamwidth of 23°, the azimuth footprint mismatch was still rather small during the data collection. In Fig V.8 we show the SAS reflectivity and bathymetry over the target scene, together with the estimated track positions. The temporal separation between the tracks was around 10 minutes, the AUV speed was 3.9 knots, its altitude 24 meters, and the water depth 196 meters. The main features that can be observed are the trawl tracks, while the scene appears rather flat and homogeneous otherwise.

V.7.2 Cross-Correlation

We chose a patch length of 4.8 m, corresponding to around 128 independent samples with an effective signal bandwidth of 20 kHz. The rather long patch assured a low bias floor on the cross-correlation output. We selected patches from the slant range data of the first pass at distances of 50 m, 100 m and 150 m. For the second pass, we gathered ping data not only from the estimated closest point of approach, but also from 9.6 m of range samples and within ±3 standard deviations of the along-track navigation drift, returning data from 9 pings of 28 non-overlapping elements each. Then, for each element position of the first pass, we correlated the patch data with the candidate patch data from the

second pass using a sliding window cross-correlation. We illustrate the maximum coherence versus along-track element offset over 5 of the pings for the patch at 100 m range in the upper panel of Figure V.9, and the corresponding delay estimate in the lower panel. As with SAS micronavigation, we have estimated the slant range baseline from the delay corresponding to the highest coherence, and the along-track offset from the location of the coherence peak. We obtained multiple estimates (of coherence and delay) per ping of the first pass, and chose to average these in order to reduce the variance of the estimate. We also repeated the correlation process for larger effective elements, obtained by combining neighbouring elements.

V.7.3 Minimizing Decorrelation

We attempted to minimize the decorrelation from footprint mismatch and from stretching in our processing. When combining elements into larger effective elements, we steered the beam of the repeated pass to compensate for the relative change of azimuth look direction, as measured by the onboard navigation system. We also explored micro-steering around these measured angles. An upper limit on the cross-track coherence is available from the interferometric coherence between the two banks when using all 32 receiver elements. This was constantly measured to above 0.98 at 100 m range.

We reduced the decorrelation from stretching by the following application of the method of Section V.5.4.2: We chose a grid that was equispaced horizontally, and that followed the seafloor bathymetry $z(y_g)$. We recorded the bathymetry

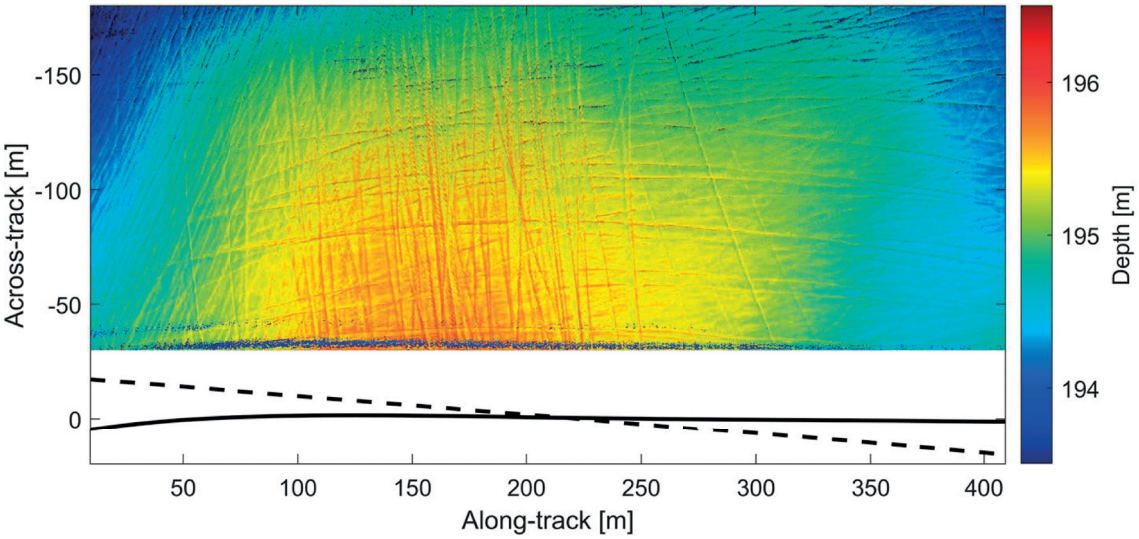

Figure V.8: SAS intensity image of the target scene, color-coded using SAS bathymetry. We observe trawl tracks on an rather flat and homogeneous seafloor. The estimated navigation of the first pass and second pass, crossing at roughly 5 degrees, are illustrated by the solid and dotted lines.

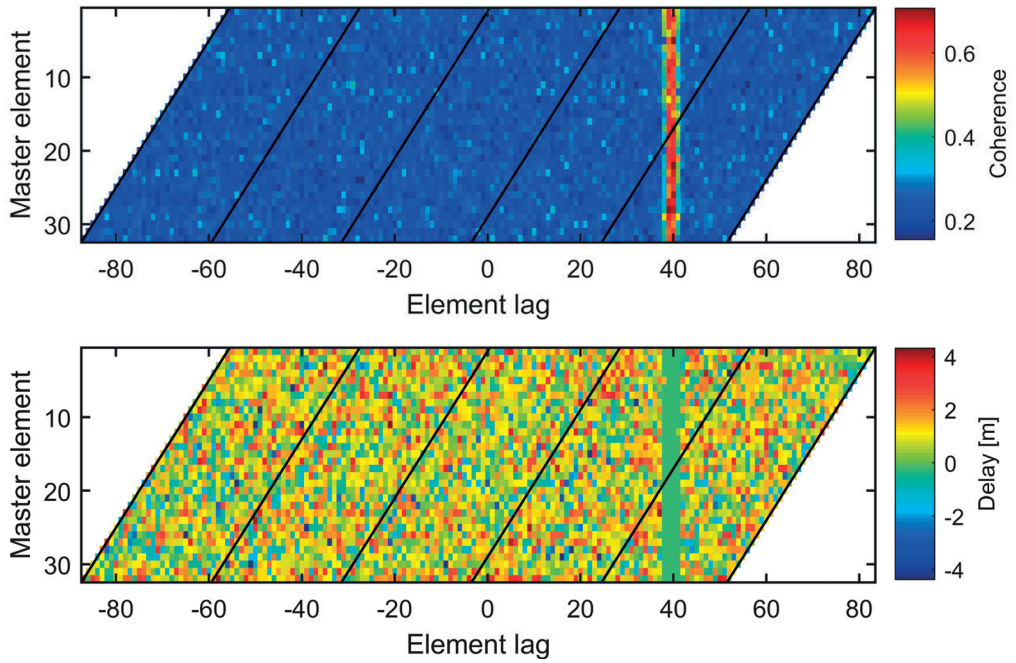

Figure V.9: Estimated coherence (upper) and delay (lower) by correlating element time series of ping 525 of the first pass with element time series for five consecutive pings of the repeated pass. Elements corresponding to the different pings of the second pass are separated by diagonal lines. The data from the first pass correspond to around 100 m slant range, and we have applied a sliding window cross-correlation of 4.8 m length, corresponding to 128 independent samples. The high coherence observed around lag 40 indicates overlapping phase centers and thus reflects the along track displacement, while the corresponding delay reflects the across-track displacement.

individually for each pass, to provide $r(y_g)$, and estimated the ground range projection $a(y_g)$ of each signal $a(r_s)$ through

$$a(y_g) = \mathcal{I}\{r_s, a(r_s) \cdot O(r_s), r(y_g)\} \cdot O^*(r(y_g)), \tag{V.34}$$

where $\mathcal{I}\{x, f, y\}$ denotes interpolation of $f(x)$ onto y. $O(r) = \exp\left\{-i2\pi f_c \frac{2r}{c}\right\}$ is a mixing term, accounting for the phase revolution at carrier f_c as a function of range.

We illustrate the resulting coherence estimates versus estimated across-track (or sway) baseline in Figure V.10.

V.7.4 Results

In Figure V.11, we present the estimated effective coherence as a function of estimated across-track baseline for all three patches. We present results both for correlating slant range data, and for correlating ground range data

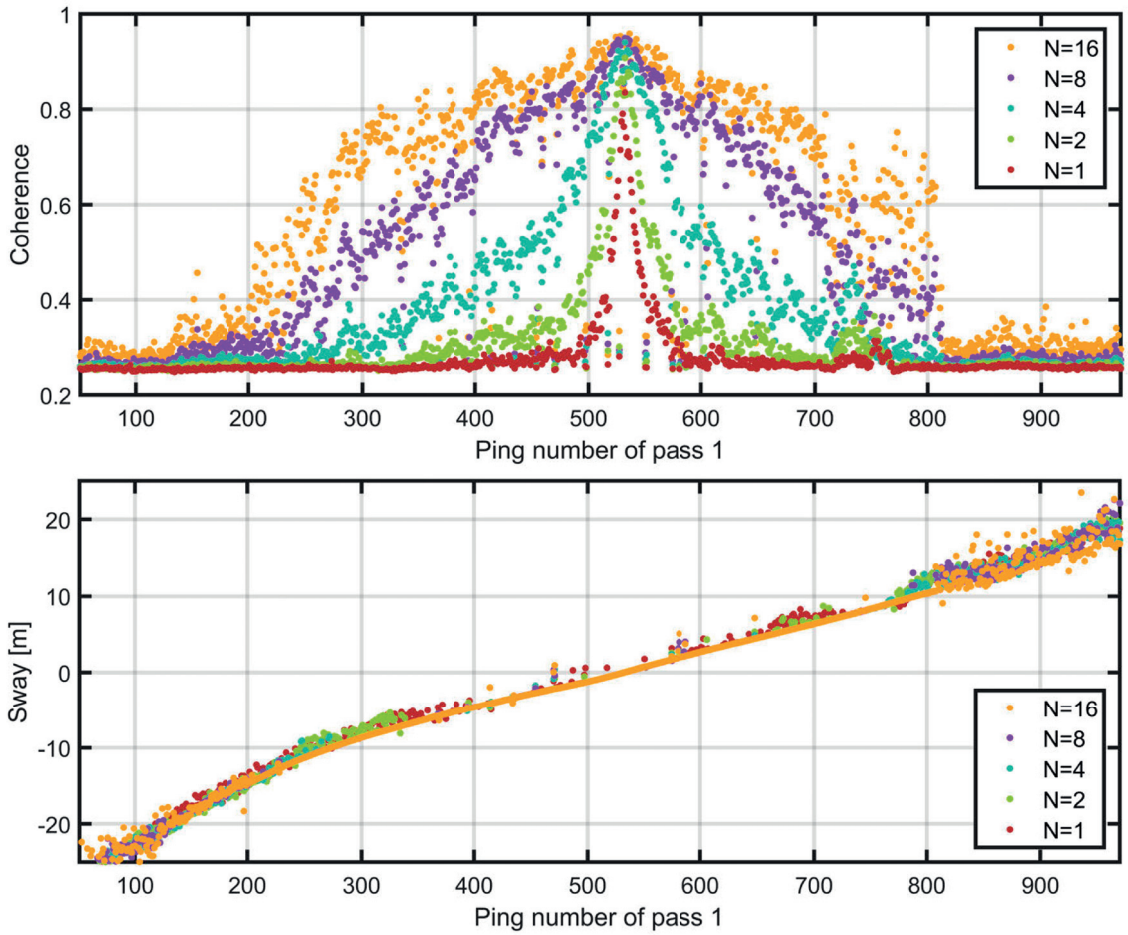

Figure V.10: Coherence and estimated sway versus ping number of the first pass for a 4.8 m patch at 150 m range with slant range to ground range conversion using the average depth.

after de-stretching by use of (V.34). Smoothed and extrapolated across-track estimates from the ground range projected data at 150 m range of combining 16 receiver elements have been adopted as ground-truth for the across-track baseline. This provided an estimate of the the across-track baseline with sub-wavelength accuracy, also where the estimated coherence was low, as with shorter receiver arrays and at shorter ranges.

We have inscribed theoretical predictions of the effect of speckle decorrelation (combined with footprint mismatch) and the effect of wavenumber stretching into Figure V.11 for comparison. These were obtained from an evaluation of the predicted decorrelation baselines for the different sources to decorrelation with the sensor parameters and the system geometry of the experiment from V.8.1.

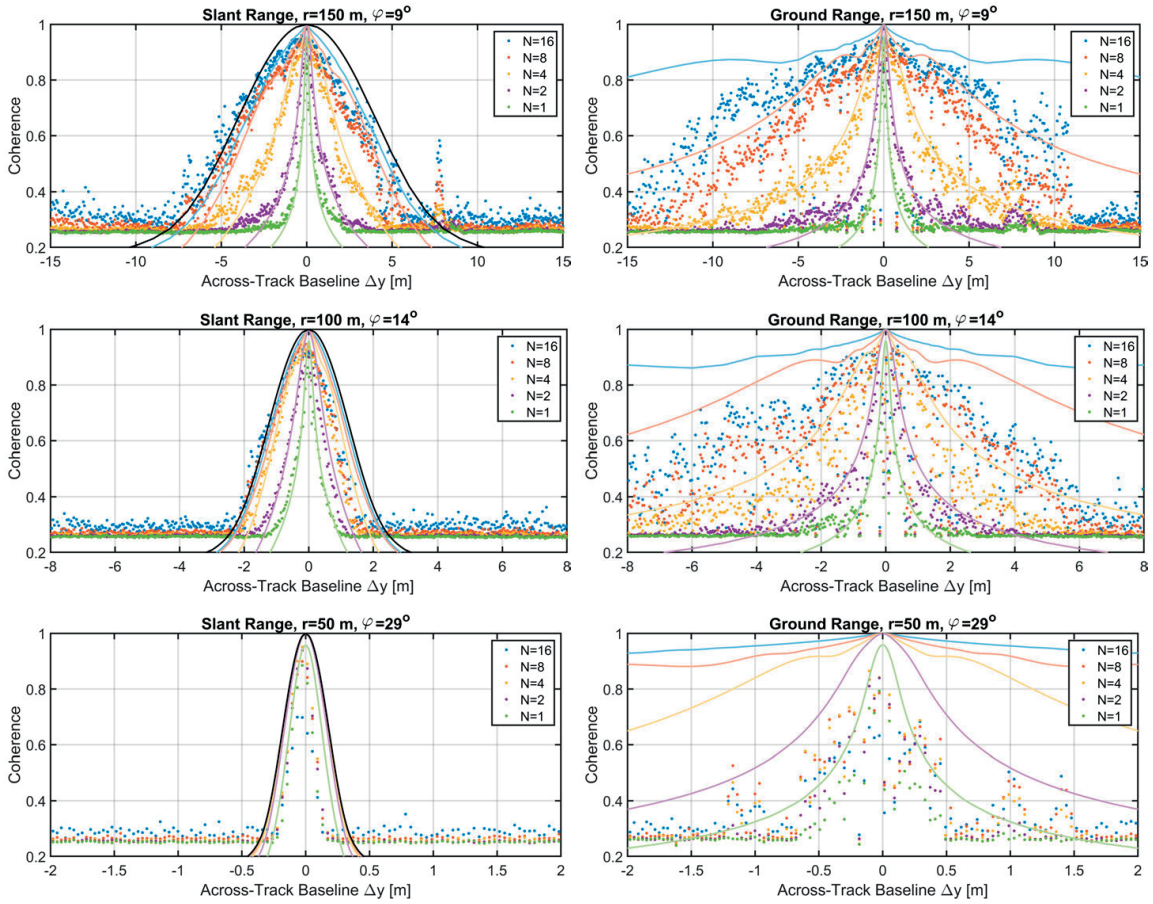

Figure V.11: Coherence between ping-pairs as a function of across-track (or sway) baseline, evaluated at slant range distances of 50 m, 100 m and 150 m. Left: Slant range data. Right: Data projected onto a common ground plane. The colors indicate the number of receiver elements combined. While each dot represents one measurement from a ping-pair, our theoretical predictions are represented as solid lines. The colored lines show the combined model effects of speckle decorrelation and decorrelation from stretching. The black lines in the left panels show the effect of stretching only. The results apply to a patch length of 4.8 m and a ratio of bandwidth to maximum frequency of 0.2.

V.8 Analysis and Discussion

We described a method for estimating the spatial coherence in Section V.2, before we derived decorrelation baselines of coherence 0.5 for each of the different sources of spatial decorrelation: footprint mismatch, speckle decorrelation and stretching in Sections V.3, V.4 and V.5. These formulas were assembled in Table V.1 of Section V.6. We then reported from a controlled experiment in Section V.7, where we had used an operational AUV with interferometric SAS for recording acoustic data over a continuous interval of across-track baselines. We estimated the spatial coherence on the data, and presented the results in Figure V.11, both with and without compensation for stretching.

In this section we analyse the predicted decorrelation from using the sensor and geometry of our experiment, identify what we consider the most important sources to decorrelation in our experiment and illustrate the predicted decorrelation from these sources in Figure V.11. Then we analyze the experimental results supported by these predictions, before we generalize our findings.

V.8.1 Predictions

We have predicted decorrelation as a function of across-track baseline for each of the potential sources of decorrelation, by use of the formulas assembled in Table V.1. We have used the parameters of the experiment from Section V.7 to obtain the effective element lengths $\delta(N = 1) \approx \sqrt{2} \cdot 0.0375\,\mathrm{m}$ and $\delta(N = 16) \approx 16 \cdot 0.0375\,\mathrm{m}$ for combining N neighbor elements into larger effective elements. The wavelength $\lambda = 0.015\,\mathrm{m}$, the effective ratio of bandwidth to maximum frequency $\eta \approx 0.18$, the number of independent samples $M \approx 128$ and the -3dB beamwidth $\beta \approx 23°$. We ran the evaluation for three patches at ranges of 50 m, 100 m and 150 m, and also included an idealized far range patch. The evaluation was executed both for correlation of single elements and for correlation of 16 receiver elements added together. We present the results in Table V.2, and list the evaluated patch ranges with the corresponding grazing angles in the two first rows, using italic text.

V.8.1.1 Correlation of Single Element Data

From Table V.2, we observe that for correlation of single elements, our prediction of speckle decorrelation indicates an across-track decorrelation baseline of 0.38 m for all evaluated patch ranges, thus constituting the most prominent source of decorrelation for small grazing angles. Decorrelation from stretching is predicted to give an increasing impact with larger grazing angles, and for grazing angles above 25 degrees the decorrelation from stretching dominates, with a predicted across-track decorrelation baseline of only 0.24 m for our closest patch at 50 m range.

Table V.2: Predicted Across-Track Decorrelation Baselines for HISAS 1030

Source	**Comp**	**Parameter**	**Decorrelation baseline @ patch**			
Patch Range		$r_{\min}$	*50 m*	*100 m*	*150 m*	∞
Patch Grazing Angle		$\varphi_{\min}$	*29°*	*14°*	*9°*	*0°*
Speckle Decorr.	y	$\Delta y(N{=}1)$	0.38 m	0.38 m	0.38 m	0.38 m
Speckle Decorr.	y	$\Delta y(N{=}16)$	1200 m	92 m	71 m	48 m
Wavenum. Mism.	φ	$\Delta y(\Delta\varphi)$	18 m	72 m	132 m	–
Wavenum. Str.	φ	$\Delta y(\Delta\varphi, M{=}128)$	0.24 m	2.1 m	7.1 m	–
Footprint Mism.	y	Δy	50 m	100 m	150 m	–
Footprint Mism.	φ	$\Delta y(\Delta\varphi)$	35 m	85 m	136 m	–
Footprint Mism.	α	$\lvert\Delta\alpha(N{=}1)\rvert$	9.2°	8.3°	8.2°	8.1°
Footprint Mism.	α	$\lvert\Delta\alpha(N{=}16)\rvert$	0.8°	0.7°	0.7°	0.7°

Predicted across-track decorrelation baselines from evaluating Table V.1 for the patch ranges and corresponding grazing angles listed in two upper rows, an operating altitude of 24 m and the processing parameters and HISAS 1030 system parameters summarized in Section V.8.1.

V.8.1.2 Correlation of Multiple Elements Added Together

From Table V.2, we observe that when processing 16 receiver elements added together, wavenumber stretching constitutes the most prominent source of decorrelation, with an across-track decorrelation baseline of 0.24 m at 50 m range, increasing to 7.1 m at 150 m range. If this stretching can be compensated for, the next prominent sources of decorrelation are wavenumber mismatch at 50 m range, limiting the decorrelation baseline to 18 m, and speckle decorrelation at far range, limiting the decorrelation baseline to 48 m.

V.8.1.3 Illustration of the Predictions

After making the above observations, we have chosen to inscribe numerical estimates on the combined effect of speckle decorrelation and footprint mismatch into Figure V.11. This contribution to decorrelation was computed for the system parameters and geometry of our experiment using the method described in V.3.2. Though computed for a range of 100 m, these results should be applicable to any $r \gg \Delta y$. We also show the predicted effect of decorrelation from wavenumber stretching from (V.33) along with the results obtained without stretch compensation of Figure V.11.

V.8.2 Analysis of Experiment

We now examine the experimental results on the spatial coherence of Figure V.11 in light of our predictions on the decorrelation baseline of coherence 0.5 for an across-track baseline from Table V.2, and our theoretical curves inscribed into Figure V.11.

V.8.2.1 Azimuth Look Direction

For our experiment, the relative heading between the tracks was around 5 degrees. We obtained a ground truth on this relative heading from the on-board INS-system, with an error that is presumed to be smaller than the absolute azimuth heading bias of 0.04° reported in V.7.1. The predicted decorrelation baseline of coherence 0.5 from footprint mismatch caused by a change of azimuth look direction was predicted to 8 degrees for correlation of single elements, and 0.7 degrees for the correlation of 16 elements added together, c.f. Table V.2. It is therefore important to apply steering to avoid decorrelation from footprint mismatch, and in particular for the case of adding elements together before correlating. In Figure V.11, we observe a measured coherence for slant range correlation at 100 m range of up to 0.85 for the single element case where no steering could be applied. For the same corresponding cases of steered multi-element receiver arrays, the measured coherence increases to 0.95, which approaches the theoretical limit for combining two independent measurements of coherence 0.98, as $0.98^2 \approx 0.96$.

V.8.2.2 Coherence Floor

The experimental results on the spatial coherence presented in Figure V.11 show a coherence floor around 0.26-0.30. We recall that we correlated 128 range samples from the first pass with 256 range samples from 9 pings and 28 non-overlapping element positions from the second pass, using a sliding window cross-correlation. This results in $L = (256-127)\cdot 9\cdot(29-N)$ coherence evaluations, when combining N neighbor elements into larger effective elements. According to Section V.2.6, and with N between 1 and 16, this should correspond to between 32508 and 15093 coherence evaluations, giving a coherence floor near 0.28. We find that the predicted and the measured levels of the coherence floor are in good agreement. Conferring Figure V.3, we note that a reduction of the patch length from 4 to 1 meter, thus reducing the number of independent samples from 128 to 32, increases the coherence floor to around 0.53. Assuming that a full correlation over all combinations are run, this coherence floor would reduce the practical baseline of valid navigation updates to roughly half that of our example.

V.8.2.3 Correlation of Slant Range Data

In the left panels of Figure V.11, we present experimental results of slant range measurements without stretch compensation. These express the combined effect of speckle decorrelation, footprint mismatch and stretching. Here we observe

an excellent agreement between our predictions and the measurements for all patches and all effective receiver element sizes.

V.8.2.4 Correlation of Ground Range Data

The decorrelation of the ground range projected (stretch compensated) measurements as a function of across-track baseline is presented in the right panels of Figure V.11. We observe that the estimated effective coherence follows the predictions for increasingly longer effective elements with longer range. Only for the patch at shortest range, we observe an invariance on element length. This can be a result of residue stretch, as this would cause a stronger decorrelation at short range where the relative stretch between the patches is the largest. Origins for residue stretch could be a combination of local terrain variations and volume scattering, both plausible with our measurements.

V.8.3 General Discussion

V.8.3.1 Effective Element Size

For small grazing angles, speckle decorrelation with range baseline constitutes the most prominent source of decorrelation when correlating single element data from repeated passes. For larger grazing angles (above 25 degrees for HISAS 1030), wavenumber stretching dominates, and must be accounted for before the fundamental limitation of speckle decorrelation can be met. While processing on single element data provides the most accurate along-track navigation, the speckle decorrelation with range baseline rapidly falls when combining multiple elements into longer effective elements and synthetic apertures, as shown in Section V.3. Increasing the feasible across-track baseline of repeat-pass SAS micronavigation to above 0.5 m can be achieved, but only by increasing the effective aperture length or by reducing the wavelength from the value used in our experiment when using a single element receiver.

V.8.3.2 Compensation for Stretching

With longer effective elements, decorrelation from relative stretching with a change of grazing angle between observations takes over as the dominating source of decorrelation. This contribution was investigated in Section V.5 and comprises both ground wavenumber mismatch and stretching within overlapping wavenumbers. While wavenumber mismatch is prominent for repeat-pass SAR interferometry, the impact of stretching increases with the number of independent range samples. In Section V.2, we saw that long range patches can be exploited for lowering the coherence floor and detecting valid measurements of repeat-pass SAS micronavigation. As a result, stretching becomes the most important source of decorrelation for repeat-pass SAS micronavigation. This decorrelation can be reduced by stretch-compensation, which is left as the critical processing step for extending the baseline of impact (towards that of speckle decorrelation). We find that stretch-compensation appears to be one important area of further

work for reducing decorrelation and extending the application of repeat-pass SAS micronavigation. Indeed, we believe that decorrelation from residue stretching remains the primary source of decorrelation of our data, also after the applied stretch-compensation. As a consequence, we have not yet included the stretch-compensation (or wavenumber alignment) with pass-band filtering of the overlapping wavenumbers.

V.8.3.3 Repeat-Pass Micronavigation

In Section V.7 we demonstrated increasing the feasible across-track baseline of repeat-pass SAS micronavigation to above 10 m, more than one order of magnitude up from what was reported before. We evaluated the spatial correlation of speckle, showing that with a fixed wavelength, 10 m baseline is only possible after combining at least 8 elements from a typical SAS system, while we combined 16 elements to meet this baseline. In Section V.1, we recognized that such an increased tolerance to across-track separation is needed to expand the feasibility of repeat-pass SAS micronavigation to cover applications with larger potential drift between passes.

V.9 Conclusion

We have investigated the spatial correlation of speckle for repeat-pass SAS micronavigation, and showed that spatial decorrelation can be effectively described through the three contributions of speckle decorrelation, footprint mismatch and stretching. We demonstrated that their combined effect is in line with the spatial decorrelation observed in actual repeat-pass SAS micronavigation measurements. We parameterized the baseline of impact for the contributions, and analyzed their absolute and relative impact. We also demonstrated increasing the across-track baseline for acquisition of repeat-pass SAS micronavigation measurements by one order of magnitude to 10 m at the cost of reducing the along-track position accuracy. This expands the feasibility of repeat-pass SAS micronavigation to cover operations with larger drift between passes.

Acknowledgments

The authors wish to thank the Royal Norwegian Navy Mine Warfare Service for the permission to use data recorded with their HUGIN 1000-MR AUV. The authors also thank Antony P. Lyons at the Center for Coastal and Ocean Mapping, University of New Hampshire, USA, for valuable discussions, and we thank our colleagues at FFI's Underwater Robotics group for important feedback upon finalizing the manuscript. And finally, we thank the anonymous reviewers for important feedback that enabled us to improve the final manuscript.

References

Alam, S. K. and Ophir, J. (1997). "Reduction of signal decorrelation from mechanical compression of tissues by temporal stretching: Applications to elastography". In: *Ultrasound in Medicine and Biology* vol. 23, no. 1, pp. 95–105.

Bellettini, A. and Pinto, M. A. (2002). "Theoretical accuracy of synthetic aperture sonar micronavigation using a displaced phase-center antenna". In: *IEEE Journal of Oceanic Engineering* vol. 27, no. 4, pp. 780–789.

Born, M. and Wolf, E. (1999). *Principles of Optics*. 7th. Cambridge, UK: Pergamon press.

Brown, D. C., Gerg, I. D., and Blanford, T. E. (2020). "Interpolation kernels for synthetic aperture sonar along-track motion estimation". In: *IEEE Journal of Oceanic Engineering* vol. 45, no. 4, pp. 1497–1505.

Callow, H. J., Hagen, P. E., Hansen, R. E., Sæbø, T. O., and Pedersen, R. B. (2012). "A new approach to high-resolution seafloor mapping". In: *Journal of Ocean Technology* vol. 7, no. 2, pp. 13–22.

Carter, G. C., Knapp, C. H., and Nuttall, A. H. (1973). "Statistics of the estimate of the magnitude-coherence function". In: *IEEE Transactoins on Audio and Electroacoustics*, no. August, pp. 388–389.

Cervenka, P. (2012). "Geometric decorrelation in acoustic tools for surveying the seafloor". In: *Proceedings of the Acoustics*. Nantes, France, pp. 2807–2813.

Denny, A. R., Sæbø, T. O., Hansen, R. E., and Pedersen, R. B. (2015). "The use of synthetic aperture sonar to survey seafloor massive sulfide deposits". In: *Journal of Ocean Technology* vol. 19, no. 1, pp. 36–53.

Dickey, F. R. and Edward, J. A. (1978). "Velocity measurement using correlation sonar". In: *IEEE Position Location and Navigation Symposium*. San Diego, CA, USA, pp. 255–264.

Doisy, Y. (1998). "General motion estimation from correlation sonar". In: *IEEE Journal of Oceanic Engineering* vol. 23, no. 2, pp. 127–140.

Ewens, W. J. and Grant, G. R. (2005). *Statistical Methods in Bioinformatics: An Introduction*. Springer Science & Business Media, p. 598.

Gatelli, F., Guarnieri, A. M., Parizzi, F., Pasquali, P., Prati, C., and Rocca, F. (1994). "The wavenumber shift in SAR interferometry". In: *IEEE Transactions on Geoscience and Remote Sensing* vol. 32, no. 4, pp. 855–865.

Goodman, J. W. (2005). *Introduction to Fourier Optics*. Roberts and Company, p. 491.

Griffiths, H. D., Rafik, T. A., Meng, Z., Cowan, C. F. N., Shafeeu, H., and Anthony, D. K. (1997). "Interferometric synthetic aperture sonar for high resolution 3-D mapping of the seabed". In: *IEE Proc. Radar, Sonar Navig.* vol. 144, no. 2, pp. 96–103.

Hagen, P. E., Fossum, T. G., and Hansen, R. E. (2008). "HISAS 1030: The next generation mine hunting sonar for AUVs". In: *Proceedings of the Underwater Defence Technology (UDT) Pacific*. Sydney, Australia, pp. 1–8.

Hansen, R. E. (2011). "Introduction to Synthetic Aperture Sonar". In: *Sonar Systems*. Ed. by Kolev, N. Z. Intech. Chap. 1, pp. 3–28. URL: http://www.intechopen.com/books/show/title/sonar-systems.

Heremans, R., Dupont, Y., and Acheroy, M. (2009). "Motion compensation in high resolution synthetic aperture sonar (SAS) images". In: *Advances in Sonar Technology*. Ed. by Silva, S. R. InTech, pp. 43–74.

Hunter, A. J., Dugelay, S., and Fox, W. L. J. (2016). "Repeat-pass synthetic aperture sonar micronavigation using redundant phase center arrays". In: *IEEE Journal of Oceanic Engineering* vol. 41, no. 4, pp. 820–830.

Hunter, A. J., Connors, W. A., and Dugelay, S. (2017). "An operational concept for correcting navigation drift during sonar surveys of the seafloor". In: *IEEE Journal of Oceanic Engineering* vol. 43, no. 4, pp. 913–926.

Hunter, A. J. and Dugelay, S. (2015). "Exploiting the coherence of seabed scattering for repeat-pass sas micro-navigation". In: *Proceedings of Seabed and Sediment Acoustics: Measurements and Modelling 2015*. Vol. 37. Bath, UK, pp. 175–182.

Jalving, B., Gade, K., Hagen, O. K., and Vestgård, K. (2003). "A toolbox of aiding techniques for the HUGIN AUV integrated inertial navigation system". In: *Proceedings of Oceans 2003 MTS/IEEE*. San Diego, CA, USA, pp. 1–8.

Li, F. K. and Goldstein, R. M. (1990). "Studies of multibaseline spaceborne interferometric synthetic aperture radars". In: *IEEE Transactions on Geoscience and Remote Sensing* vol. 28, no. 1, pp. 88–97.

Lurton, X. (2010). *An Introduction to Underwater Acoustics, Principles and Applications*. Second. Springer, p. 680.

Lyons, A. P. and Brown, D. C. (2013). "The impact of the temporal variability of seafloor roughness on synthetic aperture sonar repeat-pass interferometry". In: *IEEE Journal of Oceanic Engineering* vol. 38, no. 1, pp. 91–97.

Mallart, R. and Fink, M. (1991). "The van Cittert-Zernike theorem in pulse echo measurements". In: *The Journal of the Acoustical Society of America* vol. 90, no. 5, pp. 2718–2727.

Midtgaard, Ø. (2013). "Change detection using synthetic aperture sonar imagery with variable time intervals". In: *Proceedings of the 1st Underwater Acoustics Conference*. Corfu, Greece, pp. 713–720.

Midtgaard, Ø. and Nakjem, M. (2016). "Unmanned systems for stand-off underwater mine hunting". In: *Underwater Defence Technology Conference Proceedings*. Oslo, Norway, pp. 1–7.

Myers, V. L., Sternlicht, D. D., Lyons, A. P., and Hansen, R. E. (2014). "Automated seabed change detection using synthetic aperture sonar: Current and future directions". In: *Proceedings of Synthetic Aperture Sonar and Synthetic Aperture Radar 2014*. Vol. 36. Lerici, Italy, pp. 1–10.

Myers, V., Quidu, I., Sæbø, T., and Hansen, R. (2013). "Results and analysis of coherent change detection experiments using repeat-pass synthetic aperture sonar images". In: *Proceedings of the 1st Underwater Acoustic Conference*. Corfu, Greece, pp. 1–8.

Myers, V., Quidu, I., Zerr, B., Sæbø, T. O., and Hansen, R. E. (2020). "Synthetic aperture sonar track registration with motion compensation for coherent

change detection". In: *IEEE Journal of Oceanic Engineering* vol. 45, no. 3, pp. 1045–1062.

Neto, A. A., Rodrigues, G. P., and Alvarenga, I. D. (2017). "Seabed mapping with HISAS sonar for decommissioning projects". In: *Sea Technology*, pp. 15–18.

Oliver, C. and Quegan, S. (1998). *Understanding Synthetic Aperture Radar Images*. 1st ed. Artech house, Inc., p. 512.

Ophir, J., Alam, S. K., Garra, B., Kallel, F., Konofagou, E., Krouskop, T., and Varghese, T. (1999). "Elastography: ultrasonic estimation and imaging of the elastic properties of tissues". In: *Proceedings of the Institution of Mechanical Engineers, Part H* vol. 213, no. 3, pp. 203–233.

Reigber, A. (1999). "Range dependent spectral filtering to minimize the baseline decorrelation in airborne SAR interferometry". In: *International Geoscience and Remote Sensing Symposium (IGARSS)* vol. 3, no. 49, pp. 1721–1723.

Rindal, O. M. H. (2019). "Software beamforming in medical ultrasound imaging - a blessing and a curse". PhD thesis. University of Oslo, p. 177.

Rodriguez, E. and Martin, J. M. (1992). "Theory and design of interferometric synthetic aperture radars". In: *IEE Proceedings-F: Radar and Signal Processing* vol. 139, no. 2, pp. 147–159.

Roman, C. and Singh, H. (2007). "A self-consistent bathymetric mapping algorithm". In: *Journal of Field Robotics* vol. 24, no. 1, pp. 23–50.

Sture, Ø., Ludvigsen, M., Scheide, M. S., and Thorsnes, T. (2018). "Recognition of cold-water corals in synthetic aperture sonar imagery". In: *Proceedings of the IEEE/OES Autonomous Underwater Vehicle Workshop (AUV)*. Porto, Portugal, pp. 1–6.

Synnes, S. A. V., Callow, H. J., Sæbø, T. O., and Hansen, R. E. (2010). "Multipass coherent processing on synthetic aperture sonar data". In: *Proceedings of the 10th European Conference on Underwater Acoustics (ECUA)*. Istanbul, Turkey, pp. 1–7.

Sæbø, T. O., Hansen, R. E., Callow, H. J., and Kjellesvig, B. (2007a). "Using the cross-ambiguity function for improving sidelooking sonar height estimation". In: *Underwater Acoustic Measurements (UAM)*. Crete, Greece, pp. 309–316.

Sæbø, T. O., Hansen, R. E., and Hanssen, A. (2007b). "Relative height estimation by cross-correlating ground-range synthetic aperture sonar images". In: *IEEE Journal of Oceanic Engineering* vol. 32, no. 4, pp. 971–982.

Sæbø, T. O. and Lorentzen, O. J. (2015). *Synthetic aperture sonar images and bathymetries from the 2015 survey of the Skagerrak World War II chemical munitions dump site*. Tech. rep. FFI-rapport 2015/02345. Kjeller, Norway: Norwegian Defence Research Establishment (FFI), pp. 1–145.

Taylor, J. D. (1994). "Ultra-wideband radar overview". In: *Introduction to Ultra-Wideband Radar Systems*. Ed. by Taylor, J. D. CRC Press. Chap. 1, pp. 1–10.

Thompson, R. A., Moran, J. M., and Swenson, G. W. (2017). "Van Cittert-Zernike theorem, spatial coherence, and scattering". In: *Interferometry and Synthesis in Radio Astronomy*. Ed. by Barstow, M. A. 3rd. Springer Open, pp. 767–808. URL: https://link.springer.com/book/10.1007/978-3-319-44431-4.

Varghese, T. and Ophir, J. (1997). "Enhancement of echo-signal correlation in elastography using temporal stretching". In: *IEEE Transactions on Ultrasonics, Ferroelectrics, and Frequency Control* vol. 44, no. 1, pp. 173–180.

Wang, Z., Yang, Y., Ding, Z., Lin, S., Zhang, T., and Lv, Z. (2017). "A high-accuracy interferometric SAR images registration strategy combined with cross correlation and spectral diversity". In: *Proceedings of the International Conference on Radar Systems (Radar)*. Belfast, UK, pp. 1–6.

Zebker, H. A. and Villasenor, J. (1992). "Decorrelation in Interferometric Radar Echoes". In: *IEEE Trans. Geosci. Remote Sens.* vol. 30, no. 5, pp. 950–959.

Ødegård, Ø., Hansen, R. E., Singh, H., and Maarleveld, T. J. (2018). "Archaeological use of synthetic aperture sonar on deepwater wreck sites in Skagerrak". In: *Journal of Archaeological Science* vol. 89, pp. 1–13.

Ånonsen, K. B., Hagen, O. K., and Berglund, E. (2017). "Autonomous mapping with AUVs using relative terrain navigation". In: *Proceedings of Oceans 2017 MTS/IEEE*. Anchorage, Alaska, pp. 1–7.